

Many-body effects in the valence bands of two-dimensional heterostructures based on III/V semiconductors

Citation for published version (APA):

Kemerink, M. (1998). *Many-body effects in the valence bands of two-dimensional heterostructures based on III/V semiconductors*. [Phd Thesis 1 (Research TU/e / Graduation TU/e), Applied Physics and Science Education]. Technische Universiteit Eindhoven. <https://doi.org/10.6100/IR506715>

DOI:

[10.6100/IR506715](https://doi.org/10.6100/IR506715)

Document status and date:

Published: 01/01/1998

Document Version:

Publisher's PDF, also known as Version of Record (includes final page, issue and volume numbers)

Please check the document version of this publication:

- A submitted manuscript is the version of the article upon submission and before peer-review. There can be important differences between the submitted version and the official published version of record. People interested in the research are advised to contact the author for the final version of the publication, or visit the DOI to the publisher's website.
- The final author version and the galley proof are versions of the publication after peer review.
- The final published version features the final layout of the paper including the volume, issue and page numbers.

[Link to publication](#)

General rights

Copyright and moral rights for the publications made accessible in the public portal are retained by the authors and/or other copyright owners and it is a condition of accessing publications that users recognise and abide by the legal requirements associated with these rights.

- Users may download and print one copy of any publication from the public portal for the purpose of private study or research.
- You may not further distribute the material or use it for any profit-making activity or commercial gain
- You may freely distribute the URL identifying the publication in the public portal.

If the publication is distributed under the terms of Article 25fa of the Dutch Copyright Act, indicated by the "Taverne" license above, please follow below link for the End User Agreement:

www.tue.nl/taverne

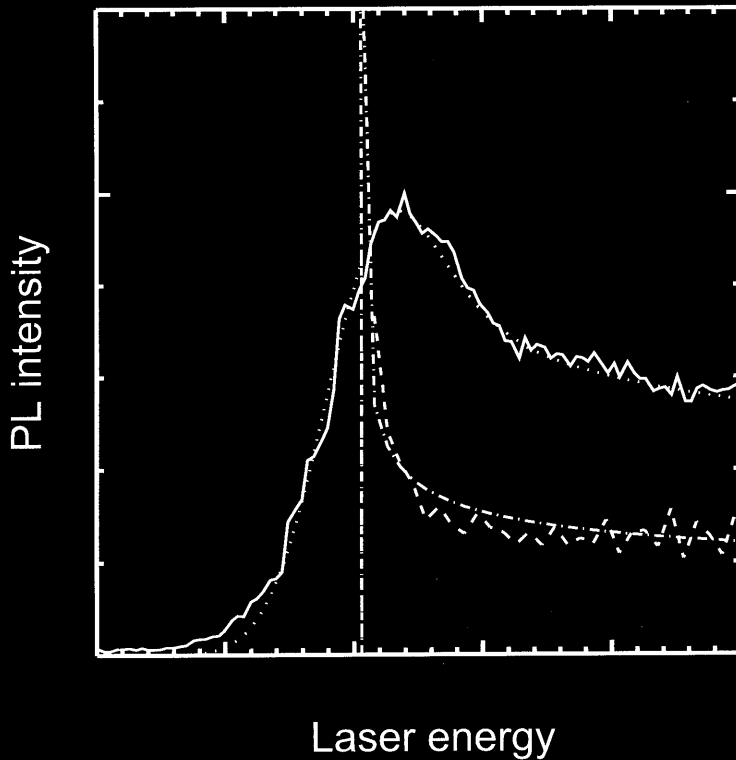
Take down policy

If you believe that this document breaches copyright please contact us at:

openaccess@tue.nl

providing details and we will investigate your claim.

Many-body effects in the valence bands of two-dimensional heterostructures based on III/V semiconductors



Martijn Kemerink

Many-body effects in the valence bands of two-dimensional heterostructures based on III/V semiconductors

PROEFSCHRIFT

ter verkrijging van de graad van doctor aan de
Technische Universiteit Eindhoven, op gezag van de
Rector Magnificus, prof.dr. M. Rem, voor een
commissie aangewezen door het College voor
Promoties in het openbaar te verdedigen
op woensdag 4 maart 1998 om 16.00 uur

door

Martijn Kemerink

geboren te Hengelo (O)

Dit proefschrift is goedgekeurd door de promotoren:

prof.dr. J.H. Wolter

en

prof.dr. L.W. Molenkamp

en de copromotor:

dr. P.M. Koenraad

CIP-DATA LIBRARY TECHNISCHE UNIVERSITEIT EINDHOVEN

Kemerink, Martijn

Many-body effects in the valence bands of two-dimensional heterostructures based on III/V semiconductors / by Martijn Kemerink. -

Eindhoven: Technische Universiteit Eindhoven. 1998.-

Proefschrift. -

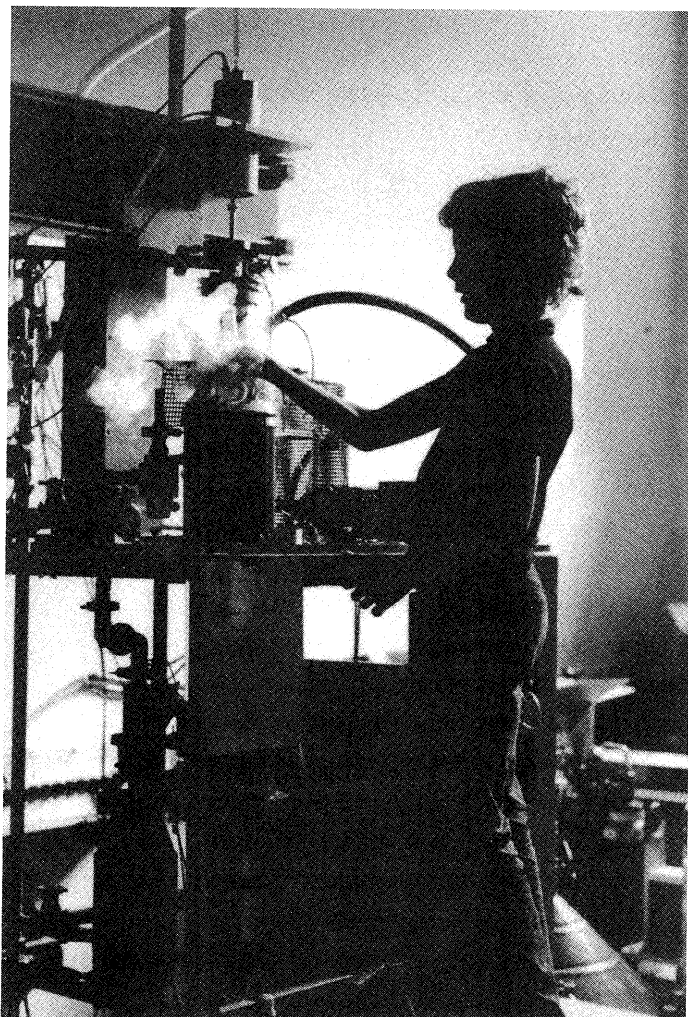
ISBN 90-386-0627-3

NUGI 812

Trefw.: veeldeeltjessystemen; halfgeleiders, optische eigenschappen; halfgeleiders, transport verschijnselen; halfgeleiders, bandenstructuur; fotoluminescentie.

Subject headings: many-particle systems; optical absorption spectra; Shubnikov-de Haas effect; semiconductor heterojunctions; bandstructure.





The author at the age of 11, filling liquid nitrogen
in the setup of his father at the
University of Groningen

Contents

1	Introduction	7
1.1	Two-dimensional semiconductor structures	8
1.2	Holes versus electrons	10
1.3	Many-body effects	11
1.4	This thesis	12
1.5	Outlook	13
	References	15
2	Hole and electron levels in 2D semiconductor structures	17
2.1	One particle states in 2D structures	18
2.1.1	The Schrödinger equation in semiconductor bulk materials ..	18
2.1.2	The envelope formalism	22
2.1.3	Electron states in 2D semiconductors	22
2.1.4	Hole states in 2D semiconductors	24
2.2	Band alignment and the effects of lattice mismatch	27
2.3	Effects of a perpendicular magnetic field	30
2.4	Many-body interactions	36
2.4.1	The Hartree term: the Poisson equation	37
2.4.2	Band gap renormalization: exchange and correlation	37
2.5	Exciton (un)binding	43
2.5.1	Free excitons in undoped heterostructures	43
2.5.2	Exciton bleaching by interactions with free carriers	45
2.5.3	Excitons in a magnetic field	47
2.6	The Broido-Sham transformation, interface conditions and numerical solutions	49
2.6.1	The Broido-Sham transformation	49
2.6.2	Interface conditions	50
2.6.3	Real-space numerical solution	50
	References	52
3	Enhancement of spin-dependent hole delocalization in degenerate asymmetric double quantum wells	55
3.1	Introduction	55
3.2	Theory	57

3.3	Numerical results	60
3.3.1	Zero in-plane wave vector	60
3.3.2	Non-zero in-plane wave vector	61
3.4	Experimental results	66
3.4.1	Transport experiments	66
3.4.2	Optical experiments	68
3.5	Summary	70
	References	72
4	The effect of strain on a second-order van Hove singularity in $\text{Al}_x\text{Ga}_{1-x}\text{As}/\text{In}_y\text{Ga}_{1-y}\text{As}$ quantum wells	75
4.1	Introduction	75
4.2	Experiments	76
4.2.1	Sample description and experimental setup	76
4.2.2	Results	78
4.2.3	Excitonic effects	79
4.3	Simulations	83
4.3.1	Numerical formalism	83
4.3.2	Numerical results and discussion	85
4.3.3	Analytical results	88
4.4	Summary	89
	References	91
5	Magneto-optical study on exciton screening in p-type $\text{Al}_x\text{Ga}_{1-x}\text{As}/\text{In}_y\text{Ga}_{1-y}\text{As}$ quantum wells	93
5.1	Introduction	93
5.2	Theory	95
5.3	Experiments	99
5.3.1	Samples and setup	99
5.3.2	Results	101
5.4	Discussion	105
5.4.1	Spectral features	105
5.4.2	Exciton screening	107
5.4.3	Comparison with other models	109
5.4.4	Numerical results	111
5.5	Conclusion	112

References	114
6 Exchange interaction in p-type GaAs/Al _x Ga _{1-x} As heterostructures studied by magneto transport	119
6.1 Introduction	119
6.2 Experiments	120
6.3 Model	123
6.4 Numerical results and discussion	128
6.5 Conclusions	132
References	134
7 Many-particle effects in Be-delta-doped GaAs/Al _x Ga _{1-x} As quantum wells	137
7.1 Introduction	137
7.2 Samples	138
7.3 Experimental results	140
7.3.1 Substrate-related PL(E)	142
7.3.2 2D-related PL(E)	144
7.4 Numerical calculations	147
7.4.1 Model	147
7.4.2 Exchange and correlation	148
7.4.3 Numerical results	150
7.5 Discussion	154
7.5.1 Exchange and correlation	154
7.5.2 Exciton screening	156
7.5.3 The absence of a Fermi-edge singularity	157
7.6 Conclusions	158
References	159
Summary	163
Samenvatting	165
List of publications	168
Dankwoord	170
Curriculum vitae	171

1 Introduction

The attitude of physicists towards semiconductor valence bands has always been somewhat ambivalent. On the one hand, to probe the complexity of the valence bands experimentally and to improve existing calculations of the valence band structure has challenged physicists throughout the years. In general, band structures are key elements in the understanding of almost all experiments on semiconductors. On the other hand, neglecting valence band complexities can strongly enlighten the interpretation of experiments in which valence bands are somehow involved. The reason is that most physical effects that are found for simple, parabolic bands, are also found in more complex bands, and vice versa. In such cases, the inclusion of valence band complexity can only obscure the physical picture. Furthermore, inclusion of realistic valence bands in actual calculations always complicates them, and often makes them impossible. It will, however, become clear that a simplified view can easily become a simple-minded view.

Also more practical arguments have forced physicists to consider the peculiarities of semiconductor valence bands. The characteristics of semiconductor optical devices like waveguides, (de-)multiplexers, light emitting diodes and lasers are always determined by the joint action of conduction and valence bands. For example, in the operation of a semiconductor quantum well laser, electrons and holes are injected in the active region, relax to their energetic minimum where population inversion has to be reached, and then recombine under the emission of light. In these subsequent steps various parameters like transport mobilities, phonon coupling, density of states, band

gaps and wave functions are important for both electrons and holes. Particularly with the advent of ternary and quaternary semiconducting materials, it has become possible to control many of these parameters independently. However, as the number of degrees of freedom is almost infinite in a modern heterostructure, a solid knowledge of the physics of these novel systems, both theoretical and experimental, is required in the device design process.

In the next paragraph semiconductor heterostructures will briefly be discussed. The following paragraphs deal with a very brief overview of earlier experiments on hole and electron systems, and with the aim and main results of the work described in this thesis. This chapter will end with a brief outlook.

1.1 Two-dimensional semiconductor structures

With modern growth facilities like Molecular Beam Epitaxy (MBE), Metal-Organic MBE (MOMBE) or Chemical Beam Epitaxy (CBE) it is possible to grow semiconducting materials atomic layer by atomic layer¹. By growing different semiconductors on top of each other¹ it is possible to create structures with an artificial potential in one dimension. These structures are generally referred to as heterostructures. When the width of the one-dimensional potential becomes of the same length scale as the electron wavelength, quantization effects occur. As the motion is restricted in the quantization direction, but still free in the other two directions, such structures are commonly referred to as (quasi) two-dimensional (2D). Chapter 2 will be dedicated to the calculation of the energy levels in these structures. For now we will restrict ourselves to introducing the four heterostructures which will be used throughout this thesis, see Fig. 1.1. Since this thesis focusses on the valence band states, hole energy is counted positive throughout this thesis, and the valence bands are plotted above the conduction bands.

The structures that will be discussed below are grown in the gallium-arsenide/aluminum-gallium-arsenide ($\text{GaAs}/\text{Al}_x\text{Ga}_{1-x}\text{As}$) material system. Since $\text{Al}_x\text{Ga}_{1-x}\text{As}$ has a larger band gap than GaAs, the former is used as barrier material. The single quantum well (QW), see Fig. 1.1(a), is in many respects the most simple heterostructure. Its active region consists of a thin well layer of GaAs, sandwiched

¹Here, we shall assume that both materials have the same lattice constants. The effects of lattice mismatch are discussed in paragraph 2.3.

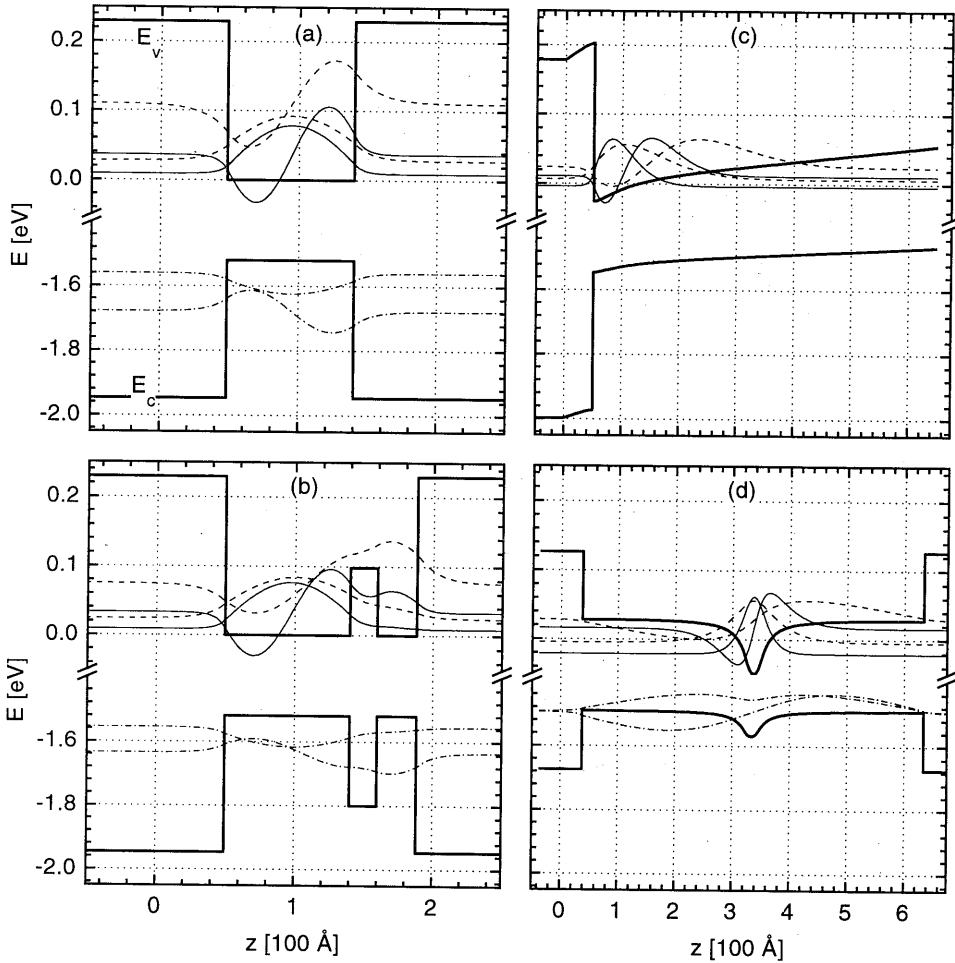


Fig. 1.1. Valence and conduction band potentials for (a) a single, empty, quantum well, (b) an empty asymmetric double quantum well, (c) a single heterojunction and (d) a center-delta doped quantum well. The thin solid, dashed and dash-dotted lines denote heavy hole, light hole and electron wave functions calculated using $\mathbf{k}\mathbf{p}$ theory, the thick solid lines denote the total confining electrostatic potential. The low and high band gap materials are GaAs and $\text{Al}_x\text{Ga}_{1-x}\text{As}$, respectively.

between two $\text{Al}_x\text{Ga}_{1-x}\text{As}$ ($x=0.45$) barrier layers. The asymmetric double quantum well (ADQW), plotted in Fig. 1.1(b), consists of two single quantum wells of different width, separated by a tunnel barrier, i.e. a layer which is thin enough to allow electrons and holes to tunnel through. The absence of inversion symmetry in this structure, i.e. the absence of a x - y plane with respect to which the potential is mirror symmetric, has remarkable effects on the properties of confined holes. The 2-D carrier confinement in

the single heterojunction (HJ) of Fig. 1.1(c) is due to the combined action of a band gap difference between the two constituent layers and the band bending arising from negatively charged acceptors and positively charged holes. As can be seen in the figure, the free carriers are spatially separated from their parent impurities. Due to this modulation doping technique, the scattering of the free carriers by the ionized impurities is strongly suppressed, as compared to the case where the spacer layer is absent. Obviously, the modulation doping technique is not restricted to single heterojunctions. Finally, it should be noted that also the HJ potential lacks inversion symmetry. The last structure to be introduced here is the center-delta-doped quantum well (δ -doped QW), see panel (d) of Fig. 1. In contrast to the common procedure in modulation doping, a sheet of beryllium (Be) dopant atoms is placed in the center of the QW. The potential resulting from the ionization of the Be atoms and the mobile holes is strongly attractive for holes, but repulsive for electrons. Consequently, the holes are confined by the resulting cusp-shaped potential, whereas the confining potential for electrons is formed by the QW. For transport experiments on these structures, the latter confinement is not necessary, but for optical experiments it is essential, in order to have sufficient overlap between holes and photo-generated electrons.

1.2 Holes versus electrons

In most 2D heterostructures, the lowest conduction band states are relatively well described by a single effective mass m^* which certainly is not the case for the highest valence band states. Moreover, electrons generally have a much higher mobility than holes. These two properties make electron systems an ideal model system for low-dimensional physics. It is therefore not surprising that, amongst others the Integer and Fractional Quantum-Hall effects^{2,3}, ballistic and phase-coherent transport^{4,5} and many-particle effects^{6,7} were all first studied in 2D electron systems, both experimentally and theoretically. Most of these effects have, at a later time, also been demonstrated in valence band systems^{8,9,10,11,12} which strengthened of course the experimental evidence for the universal character of these effects, but seldom gave rise to new insights. However, many of the effects mentioned above have been used as tools for studying valence band structure.

It is mainly for the reasons mentioned above that most research on valence bands has closely been related to the band structure, as was also mentioned in the beginning of this chapter. A large amount of 2D valence band structure calculations has appeared in

the literature both for zero¹³ and non-zero magnetic fields¹⁴. The recent interest in strained layer materials¹⁵ and growth on high-index planes, i.e. on non-(001) planes like (011), (111) and (311), has inspired theoreticians to extend their band structure calculations to these cases. Also the electron-hole interaction, giving rise to exciton formation, has been incorporated in calculations¹⁶. It is worthwhile to point out that almost all the aforementioned calculations are based on the model derived by Luttinger¹⁷, using $\mathbf{k}\cdot\mathbf{p}$ theory. Although the Luttinger model was derived to calculate impurity states in bulk semiconductors, the flexible way in which it treats the perturbing potential makes it extremely suited for calculating states in 2D systems as well. In fact, also 1D and 0D structures can be well described within the Luttinger model. In chapter 2 the Luttinger model will be discussed in some detail.

A large number of techniques has been used in experimental studies on the 2D valence band properties. In early work mainly Shubnikov-de Haas and cyclotron resonance measurements were performed for valence band characterization. Both measurements have the disadvantage that only states at the Fermi level are probed. The former method has also the disadvantage that many-particle interactions strongly affect the obtained hole masses, as will be shown in chapter 6. These effects can easily lead to an overestimation of the single particle hole mass by a factor of two. However, one of the most important properties of holes, namely the lifting of the spin degeneracy at finite wave numbers in non-inversion symmetric potentials, was first demonstrated by Eisenstein *et al.*¹⁸ in a Shubnikov-de Haas experiment. In more recent work larger parts of the valence band structure were probed, using resonant magneto-tunneling¹⁹ and hot-electron recombination²⁰. The valence band anisotropy was probed by Brosh *et al.*²¹ using the longitudinal magnetic commensurability oscillations and by Heremans *et al.*¹⁰ using transverse magnetic focussing. Finally, Molenkamp *et al.*²² used the photo-luminescence spectra of quantum wells grown on substrates of different orientations to determine the Luttinger parameters and the valence band anisotropy of GaAs.

1.3 Many-body effects

In general, calculations on semiconductor structures can significantly be simplified by ignoring interactions between the free electrons or holes, i.e. by ignoring electron-electron, hole-hole and electron-hole interactions. This procedure is known as the single-particle approximation, and often forms a good first-order approximation. Before discussing the breakdown of this single-particle model, a distinction has to be

made between few-particle interactions and many-particle interactions.

Due to the attractive Coulomb interaction between a single electron and a single hole, a hydrogen-like bound state can be formed, which is known as an exciton. This is in principle a two-particle interaction, but in a similar way complexes of one hole and two electrons, or vice versa, can be formed. These complexes are known as trions and have been observed in very high-quality heterostructures. As the formation of excitons and trions requires the presence of both electrons and holes, these few-particle effects are usually only important in optical experiments.

The many-body effects discussed in this thesis become important when a large number of carriers, in the case of this thesis holes, are present in the structure of interest. In this context, a large number means that the average inter-particle distance is comparable in magnitude to the Bohr radius of the carrier (see paragraph 2.4.2 for the definition of the Bohr radius of a single particle). For the GaAs/Al_xGa_{1-x}As heterostructures this means that these effects become important for densities above a few times 10¹⁰ cm⁻². All intentionally doped samples described in this thesis have a 2D density in the order of 10¹¹ or 10¹² cm⁻². The remark in the opening paragraph of this chapter about neglecting the complications associated with the valence band complexities in calculations is particularly true for many-body effects. Only a very limited number of papers on this subject include these complexities, and often holes are treated as electrons with a different mass. It will be shown in chapters 6 and 7 that an extension of results obtained for electron-systems to hole-systems is far from trivial.

In paragraphs 4 and 5 of chapter 2 an introductory discussion of the many-body effects that will be studied throughout this thesis will be given, together with the most important formulas.

1.4 This thesis

The common denominator of all experiments was the applied analysis method. Shubnikov-de Haas (SdH), Hall and magneto-photo luminescence (PL) and -excitation (PLE) measurements were performed, and we very carefully related the experimental findings to the valence band structure. It always turned out that the bare band structures could not describe the experimental results. Moreover, we often found that earlier interpretations, based on electron-like models, at least had to be modified or even were proven to be wrong. Examples of the latter kind are the second-order van Hove singularity, that was previously associated with an exciton line (chapter 4), and the

masses determined from temperature dependent SdH, that were proven to be dominated by exchange interactions (chapter 6), but previously were regarded as a good measure for the single-particle hole mass. The limitations of the existing theory were found in the magneto-PLE experiments described in chapter 5, which gave a very strong indication that the 2D random-phase approximation (RPA) screening theory overestimates the Coulomb screening of excited subbands. The optical experiments on δ -doped QWs (chapter 7) prove the necessity of a consistent inclusion of the valence band mixing in calculating the band gap renormalization in p-type heterostructures. As mentioned before, one should be extremely careful in regarding holes as ‘complicated electrons’, in the sense that interpretations valid for electrons can directly be applied to holes.

When we had developed a state-of-the-art band structure calculation program, it was a logical step to apply it in a numerical/theoretical study on one of the peculiar effects of the breaking of inversion symmetry on hole levels. This effect, macroscopic ‘spin’ separation, is discussed in chapter 3 and has no electronic counterpart.

The first three paragraphs of chapter 2 discuss band structure calculations in some detail. The next two paragraphs of chapter 2 deal with the theoretical description of many-particle interactions.

1.5 Outlook

All experiments discussed in this thesis are qualitatively well understood. On the other hand, the theoretical framework in which the experiments are interpreted often relies on severe approximations, especially where the many-body part of the calculations is concerned. It is, however, questionable if, in general, a further refinement of the many-body theory is worth the effort. For example, inclusion of the z -dependence, heavy-light hole coupling and magnetic field in the calculations on screened excitons (chapter 5), is not likely to yield new insight. The same is likely to hold for the effect of exchange on the hole g -factor discussed in chapter 6, and the Fermi-edge singularity that is briefly discussed in chapter 7.

In chapters 2 and 7 band gap renormalization in p-type heterostructures is discussed in some detail, and the introduced theory, in which valence band coupling is included, describes our experiments very well. At least two questions are nevertheless still open, and are worth further study. First, the derived theory employs the local density approximation (LDA), and therefore is only valid in the high-density regime. A theory beyond LDA however is still absent. In particular in systems where the mixing between

heavy and light holes is small, it is conceivable that such a theory might predict different renormalizations for heavy and light holes, in contrast to the theory discussed in this thesis. Second, our experiments on p-doped heterostructures show that occupied and unoccupied subbands renormalize almost equally, in marked contrast with several experiments²³ on highly excited intrinsic quantum wells. To my knowledge, this difference has not fully been understood, and is certainly worth further attention.

References

1. See, e.g. R. T. H. Rongen, Ph.D. thesis Eindhoven University of Technology, 1996, and references therein, A. Y. Cho, *J. Vac. Sci. Technol* **8**, s31 (1971), E. Veuhoff, W. Pletchen, P. Balk, and H. Lüth, *J. Cryst. Growth* **55**, 30 (1981), N. Vodjani, A. Lemarchand, and H. Paradan, *J. Phys. Colloq.* **43**, c5-339 (1982).
2. K. von Klitzing, G. Dorda, and M. Pepper, *Phys. Rev. Lett.* **45**, 494 (1980).
3. D. C. Tsui, H. L. Stormer, and A. C. Gossard, *Phys. Rev. Lett.* **48**, 1559 (1982).
4. For a review, see C. W. J. Beenakker and H. van Houten, *Solid State Physics* **44**, 1 (1991) or H. van Houten, C. W. J. Beenakker, and A. A. M. Staring, in *Single Charge Tunneling*, edited by H. Grabert and M. Devoret, NATO ASI, Ser. B, Vol. 294 (Plenum, New York).
5. C. J. B. Ford, T. J. Thornton, R. Newbury, M. Pepper, H. Ahmed, C. T. Foxon, J. J. Harris, and C. Roberts, *J. Phys. C* **21**, L325 (1988).
6. M. S. Skolnick, J. M. Rorison, K. J. Nash, D. J. Mowbray, P. R. Tapster, S. J. Bass, and A. D. Pitt, *Phys. Rev. Lett.* **58**, 2130 (1987).
7. A. E. Ruckenstein and S. Schmitt-Rink, *Phys. Rev. B* **35**, 7551 (1987).
8. H. L. Stormer, Z. Schlesinger, A. Chang, D. C. Tsui, A. C. Gossard, and W. Wiegmann, *Phys. Rev. Lett.* **51**, 126 (1983).
9. H. L. Stormer, A. Chang, D. C. Tsui, J. C. M. Hwang, A. C. Gossard, and W. Wiegmann, *Phys. Rev. Lett.* **50**, 1953 (1983).
10. J. J. Heremans, M. B. Santos, and M. Shayegan, *Appl. Phys. Lett.* **61**, 1652 (1992).
11. I. Zailer, J. E. F. Frost, C. J. B. Ford, M. Pepper, M. Y. Simmons, D. A. Ritchie, J. T. Nicholls, and G. A. C. Jones, *Phys. Rev. B* **49**, 5101 (1994).
12. S. Haacke, R. Zimmermann, D. Bimberg, H. Kal, D. E. Mars, and J. N. Miller, *Phys. Rev. B* **45**, 1736 (1992).
13. G. Goldoni and A. Fasolino, *Phys. Rev. B* **51**, 9903 (1995); G. Edwards, E. C. Valadares, and F. W. Sheard, *Phys. Rev. B* **50**, 8493 (1994); T. Ando, *J. Phys. Soc. Jpn.* **54**, 1528 (1985).

14. F. Ancilotto, A. Fasolino, and J. C. Maan, *Phys. Rev. B* **38**, 1788 (1988); S.-R. E. Yang, D. A. Broido, and L. J. Sham, *Phys. Rev. B* **32**, 6630 (1985); U. Ekenberg and M. Altarelli, *Phys. Rev. B* **32**, 3712 (1985).
15. See, e.g. E. P. O'Reilly, *Semicond. Sci. Technol.* **4**, 121 (1989), and references therein.
16. R. Winkler, *Phys. Rev. B* **51**, 14395 (1995) and references therein.
17. J. M. Luttinger and W. Kohn, *Phys. Rev.* **97**, 869 (1955); J. M. Luttinger, *Phys. Rev.* **102**, 1030 (1956).
18. J. P. Eisenstein, H. L. Stormer, V. Narayanamurti, A. C. Gossard, and W. Wiegmann, *Phys. Rev. Lett.* **53**, 2579 (1984).
19. R. K. Hayden, D. K. Maude, L. Eaves, E. C. Valadares, M. Henini, F. W. Sheard, O. H. Hughes, J. C. Portal, and L. Cury, *Phys. Rev. Lett.* **66**, 1749 (1991).
20. J. A. Kash, M. Zachau, M. A. Tischler, and U. Ekenberg, *Surf. Science* **305**, 251 (1994).
21. B. Brosh, M. Y. Simmons, S. N. Holmes, A. R. Hamilton, D. A. Ritchie, and M. Pepper, *Phys. Rev. B* **54**, 14273 (1996).
22. L. W. Molenkamp, R. Eppenga, G. W. 't Hooft, P. Dawson, C. T. Foxon, and K. J. Moore, *Phys. Rev. B* **38**, 4314 (1988).
23. J.A. Levenson, I. Abram, R. Raj, G. Dolique, J. L. Oudar, and F. Alexandre, *Phys. Rev. B* **38**, 13443 (1988); C. Weber, C. Klingshirn, D. S. Chemla, D.A. B. Miller, J. E. Cunningham, and C. Ell, *ibid.* **38**, 12748 (1988).

2 Hole and electron levels in 2D semiconductor structures

This chapter is intended to serve as a theoretical introduction to the following chapters. It should be stressed that we do not try to give a state-of-the-art overview of semiconductor theory, but rather present the theoretical framework in which our experimental results are interpreted. The vast majority of its content is compiled from textbooks, review and regular articles, to which we will try to refer where appropriate. The presented theory is, in general, commonly applied in semiconductor physics. Where this is not the case, particularly in paragraphs 2.4.2 and 2.5.3, we refer to chapters where a further discussion can be found.

The chapter starts with the calculation of electron and hole states in lattice matched heterostructures at zero magnetic field. Interactions with other electrons or holes are neglected (single-particle approximation). The effects of lattice mismatch, magnetic fields, many-body interactions and exciton (un)binding will be discussed in paragraphs 2.2 through 2.5, respectively. In paragraph 2.6 miscellaneous topics related to the numerical solution of the hole and electron eigenvalue equations will shortly be discussed.

Hole energy is counted *positive* throughout this thesis. Therefore, the valence band lays above the conduction band in all plots.

2.1 One particle states in 2D structures

2.1.1 The Schrödinger equation in semiconductor bulk materials

The starting point for the calculation of the valence and conduction band states is the bulk Schrödinger equation¹:

$$\left[\frac{\mathbf{p}^2}{2m_0} + V(\mathbf{r}) + \frac{\hbar}{4m_0^2 c^2} (\boldsymbol{\sigma} \times \nabla V) \cdot \mathbf{p} \right] \Psi(\mathbf{r}) = [H_0 + H_{S.O.}] \Psi(\mathbf{r}) = \epsilon \Psi(\mathbf{r}) \quad (2.1)$$

where m_0 is the free electron mass and $V(\mathbf{r})$ the electrostatic crystal potential. \mathbf{p} and $\boldsymbol{\sigma}$ are the momentum and Pauli spin operators, respectively. The first and second terms on the left-hand side are the kinetic and potential contributions, the third term describes the spin-orbit interaction. This partially relativistic expression can qualitatively be understood as follows². Consider an electron that is moving with respect to a nearby fixed charge. In the electron rest frame, however, the 'fixed' charge is moving, so there is a current present, and the electron experiences a magnetic field. If the relative motion were rectilinear, the magnetic field, as seen by the electron, would be $\mathbf{v} \times \mathbf{E}/c$. This magnetic field interacts with the spin, or more precisely, with the magnetic moment of the electron. In this case, one would expect an interaction of the form

$$\begin{aligned} H_{S.O.} &= -\mathbf{M} \cdot \mathbf{B} = 2\mu_B \mathbf{S} \cdot \mathbf{B} = \frac{e}{mc} \mathbf{S} \cdot \mathbf{B} \\ &= -\frac{e}{mc^2} \mathbf{S} \cdot \mathbf{v} \times \mathbf{E} \\ &= \frac{e}{m^2 c^2} \mathbf{S} \cdot \mathbf{p} \times \nabla \phi \\ &= -\frac{1}{m^2 c^2} \mathbf{S} \times \nabla (e\phi) \cdot \mathbf{p} \end{aligned} \quad (2.2)$$

where μ_B is the Bohr magneton and \mathbf{S} the spin operator ($\mathbf{S} = \frac{1}{2} \hbar \boldsymbol{\sigma}$). In the last step use has been made of the relations $\mathbf{A} \cdot (\mathbf{B} \times \mathbf{C}) = (\mathbf{A} \times \mathbf{B}) \cdot \mathbf{C}$ and $(\mathbf{A} \times \mathbf{B}) = -(\mathbf{B} \times \mathbf{A})$. Actually, the above is not correct. It turns out that relativistic effects associated with the fact that the electron does not move in a straight line (the Thomas precession effect) add a factor 2 to the denominator of Eq. (2.2). For a spherically symmetric potential [i.e. $\Phi(\mathbf{r}) = \Phi(r)$], Eq. (2.2) can be written as

$$H_{\text{SO}} = \frac{-1}{2m_0 c} \frac{1}{r} \frac{\partial(e\phi(r))}{\partial r} \mathbf{S} \cdot \mathbf{L} \quad (2.3)$$

with \mathbf{L} the angular momentum of the moving electron. From (2.3) it can be seen that for electrons, that originate from s-like orbitals ($L \approx 0$), the spin-orbit interaction will, in zeroth order, be small or even negligible. For electrons in GaAs and $\text{Al}_x\text{Ga}_{1-x}\text{As}$ this is a reasonable approach, for narrow-gap materials as InAs, it is not. For holes, that originate from p-like orbitals ($L \approx 1$), H_{SO} can never be neglected.

In crystalline semiconductors, the electrostatic potential $V(\mathbf{r})$ has the same periodicity as the crystal. Taking \mathbf{a}_i ($i=1,2,3$) for the basis vectors of the crystal, we then can write:

$$V\left(\mathbf{r} + \sum_x n_x \mathbf{a}_x\right) = V(\mathbf{r}) \quad (2.4)$$

which is valid for any \mathbf{r} and all integers n_i . Therefore one can look for solutions of Eq. (2.1) that are also eigenfunctions of the translation operator $T_{\mathbf{d}}$, where $\mathbf{d} = \sum_x n_x \mathbf{a}_x$:

$$T_{\mathbf{d}} \Psi(\mathbf{r}) = \Psi(\mathbf{r} + \mathbf{d}) = \exp(i\mathbf{k} \cdot \mathbf{d}) \Psi(\mathbf{r}) \quad (2.5)$$

Equivalently, the solutions of Eqs. (2.1) and (2.5) can be written in the well-known Bloch form:

$$\Psi_{\mathbf{q}\mathbf{e}\mathbf{Q}}(\mathbf{r}) = N u_{\mathbf{q}\mathbf{e}\mathbf{Q}}(\mathbf{r}) \exp(i\mathbf{k} \cdot \mathbf{d}) \quad (2.6)$$

where N is a normalization constant, $u_{n,\mathbf{k}}$ a function with the periodicity of the crystal lattice and n and \mathbf{k} are the band index and crystal wave vector, respectively.

For future purposes is useful to mention that it can easily be shown that the $u_{n,\mathbf{k}}$ can be expanded in the cell-periodic functions at the zone center \mathbf{k}_0 , $u_{n,\mathbf{k}0}$:

$$u_{\mathbf{q}\mathbf{e}\mathbf{Q}} = \sum_{\Gamma} c_{\Gamma}(\mathbf{k}) u_{\Gamma\mathbf{e}\mathbf{Q}_0} \quad (2.7)$$

Before switching to two dimensional semiconductor structures it is worthwhile to go a little deeper in the bulk solutions of (2.1). A $\mathbf{k} \cdot \mathbf{p}$ analysis of Eq. (2.1), using second order perturbation theory¹ yields dispersion relations that are quadratic in \mathbf{k} for

all band edges. This analysis is only valid in the vicinity of the Γ point. As the extension of the perturbative calculation to higher orders of k is very cumbersome, other methods have to be applied. A very successful approach was introduced by Kane³. Since the Luttinger formalism, which will be used to calculate the valence band states in 2D, uses the same basis¹ as was derived by Kane, we will briefly discuss Kane's analysis.

The essential assumption of the Kane model is that, in most semiconductors, the lowest conduction band edge and the highest valence band edge are relatively well separated from all other band edges around the Γ point. Kane therefore diagonalized the Hamiltonian $[H_0 + H_{S.O}]$ exactly within this limited set of band edges and included coupling with other Γ band edges afterwards, using second order perturbation theory. In order to diagonalize this Hamiltonian, we need a basis in which both H_0 and $H_{S.O}$ are diagonal at $k=0$. In the following we will outline the construction of such a basis.

In the absence of spin-orbit interaction, the lowest conduction band edge is twofold degenerate. Its band edge Bloch functions can be denoted as $|S\uparrow\rangle$, $|S\downarrow\rangle$, having the same properties as molecular S orbitals. The highest valence band then is sixfold degenerate, with Bloch functions $|X\uparrow\rangle$, $|Y\uparrow\rangle$, $|Z\uparrow\rangle$, $|X\downarrow\rangle$, $|Y\downarrow\rangle$, $|Z\downarrow\rangle$, having the same symmetry properties as molecular P orbitals. The S and P functions are already eigenfunctions of L^2 and S^2 , with L and S the orbital angular momentum and spin operators, respectively. However, L and S cannot characterize the valence band states uniquely, so another commuting observable needs to be introduced. We choose this to be the projection of L along the z-axis, $m_L = -1, 0, 1$. By taking linear combinations of the Bloch functions mentioned above, new Bloch functions can be constructed that are eigenfunctions of both L^2 and L_z . One finds²:

$$\begin{aligned} |1,+1\rangle &= \frac{1}{\sqrt{2}}(X+iY) \\ |1,0\rangle &= Z \\ |1,-1\rangle &= \frac{1}{\sqrt{2}}(X-iY) \end{aligned} \quad (2.8)$$

where each $|L, m_L\rangle$ state can have both spin up and down.

The spin-orbit interaction now couples the orbital and spin momenta, see Eq. (2.3). Since the total angular momentum J satisfies

¹In fact the Luttinger model reduces to the Kane model when applied to bulk.

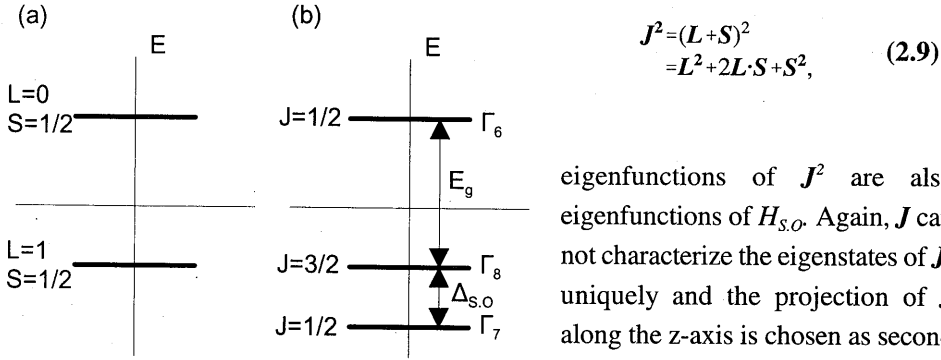


Fig. 2.1. Schematic illustration of the effect of spin-orbit coupling on the lowest conduction band edge and the highest valence band edge. (a) No spin-orbit interaction. (b) With spin-orbit interaction.

($m_j = \pm 1/2$). This is illustrated in Fig. 2.1. E_g and $\Delta_{s.o.}$ are the band-gap and spin-orbit splitting, respectively. The edges of the $J=3/2$ with $m_j = \pm 3/2, \pm 1/2$ are named the heavy and light holes, respectively, the $J=1/2$ doublet edges are the split-off band. The construction of eigenfunctions of J^2 and J_z out of those of L and S is beyond the scope of this chapter, but can be found in standard textbooks on quantum mechanics, see e.g. Ref. [2]. The final result is given in (2.10) with the states labeled as $|J, m_j\rangle$.

$$\begin{aligned}
 |\frac{1}{2}, +\frac{1}{2}\rangle &= iS\uparrow \\
 |\frac{1}{2}, +\frac{1}{2}\rangle &= \frac{1}{\sqrt{3}}[(X+iY)\downarrow + Z\uparrow] \\
 |\frac{3}{2}, +\frac{3}{2}\rangle &= \frac{1}{\sqrt{2}}[(X+iY)\uparrow] \\
 |\frac{3}{2}, +\frac{1}{2}\rangle &= \frac{1}{\sqrt{6}}[(X+iY)\downarrow - 2Z\uparrow] \\
 |\frac{3}{2}, -\frac{1}{2}\rangle &= \frac{1}{\sqrt{6}}[-(X-iY)\downarrow - 2Z\uparrow] \\
 |\frac{3}{2}, -\frac{3}{2}\rangle &= \frac{1}{\sqrt{2}}[(X-iY)\downarrow] \\
 |\frac{1}{2}, -\frac{1}{2}\rangle &= \frac{1}{\sqrt{3}}[-(X-iY)\downarrow + Z\uparrow] \\
 |\frac{1}{2}, -\frac{1}{2}\rangle &= iS\downarrow
 \end{aligned} \quad (2.10)$$

To recapitulate, Eq. (2.10) is the basis on which the total Hamiltonian [$H_0 + H_{s.o.}$] is diagonal at $\mathbf{k}=0$. At non-zero wave vectors off-diagonal elements arise due to $\mathbf{k}\cdot\mathbf{p}$ terms, resulting from the kinetic term in Eq. (2.1), and interactions with higher bands. We will come back to these terms in the discussion of the Luttinger Hamiltonian.

2.1.2 The envelope formalism

To solve Eq. (2.1) in two-dimensional semiconductor structures, further approximations have to be made. As most experimental properties of semiconductor heterostructures are determined by states near one of the high symmetry points, i.e. the Γ , X or L point, of the host materials, the envelope formalism is extremely suited for a theoretical interpretation of experiments. The main advantages of this model are its relative mathematical simplicity and the physical transparency of the obtained results.

Two key assumptions are made in the envelope formalism. Firstly, inside each material layer, the wave function is expanded on the periodic parts of the Bloch functions of the edges m under consideration. Secondly, the periodic parts of the Bloch functions are assumed to be equal in each heterostructure layer. Under these assumptions the wave function can be written as

$$\Psi(\mathbf{r}) = \sum_m \phi_m(\mathbf{r}) u_{m, \mathbf{k}_0}(\mathbf{r}) \quad (2.11)$$

The possible \mathbf{k} dependence of $\Psi(\mathbf{r})$ and the envelope functions $\phi_m(\mathbf{r})$ has been dropped for simplicity. Eq. (2.11) is obtained from Eq. (2.7) when the constants c_m are made position dependent. As we will only consider lattice matched and elastically strained structures, the in-plane lattice constant is the same in each layer. The total heterostructure will therefore be translationally invariant in the layer plane, and the in-plane motion of the particles can be described by plane waves:

$$\Psi(\mathbf{r}) = \sum_m \frac{1}{\sqrt{S}} \exp(i\mathbf{k}_\parallel \cdot \mathbf{r}_\parallel) \zeta_m(z) u_{m, \mathbf{k}_0}(\mathbf{r}) \quad (2.12)$$

where S denotes the sample area, \mathbf{k}_\parallel the in-plane wave vector and $\zeta_m(z)$ the envelope function of edge m in the z direction. The interfacial plane is taken perpendicular to the z axis.

2.1.3 Electron states in 2D semiconductors

In GaAs and $\text{In}_x\text{Ga}_{1-x}\text{As}$ with $x \leq 0.25$ the lowest conduction band is relatively well separated from all other bands. Therefore the admixture of other band-edge states to the conduction band wave function is very small in the vicinity of the Γ point. For the

conduction band states, the basis Eq. (2.10) can then be reduced to $iS\uparrow$ and $iS\downarrow$ and the summation in Eq. (2.12) only runs over these states. Under these conditions it can be shown¹ that the slowly varying envelope functions $\zeta_m(z)$ are given by the equation

$$\left[-\frac{\hbar^2}{2m^*(z)} \frac{\partial^2}{\partial z^2} + \frac{\hbar^2 \mathbf{k}_\parallel^2}{2m^*(z)} + U_c(z) \right] F_i(z) = E_i(\mathbf{k}_\parallel) F_i(z) \quad (2.13)$$

where m^* is the layer dependent electron effective mass, $U_c(z)$ the bottom of the conduction band and E_i and F_i the energy and envelope wave function of the i -th subband. For eigenfunctions of Eq. (2.13) the subband index i is a good quantum number that equals the number of nodes in the envelope function $F_i(z)$. In the following, we will use the term eigenstate to refer to the combination of the eigenvalue E_i and eigenfunction F_i , and E_0, E_1 etc. will be used to abbreviate the electronic groundstate and first excited state in a 2D heterostructure. Similarly, we will use H_i and L_i to denote the i -th eigenstate of the heavy and light holes, respectively. As Eq. (2.13) is independent of spin, each level is twice degenerate (Kramers degeneracy).

Eq. (2.13) is a good approximation for the lowest conduction band states in not too narrow quantum wells ($l_z \geq 100 \text{ \AA}$). For higher subbands the error in Eq. (2.13) caused by admixture of other Γ edges becomes significant. From fourth-order $\mathbf{k}\cdot\mathbf{p}$ theory it was derived⁴ that the admixture of highest valence band edges ($J=3/2$ and $1/2$) leads to a correction on $E(\mathbf{k}_\parallel)$ of the form

$$E'(\mathbf{k}_\parallel, \hat{k}_z) = \epsilon(\mathbf{k}_\parallel, \hat{k}_z) \left[1 + \frac{K_2}{E_g} \epsilon(\mathbf{k}_\parallel, \hat{k}_z) \right] \quad (2.14)$$

with

$$K_2 = \left[1 - \frac{m^*}{m_0} \right]^2 E_g \left[\frac{3E_g + 4\Delta_{s.o} + 2\Delta_{s.o}/E_g}{(E_g + \Delta_{s.o})(3E_g + 2\Delta_{s.o})} \right] \quad (2.15)$$

$$\epsilon(\mathbf{k}_\parallel, \hat{k}_z) = \frac{\hbar^2(\mathbf{k}_\parallel^2 + \langle \hat{k}_z^2 \rangle)}{2m^*}$$

where E_g and $\Delta_{s.o}$ are the band gap and spin-orbit splitting of the material, respectively. It is easy to show that, at $\mathbf{k}_\parallel=0$, for square wells with infinite barriers ϵ equals the confinement energy, i.e. the distance between the bottom of the well and $E(0)$. For parabolic wells ϵ equals half the confinement energy, again at $\mathbf{k}_\parallel=0$.

2.1.4 Hole states in 2D semiconductors

In bulk and in most 2D heterostructures, the energetic separation between the highest valence band edges ($J=3/2$, $m_f=\pm 3/2$, $\pm 1/2$) is very small. Consequently, they interact very strongly at non-zero \mathbf{k} and an equation like Eq. (2.13) is not applicable for a proper description of their in-plane dispersions, even when interactions with the lowest conduction band and the split-off band are weak and can be neglected. The simplest realistic model for the valence band edges therefore requires at least the $J=3/2$ quadruplet as basis. In GaAs and low indium-content $\text{In}_y\text{Ga}_{1-y}\text{As}$ the conduction and split-off bands are indeed well separated from the $J=3/2$ quadruplet ($E_{\text{gap}}=1.52$ eV and $\Delta_{s,0}=0.34$ eV at 4.2 K for GaAs) and can be ignored in most cases^{1,5,6}. The highest valence band states are then described by the Luttinger Hamiltonian \underline{H}_{Lut} ⁷. When we choose $\{|3/2, +3/2\rangle, |3/2, -1/2\rangle, |3/2, +1/2\rangle, |3/2, -3/2\rangle\}$ as our basis, the Luttinger Hamiltonian becomes:

$$\underline{H}_{Lut}(k_x, k_y, k_z) = \frac{\hbar^2}{2m_0} \begin{bmatrix} H_h & c & -b & 0 \\ c^\dagger & H_l & 0 & b \\ -b^\dagger & 0 & H_l & c \\ 0 & b^\dagger & c^\dagger & H_h \end{bmatrix} \quad (2.16)$$

The elements H_h , b and c are, with the quantization direction along the z-axis, given by

$$\begin{aligned} H_h &= (k_x^2 + k_y^2)(\gamma_1 + \gamma_2) + k_z^2(\gamma_1 - 2\gamma_2), \\ H_l &= (k_x^2 + k_y^2)(\gamma_1 - \gamma_2) + k_z^2(\gamma_1 + 2\gamma_2), \\ b &= 2\sqrt{3}\gamma_3(k_x - ik_y)k_z, \\ c &= -\sqrt{3}[\gamma_2(k_x^2 - k_y^2) - 2i\gamma_3k_xk_y], \\ &= -\sqrt{3}\left(\frac{\gamma_2 + \gamma_3}{2}\right)(k_x - ik_y)^2 + \sqrt{3}\left(\frac{\gamma_3 - \gamma_2}{2}\right)(k_x + ik_y)^2 \end{aligned} \quad (2.17)$$

The † denotes the Hermitian conjugation. The material parameters γ_1 , γ_2 and γ_3 are the Luttinger parameters. Together with Eqs. (2.16) and (2.17) they describe both the coupling between the edges within the $J=3/2$ quadruplet and the coupling of the $J=3/2$ quadruplet edges with all other Γ -edges, including the conduction band, but excluding the split-off band. For most III/V binary compounds they are relatively well known⁸, although even for such intensively studied materials like GaAs, there is some debate on which set of γ_i s is the most suited⁹.

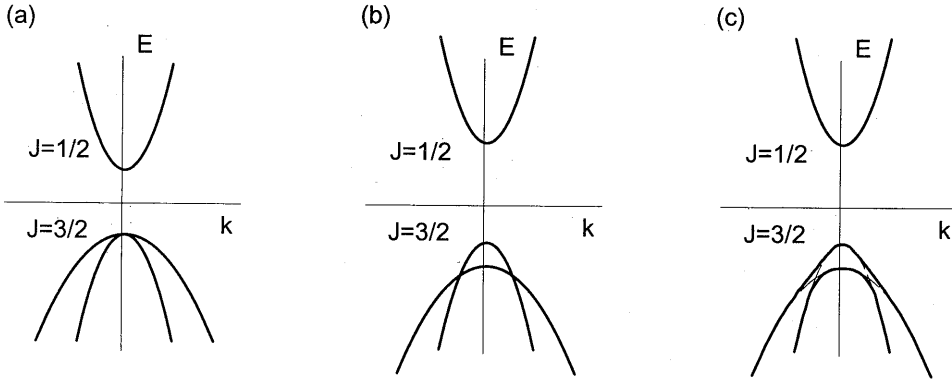


Fig. 2.2. Illustration of the effect of the 2D confinement and the off-diagonal elements in the Luttinger Hamiltonian. (a) Bulk semiconductor. (b) 2D confinement in diagonal approximation. (c) 2D confinement with full 4*4 Luttinger Hamiltonian.

Since Eq. (2.16) takes only the periodic (bulk) part of the electrostatic potential $V(\mathbf{r})$ in Eq. (2.1) into account, the confining potential still has to be added to obtain the total hole eigenvalue equation. In the envelope formalism it is usually tacitly assumed that the interface potential does not mix the various band edges, but only shifts them, which is plausible due to the very different symmetries of the conduction and valence bands¹⁰. Under this condition the electrostatic potential term only adds to the diagonal of Eq. (2.16). When we choose to align the confining potential with the z -axis, this becomes our quantization axis and the total hole eigenvalue equation reads

$$\left[\underline{H}_{Lut}(k_x, k_y, \frac{1}{i} \frac{\partial}{\partial z}) + \underline{U}(z) \right] G_i(k_x, k_y, z) = E_i G_i(k_x, k_y, z) \quad (2.18)$$

with $\underline{U}(z)$ a 4*4 matrix with on its diagonal the elements $U_{v,h}(z)$, $U_{v,l}(z)$, $U_{v,l}(z)$ and $U_{v,h}(z)$, respectively, and zeros on all other positions. $U_{v,h}(z)$ and $U_{v,l}(z)$ are the electrostatic potentials, without the cell periodic part, for heavy and light holes, respectively. In the absence of strain effects these are the same. The E_i and G_i are the eigenvalue and envelope function spinor of the i -th subband, respectively. Note that k_z had to be replaced by its operator form.

Of course it is possible to choose another quantization axis than the z axis. Our choice has the advantage that heavy ($m_J = \pm 3/2$) and light ($m_J = \pm 1/2$) hole states decouple at $\mathbf{k} = 0$. Other choices can be advantageous from a numerical point of view¹¹.

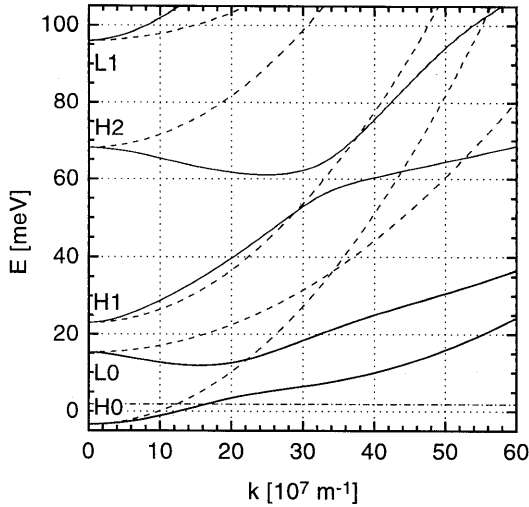


Fig. 2.3. Calculated dispersions of the lowest hole subbands in a 90 Å GaAs/Al_{0.45}Ga_{0.55}As QW with $p=5 \cdot 10^{15} \text{ m}^{-2}$. The solid lines result from the full calculation, dashed lines from the diagonal approximation. The dash-dotted line indicates the Fermi level.

elements are still neglected (diagonal approximation), comparison with Eq. (2.13) gives heavy and light hole in-plane or longitudinal masses of $1/(\gamma_1 + \gamma_2)$ and $1/(\gamma_1 - \gamma_2)$, respectively. Now the heavy and light holes have reversed their character in the sense that the heavy holes have an in-plane mass that is smaller than the light hole in-plane mass. Due to this mass reversal effect, the heavy and light hole energies would cross at a certain value of k_{\parallel} , see Fig. 2.2(b). However, due to interactions between the heavy and light holes, which are accounted for by the off-diagonal elements in the Luttinger Hamiltonian, the crossing is avoided and anti-crossing gaps open. This is illustrated in Fig. 2.2(c).

This anti-crossing can also be understood in terms of the Pauli principle, by considering the quantum numbers that still exist at finite k_{\parallel} . Due to the off-diagonal elements in the Luttinger Hamiltonian, states of different m_j are mixed at non-zero k_{\parallel} , so m_j ceases to be a good quantum number. Also the subband index i is no longer a good quantum number at finite k_{\parallel} . This is due to the d/dz operator in element b of the Hamiltonian Eq. (2.16), which couples states with subband index i to states with index $i \pm 1$. Therefore, the only remaining quantum numbers are J , k_x and k_y . At a crossing they would be the same for both heavy and light holes, which is forbidden by the Pauli

The last part of this paragraph is spent with the interpretation of the Luttinger Hamiltonian and the hole eigenvalue Eq. (2.18). At $k_{\parallel} = 0$ all non-diagonal elements in Eq. (2.16) vanish and four uncoupled one-dimensional Schrödinger equations remain. By comparison with Eq. (2.13) one finds that the heavy and light holes have a band- or transverse-effective mass of $1/(\gamma_1 - 2\gamma_2)$ and $1/(\gamma_1 + 2\gamma_2)$, respectively. Usually, all γ_i are positive and $\gamma_1 > 2\gamma_2$ so the heavy holes indeed have a higher binding mass than the light holes. This is illustrated in Fig. 2.2(a) and (b).

When $k_{\parallel} \neq 0$, but all off-diagonal

principle. Therefore the levels must anti-cross.

Fig. 2.3 displays the dispersion relations of a p-type GaAs/Al_{0.45}Ga_{0.55}As quantum well of 90 Å width and density $p=5 \cdot 10^{15} \text{ m}^{-2}$. Both the results of the diagonal approximation and the full Luttinger Hamiltonian are shown. The electron-like mass of L0 at small k is due to the repulsive interaction between L0 and H1. This interaction is expressed by the element b in the Luttinger Hamiltonian, as stated above.

2.2 Band alignment and the effects of lattice mismatch

The alignment of the band edges of two different semiconductors are grown on top of each other has been the subject of intense debate. In our calculations we have mainly employed band edge discontinuities, or band offsets, that follow from the model-solid theory of van de Walle¹². This theory predicts band alignments of both valence and conduction bands for many heterojunctions in III/V, II/VI and group IV semiconductors. Furthermore, the effects of strain can be incorporated as simply as in bulk semiconductors, which subject will be discussed below. Most importantly, the agreement with experiments seems to be rather good. The principal feature of the model-solid theory¹² is that it gives the average valence band energy $E_{v,av}$, defined as $E_{v,av} \equiv (E_{hh} + E_{lh} + E_{s,o})/3$, for each bulk semiconductor on an absolute energy scale. Band edge discontinuities at any hetero interface can then be calculated by simply subtracting the respective $E_{v,av}$'s. The conduction band edge of a semiconductor is obtained by adding the experimental value of the band-gap to the (unstrained) heavy hole, or equivalently light hole, edge: $E_c = E_{v,av} + (1/3)\Delta_{s,o} + E_g$.

From the calculation procedure following from the model-solid theory, band edge discontinuities appear to be uniquely determined by bulk properties and should therefore have the transitivity property. However, the band alignment is directly related to the electrostatic potential lineup^{13,14}, defined as the the difference between the average electrostatic potential on the two sides of the interface, which arises from the electron density distribution at the interface. In general, this electron density distribution depends on the interfacial atomic configuration^{14,15} and composition¹⁶, and on the orientation of the substrate¹⁷, and therefore the band alignment also depends on these factors. However, for lattice matched interfaces, it has theoretically been shown that, within the numerical accuracy, both the transitivity rule is satisfied¹⁸ and the dependences on interface orientation, atomic configuration and composition are absent^{13,14,18}. Our reason to employ the model solid theory also for the strained In_yGa_{1-y}As/Al_xGa_{1-x}As system is its proven

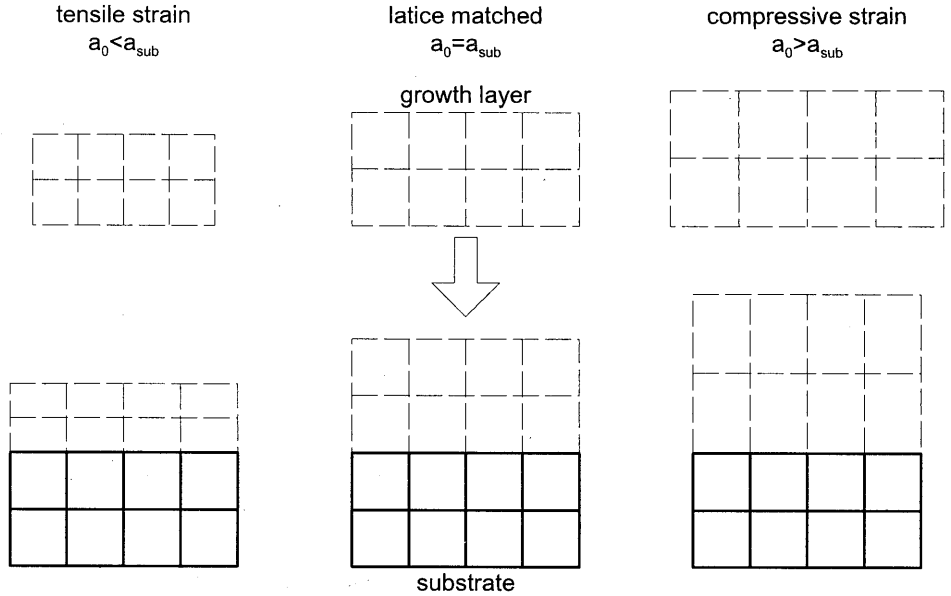


Fig. 2.4. Schematic illustration of pseudomorphic (left and right panels) and lattice matched (central panel) growth. The squares denote the crystal unit cells.

good agreement with experiments in similar material systems and its mathematical simplicity¹².

The envelope formalism that was discussed in the previous paragraph can easily be extended to take the effects of lattice mismatch into account. Consider a semiconducting layer, with equilibrium lattice constant a_0 , that is grown on a (001) substrate with lattice constant a_{sub} , see Fig. 2.4. As long as the thickness of the top layer does not exceed a certain critical value, the top layer will accommodate its lattice constant such that its in-plane lattice constant equals a_{sub} . When the critical layer thickness^{19,20} is exceeded, defects in the crystal lattice arise. Below this critical layer thickness, the growth is called pseudomorphic or commensurate and the resulting biaxial strain in the plane of the interface is then given by:

$$\epsilon_{||} = \epsilon_{xx} = \epsilon_{yy} = \frac{a_{sub} - a_0}{a_0} \quad (2.19)$$

From elasticity theory one knows that the relation between an elastic deformation $d\mathbf{r}/r$ and the applied pressure \mathbf{P} is $\mathbf{P}=\underline{C}\cdot d\mathbf{r}/r$ with \underline{C} the elasticity tensor. For crystals with cubic symmetry, like most semiconductors, all diagonal elements are equal, with value C_{11} , and all off-diagonal elements are equal, with value C_{12} . In equilibrium all forces balance and $\mathbf{P}=0$. Applying this condition to the toplayer-vacuum interface we find for the uniaxial strain perpendicular to the interfacial plane

$$\epsilon_{\perp} = \epsilon_{zz} = -2 \frac{C_{12}}{C_{11}} \epsilon_{\parallel} \quad (2.20)$$

All non-diagonal strain tensor elements are zero for (001) growth. A more extensive treatment of strain effects for growth along non-(001) directions in relation to the Luttinger formalism is beyond the scope of this chapter²¹.

The hydrostatical component of the strain, $(\epsilon_{xx} + \epsilon_{yy} + \epsilon_{zz})$, causes a shift of the average valence band edge energy $E_{v,av}$ ^{22,12}

$$\Delta E_{v,av} = a_v (\epsilon_{xx} + \epsilon_{yy} + \epsilon_{zz}) = 2a_v \left(1 - \frac{C_{12}}{C_{11}} \right) \epsilon_{\parallel} \quad (2.21)$$

Similarly, for the conduction band energy one has

$$\Delta E_c = a_c (\epsilon_{xx} + \epsilon_{yy} + \epsilon_{zz}) = 2a_c \left(1 - \frac{C_{12}}{C_{11}} \right) \epsilon_{\parallel} \quad (2.22)$$

Here, a_v and a_c are the hydrostatic deformation potentials of the valence and conduction band, respectively.

The shear component of the strain, $(2\epsilon_{zz} - \epsilon_{xx} - \epsilon_{yy})$, couples to the spin-orbit interaction. This leads to an additional splitting of the valence band energies. With respect to $E_{v,av}$ and for (001) growth, the following shifts are calculated^{23,12}:

$$\begin{aligned} \Delta E_{v,h} &= \frac{1}{3} \Delta_{s,o} - \frac{1}{2} \delta E^{sh} \\ \Delta E_{v,l} &= -\frac{1}{6} \Delta_{s,o} + \frac{1}{4} \delta E^{sh} + \frac{1}{2} \left[\Delta_{s,o}^2 + \Delta_{s,o} \delta E^{sh} + \frac{9}{4} (\delta E^{sh})^2 \right]^{\frac{1}{2}} \\ \Delta E_{v,s,o} &= -\frac{1}{6} \Delta_{s,o} + \frac{1}{4} \delta E^{sh} - \frac{1}{2} \left[\Delta_{s,o}^2 + \Delta_{s,o} \delta E^{sh} + \frac{9}{4} (\delta E^{sh})^2 \right]^{\frac{1}{2}} \end{aligned} \quad (2.23)$$

In these equations δE^{sh} is given by

$$\delta E^{sh} = b(2\epsilon_{zz} - \epsilon_{xx} - \epsilon_{yy}) = -2b \left[\frac{2C_{12}}{C_{11}} + 1 \right] \epsilon_{\parallel} \quad (2.24)$$

with b the shear deformation potential.

So far, strain effects on bulk band edges have been discussed. In the hole and electron eigenvalue equations, the strain shifted band edges are accounted for by adding the various ΔE 's to the respective electrostatic potentials $U_{c,v}$. Figs. 2.5(a-c) illustrate the effects of the hydrostatic and shear components of the strain, for both compressive ($a_0 > a_{sub}$) and tensile ($a_0 < a_{sub}$) strain. The example deals with the lowest conduction, heavy and light hole bands in an $\text{In}_y\text{Ga}_{1-y}\text{As}$ quantum well embedded between InP barrier layers, grown on an InP substrate. For clarity, only the diagonal elements in the hole eigenvalue equation (2.18) are considered. Furthermore, alloy effects on the Luttinger parameters, electron effective mass and spin-orbit splitting have been neglected. From the figure it is evident that the strain modifies the relative heavy and light hole positions and hence their interaction when the non-diagonal elements in the Luttinger Hamiltonian are taken into account. By choosing the appropriate In fraction y , the heavy-light hole interaction can be lessened ($y < 0.53$), generally resulting in an enhancement of their parabolicity, or enhanced ($y > 0.53$). The latter case can, in extreme situations lead to a reversal of the heavy-light hole order, i.e. $E(L0) < E(H0)$. It will be clear that the application of strain in semiconductor heterostructures opens huge possibilities for what is called 'band engineering'. In particular the use of quaternary materials as InAlGaAs or InGaAsP , that allow for an independent adjustment of the band gap and the lattice constant, is useful for device applications. For a more extensive discussion of this subject the reader is referred to other publications^{24,25,26} and references therein.

2.3 Effects of a perpendicular magnetic field

The application of an arbitrarily directed magnetic field \mathbf{B} to a two-dimensional electron or hole gas, leads, via the Lorentz force, generally to a coupling of the motions in the x , y and z directions. Consequently, a separation like Eq. (2.12) is no longer possible and, even when parabolic bands are assumed, no general solution to the Schrödinger equation is found. However, in the limits of extremely low or high magnetic field of arbitrary direction, the field or the confinement can be treated as a perturbation, and the Schrödinger equation can be solved. For arbitrary fields, exact solutions of the

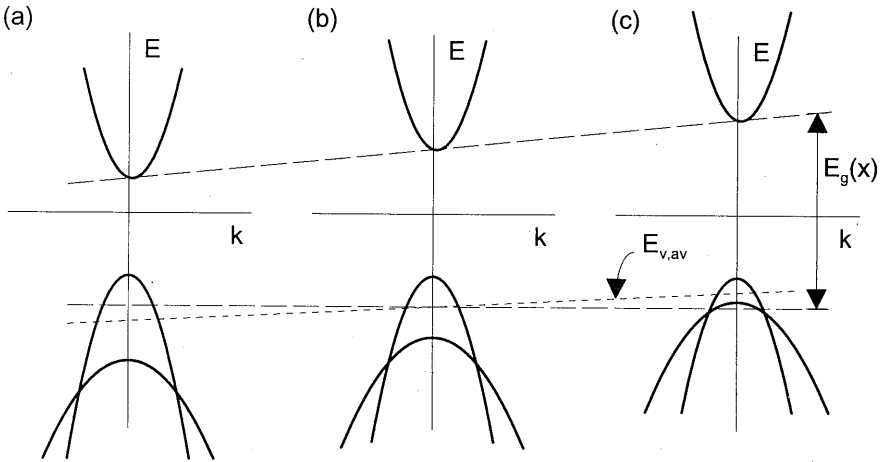


Fig. 2.5. Effect of strain on the in-plane dispersions of an $\text{In}_x\text{Ga}_{1-x}\text{As}/\text{InP}$ QW. (a) Compressive strain ($a_0 > a_{\text{sub}}$, $x > 0.53$), (b) Lattice matched ($a_0 = a_{\text{sub}}$, $x = 0.53$) and (c) tensile strain ($a_0 < a_{\text{sub}}$, $x < 0.53$).

Schrödinger equation can be found only when the field is applied either in the plane of the interfaces²⁷ or perpendicular to it. In this thesis we will only consider perpendicular magnetic fields.

The solution of the electron Schrödinger equation in a perpendicular magnetic field B yields the famous Landau levels as solutions. The usual¹ procedure starts by making the substitution

$$k_\alpha = \frac{1}{i} \frac{\partial}{\partial \alpha} + \frac{e}{\hbar} A_\alpha, \quad \alpha = \{x, y, z\} \quad (2.25)$$

in Eq. (2.13) and adding the Zeeman term $g^* \mu_B \sigma \cdot B$. The A_α are the components of the magnetic vector potential \mathbf{A} ($\mathbf{B} = \nabla \times \mathbf{A}$) for which the Landau gauge $\mathbf{A} = (-By, 0, 0)$ is chosen. The spin and spatial coordinates do not couple and the spin and spatial Hamiltonians can be separated. The eigenvalues of the spin part are simply² $\pm \frac{1}{2} g^* \mu_B B$. The spatial part forms a harmonic oscillator problem with eigenvalues $(N - \frac{1}{2}) \hbar \omega_c$. Note that the lowest Landau level has $N = 1$. The total electron energies in a perpendicular magnetic field are thus given by

$$E_N^{1,1} = \left(N - \frac{1}{2}\right) \hbar \omega_c \pm \frac{1}{2} g^* \mu_B B \quad (2.26)$$

Where the plus (minus) sign corresponds to spin up (down) and g^* and μ_B are the g -factor and the Bohr magneton, respectively. The cyclotron frequency ω_c is given by $\omega_c = eB/m_c^*$, with m_c^* the cyclotron effective mass. Corrections for electron non-parabolicity can easily be applied using Eq. (2.14) where $\epsilon(\mathbf{k}_\parallel, k_z)$ is replaced by

$$\epsilon(B, n, \hat{k}_z) = E_N^{1,1} + \frac{\hbar^2 \langle k_z^2 \rangle}{2m^*} \quad (2.27)$$

The inclusion of a magnetic field in the Luttinger Hamiltonian Eq. (2.16) is somewhat more complicated^{28,29,30}. The first step of the procedure is the same as for the electronic Hamiltonian, i.e. the numbers k_x and k_y are replaced by their operator forms Eq. (2.25). Now we introduce the ladder operators a and a^\dagger :

$$\begin{aligned} a &= \frac{l_c}{\sqrt{2}} (\hat{k}_x + i\hat{k}_y) \\ a^\dagger &= \frac{l_c}{\sqrt{2}} (\hat{k}_x - i\hat{k}_y) \end{aligned} \quad (2.28)$$

where l_c is the magnetic length, $l_c^2 = \hbar/eB$. The operators a and a^\dagger do not commute, $(a, a^\dagger) = 1$, and have the properties

$$\begin{aligned} a^\dagger u_N &= \sqrt{N+1} u_{N+1} \\ a u_N &= \sqrt{N} u_{N-1} \\ a^\dagger a u_N &= N u_N \end{aligned} \quad (2.29)$$

where the u_N are the harmonic oscillator eigenfunctions that vanish for negative N , $u_N = 0$ if $N < 0$. For the properties Eq. (2.29) a and a^\dagger are also called the annihilation and creation operator, respectively. When we now express k_x and k_y in the Luttinger Hamiltonian in terms of the operators a and a^\dagger , and let the resulting matrix work on the spinor

$$G_N = \begin{bmatrix} g_N^{h^+}(z) u_{N-2} \\ g_N^{l^-}(z) u_N \\ g_N^{l^+}(z) u_{N-1} \\ g_N^{h^-}(z) u_{N+1} \end{bmatrix} \quad (2.30)$$

we find that G_N is an eigenvector of \underline{H}_{Lut} when the axial approximation is applied, i.e. $\gamma_2 = \gamma_3$. For GaAs $\gamma_2 = 2.1$ and $\gamma_3 = 2.9$ so the neglect of the valence band anisotropy (or warping) is a reasonable approximation. Formally the total hole Hamiltonian in a magnetic field can therefore be written as

$$\underline{H}_{Lut}(a, a^\dagger, \hat{k}_z) = \underline{H}_{ax}(N, \hat{k}_z) + \underline{H}_w(a, a^\dagger) \quad (2.31)$$

with

$$\underline{H}_{ax} = \frac{\hbar^2}{m_0} \begin{bmatrix} \frac{\gamma_1 + \gamma_2}{l_c^2} \frac{2N-3}{2} + \frac{\gamma_1 - 2\gamma_2}{2} k_z^2 & -\frac{\sqrt{3}}{l_c^2} \gamma \sqrt{(N-1)N} & -\frac{\sqrt{6}}{l_c} \gamma_3 \sqrt{N-1} k_z & 0 \\ -\frac{\sqrt{3}}{l_c^2} \gamma \sqrt{(N-1)N} & \frac{\gamma_1 - \gamma_2}{l_c^2} \frac{2N+1}{2} + \frac{\gamma_1 + 2\gamma_2}{2} k_z^2 & 0 & \frac{\sqrt{6}}{l_c} \gamma_3 \sqrt{N+1} k_z \\ -\frac{\sqrt{6}}{l_c} \gamma_3 \sqrt{N-1} k_z & 0 & \frac{\gamma_1 - \gamma_2}{l_c^2} \frac{2N-1}{2} + \frac{\gamma_1 + 2\gamma_2}{2} k_z^2 & \frac{\sqrt{3}}{l_c^2} \gamma \sqrt{(N+1)N} \\ 0 & \frac{\sqrt{6}}{l_c} \gamma_3 \sqrt{N+1} k_z & -\frac{\sqrt{3}}{l_c^2} \gamma \sqrt{(N+1)N} & \frac{\gamma_1 + \gamma_2}{l_c^2} \frac{2N+3}{2} + \frac{\gamma_1 - 2\gamma_2}{2} k_z^2 \end{bmatrix} \quad (2.32)$$

where $\gamma = (\gamma_2 + \gamma_3)/2$. Since $u_N = 0$ for $N < 0$, the corresponding elements in Eq. (2.32) should be set to zero, and Eq. (2.32) is reduced to 3×3 , 2×2 , 1×1 for $N = 1, 0, -1$ respectively. The warping Hamiltonian is given by

$$\underline{H}_w = \frac{\hbar^2}{m_0} \begin{bmatrix} 0 & c_w & 0 & 0 \\ c_w^\dagger & 0 & 0 & 0 \\ 0 & 0 & 0 & c_w \\ 0 & 0 & c_w^\dagger & 0 \end{bmatrix}, \quad c_w = \frac{\sqrt{3}}{l_c^2} \mu (a^\dagger)^2, \quad \mu = \frac{\gamma_3 - \gamma_2}{2} \quad (2.33)$$

The warping Hamiltonian \underline{H}_w couples solutions Ψ_N to $\Psi_{N \pm 4}$. Therefore, an exact solution of the hole eigenvalue equation requires that an infinite number of hole Landau levels is taken into account. As this is not very attractive with respect to the processor time required for the solution of the corresponding eigenvalue equation, a different

approach is followed. First, the exact solutions of the unwarped problem are calculated. These eigenfunctions are then used as a basis in which the solutions of the total Hamiltonian are expanded, using perturbation theory.

The total hole eigenvalue equation that has to be solved in the first, exact, step is given by

$$\left[\underline{H}_{ax} + \frac{\hbar^2 \kappa}{l_c^2 m_0} \underline{M}_j + U(z) \right] G_N^j = E_N^j G_N^j \quad (2.34)$$

The suffixes N and j label the Landau level number and the band, respectively. The second term in Eq. (2.34), in which κ is the hole g -factor, describes the Zeeman splitting of the holes. \underline{M}_j is a 4*4 matrix with zeros at all positions but the diagonal elements, which equal m_j , i.e. 3/2, -1/2, 1/2, -3/2, respectively. Note that the lowest Landau level of a band does not necessarily have $N=1$, e.g. the heavy holes down have $N=-1$ as lowest Landau level.

The Schrödinger equation to solve in the second step can, using the definitions given above, be written as

$$\left(\underline{H}'_{ax} + \underline{H}_w \right) X_M^k = E_{w,M}^k X_M^k \quad (2.35)$$

where \underline{H}'_{ax} denotes the total expression between square brackets in Eq. (2.34). Since we have

$$\underline{H}_{ax} G_N^j = E_N^j G_N^j \quad (2.36)$$

and

$$\langle G_N^j | G_{N'}^{j'} \rangle = \delta_{jj'} \delta_{N,N'} \quad (2.37)$$

we can use the eigenfunctions of Eq. (2.34) as an orthonormal basis for the eigenfunctions of Eq. (2.35):

$$X_M^k = \sum_{j,N} c_N^j G_N^j \quad (2.38)$$

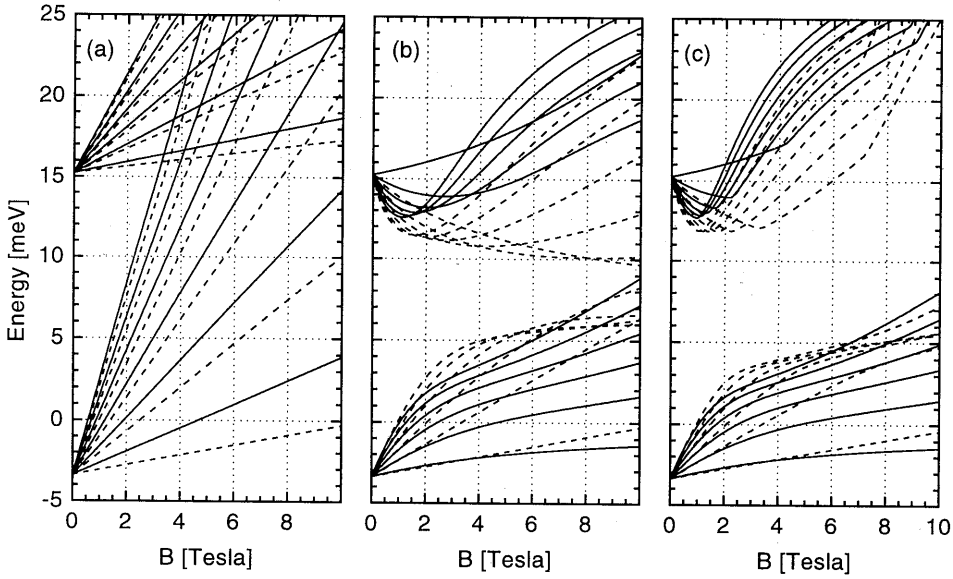


Fig. 2.6. Calculated Landau levels of the lowest hole subbands in a 90 Å GaAs/Al_{0.45}Ga_{0.55}As QW with $p=5 \cdot 10^{15} \text{ m}^{-2}$. (a) Diagonal approximation. (b) Axial approximation (i.e. warping neglected). (c) Full calculation. The solid (dashed) lines denote 'spin' up (down) subbands.

Substitution of Eq. (2.38) in Eq. (2.35) and taking the inner product with $G_{N'}^{j'}$ gives, with the use of Eqs. (2.36) and (2.37),

$$E_{N'}^{j'} c_{N'}^{j'} + \sum_{j,N} c_N^j \langle G_{N'}^{j'} | \underline{H}_w | G_N^j \rangle = E_{w,M}^k c_{N'}^{j'} \quad (2.39)$$

This is the new eigenvalue problem to solve. Since \underline{H}_w does not contain any operators after it has been applied to spinor Eq. (2.30), the solution of Eq. (2.39) requires a simple scalar matrix to be diagonalized. This matrix has in principle still an infinite number of rows and columns, but as it only couples states with index N to states with index $N \pm 4$, a limited calculation that includes L Landau levels of each band will yield reliable results for the lowest $L-4$ or $L-8$ Landau levels. Typically, we have used $L=24$.

We end this paragraph with a few notes on the interpretation of the eigenvalue equations (2.34) and (2.39). At the limit $B=0$ all off-diagonal elements in Eqs. (2.32) and

(2.33) vanish¹ and two points should be noted. Firstly, the warping Hamiltonian vanishes. Secondly, the decoupled Schrödinger equations are just the same as at $k_{\parallel}=0$ in (2.18), which of course should be the case. When the magnetic field is made non-zero, but the off-diagonal elements are still neglected, linear Landau levels are found, with a field dependence that is characterized by the in-plane effective mass $1/(\gamma_1 \pm \gamma_2)$. The off-diagonal elements of Eq. (2.32) again couple states of different m_j but, as Eq. (2.30) is an eigenvector, N is still a good quantum number of the axial problem. Therefore Landau levels with different N are allowed to cross and only levels with the same N must anticross. The warping Hamiltonian Eq. (2.33) mixes states with quantum number N to states with $N \pm 4$, so N is no longer a good quantum number. In fact four groups of Landau levels are formed in which the levels do interact with other levels in the group, but that do not interact with levels of different groups. In the chapter on magneto-transport (chapter 6) it will be shown that the warping interaction is of key importance in the calculation of realistic effective hole masses. Fig. 2.6 illustrates the above for the p-type GaAs/Al_{0.45}Ga_{0.55}As quantum well of 90 Å width and density $p=5 \times 10^{15} \text{ m}^{-2}$. Note that the lowest heavy hole down Landau level ($N=-1$) is the same in all three panels of Fig. 2.6, due to the absence of interactions with other levels. Comparison of panels (b) and (c) shows that the warping ‘compresses’ the L0 and H0 Landau fans, which can be expressed as a reduction of the effective hole mass. In chapter 6 we will come back to this point.

2.4 Many-body interactions

In the derivation of the Hamiltonians discussed in the previous paragraphs, interactions between particles have been neglected. For empty or almost empty, say n , $p \leq 5 \times 10^{14} \text{ m}^{-2}$, heterostructures this is a valid approximation. At higher carrier densities significant deviations from this one-particle approximation arise. In the following we briefly discuss three corrections to this approximation, namely the Hartree term, the Fock or exchange term and the correlation correction. As the latter two contributions lead to a reduction of the hole and electron eigenenergies, their combined effect is also known

¹ In fact, they vanish for finite N . In order to describe states at energies above the $k_{\parallel}=0$ energy in this formalism, N should approach infinity as B approaches zero. In this case the off-diagonal elements do not vanish, and the zero-field Hamiltonian Eq. (2.16) is retrieved.

as band-gap renormalization (BGR).

2.4.1 The Hartree term: the Poisson equation

The Hartree term accounts for the classical electron-electron (or hole-hole) Coulomb interaction. It amounts to replacing the exact many-electrons potential by an average one. For a system that is completely homogeneous in the x-y plane, cf. Eq. (2.12), the Hartree contribution V_H to the electrostatic potential $U_{c,v}$ is given by the one dimensional Poisson equation

$$\frac{\partial^2}{\partial z^2} V_H(z) = -\frac{e}{\epsilon_0 \epsilon_r} \rho(z) \quad (2.40)$$

with e the (positive) proton charge. The charge density $\rho(z)$ includes, apart from the occupied electron or hole states, also the distribution of ionized impurities, either due to background or doping. Furthermore, for 2D hole gases, the hole wave function is k dependent. The total charge density is then given by

$$\rho(z) = \pm e \sum_i \int dk_{\parallel} |H_i(\mathbf{k}_{\parallel}, z)|^2 f(E_i(\mathbf{k}_{\parallel}) - E_F) + eN_{don}(z) - eN_{acc}(z) \quad (2.41)$$

where the plus (minus) sign in the first term on the right hand side refers to a 2D hole (electron) gas and f is the Fermi-Dirac distribution function. H_i is the envelope function of the i -th subband of either the conduction or the valence band [cf. F_i in Eq. (2.13) and G_i in Eq. (2.18)]. For 2D electron gases the envelope functions are k_{\parallel} -independent, cf. Eq. (2.13), and the integration in Eq. (2.41) can be replaced by $n_i |H_i(\mathbf{k}_0, z)|^2$ with n_i the subband occupancy. It turns out that a similar replacement yields good results for hole gases in most structures as well. An exception to this rule are the center-delta-doped quantum wells that are discussed in chapter 7.

It should be pointed out that, in contrast to the exchange and correlation potentials that are discussed below, the Hartree potential is equal for electrons and holes.

2.4.2 Band gap renormalization: exchange and correlation

In the Poisson equation (2.40), the fermion character of the holes or electrons has

been neglected. Inclusion of the fermion character leads to the exchange interaction. Furthermore, the distribution of carriers in the x-y plane was assumed to be homogeneous. However, due to inter-particle Coulomb repulsion, the carriers are generally spatially correlated, which can lower their total energy. This process is generally referred to as the correlation interaction.

It is assumed that both interactions can be accounted for by an effective potential that is a scalar function of the local density in the heterostructure $\rho(z)$. This method is known as the local density approximation or LDA. In the local density approximation, the exchange and correlation potentials are related to the exchange and correlation energies ϵ_x and ϵ_c per particle of a homogeneous 3D hole or electron gas of density ρ by

$$V_{x,c}(z) = -\frac{d}{d\rho}[\rho\epsilon_{x,c}(\rho)](z) = -\epsilon_{x,c}(\rho(z)) - \rho(z)\frac{d}{d\rho}[\epsilon_{x,c}(\rho)](z) \quad (2.42)$$

Although the applicability of the LDA to (quasi) two dimensional structures still is, subject of discussion, it yields results that agree well with experiments. According to Langreth and Mehl³¹, the use of the LDA for an electron gas in a quantum well is justified as long as $r_s a_0 \ll 5d$, with d the width of the quantum well. The effective Bohr radius a_0 and dimensionless Wigner-Seitz radius r_s are defined by

$$a_0 = \frac{4\pi\epsilon_r\epsilon_0\hbar^2}{m_h e^2} \quad (2.43)$$

$$r_s = \frac{1}{\left(\frac{4\pi}{3}\right)^{1/3} a_0 \rho^{1/3}} \quad (2.44)$$

with ρ the three-dimensional carrier density in the quantum well. For future purposes we now also define the effective Rydberg Ry

$$Ry = \frac{\hbar^2}{2m_h a_0^2} \quad (2.45)$$

Qualitatively, the criterium of Langreth and Mehl is expected to hold for holes as well. In the samples considered in this thesis we have $r_s \lesssim 5$, $a_0 \approx 11 \text{ \AA}$ and $d \approx 50 - 100 \text{ \AA}$, so this

condition is indeed satisfied.

The origin of the exchange interaction will be illustrated with an example. Consider a two-particle system, where the two particles can be either electrons or holes. Their single-particle wave functions, i.e. the wave functions of the non-interacting particles, are $\Psi_1(\mathbf{r}_1)$ and $\Psi_2(\mathbf{r}_2)$, respectively. In the lowest approximation, the total two-particle wave function is simply their product, $F = \Psi_1(\mathbf{r}_1) \cdot \Psi_2(\mathbf{r}_2)$. However, the Fermion character of the particles requires that the total wave function is anti-symmetric under the interchange of the spatial coordinates of two particles. Such an anti-symmetric wave function can be constructed from single particle wave functions by means of a Slater determinant². For our two-particle system we have

$$F(\mathbf{r}_1, \mathbf{r}_2) = \frac{1}{\sqrt{2!}} \begin{vmatrix} \Psi_1(\mathbf{r}_1) & \Psi_1(\mathbf{r}_2) \\ \Psi_2(\mathbf{r}_1) & \Psi_2(\mathbf{r}_2) \end{vmatrix} = \frac{1}{\sqrt{2}} [\Psi_1(\mathbf{r}_1)\Psi_2(\mathbf{r}_2) - \Psi_1(\mathbf{r}_2)\Psi_2(\mathbf{r}_1)] \quad (2.46)$$

When we now wish to calculate the expectation value of the Coulomb interaction, $\langle V \rangle = \langle F | V | F \rangle$, we find

$$\langle V \rangle = \frac{e^2}{4\pi\epsilon_r\epsilon_0} \int d\mathbf{r}_1 d\mathbf{r}_2 \frac{1}{|\mathbf{r}_1 - \mathbf{r}_2|} \left[|\Psi_1(\mathbf{r}_1)|^2 |\Psi_2(\mathbf{r}_2)|^2 - \Psi_1^*(\mathbf{r}_1) \Psi_1(\mathbf{r}_2) \Psi_2^*(\mathbf{r}_2) \Psi_2(\mathbf{r}_1) \right] \quad (2.47)$$

The second term between square brackets in Eq. (2.47) is the exchange contribution and would not have been found when a simple product wave function was taken for F . The first term is the Hartree contribution that, in 2D, is accounted for by the Hartree potential V_H , calculated from the Poisson equation (2.40).

The correlation potential reflects the fact that charged particles of equal charging tend to avoid one another. By doing so they can reduce the total energy of the ensemble. At extremely low temperatures this leads to the famous Wigner solid.

Unfortunately, the actual calculation of exchange and correlation energies is rather complicated, particularly for holes when the complications arising from the coupling of the valence bands are included³². Therefore only the parametrized results of Bobbert *et al.*³² will be given here. These describe the hole exchange and correlation energies in a homogeneous 3D hole gas. Various authors have already studied these energies for homogeneous electron gases³³. It should be pointed out that the calculations for electron systems can not straightforwardly be extended to hole systems, see Ref [32] and the discussion below and in chapter 7.

The results are all given in effective Rydbergs, see Eq. (2.45). For the exchange

energy per hole Bobbert *et al.* find

$$\epsilon_x = -\zeta(w) \frac{3}{2} \left(\frac{9}{4\pi^2} \right)^{1/3} \frac{1}{r_s} Ry \quad (2.48)$$

which equals the exchange energy of an electron gas at the same density, apart from the numerical function $\zeta(w)$:

$$\zeta(w) \approx 2^{-1/3} + (1-w)^2 [w^2(aw+b) + c(4w^3 + 3w^2 + 2w + 1)] \quad (2.49)$$

where w is the ratio between the light and heavy hole Fermi wave vectors in bulk:

$$w \equiv \frac{k_{F,l}}{k_{F,h}} = \sqrt{\frac{m_l}{m_h}} \quad (2.50)$$

The hole effective masses m_l and m_h are here defined as

$$m_l = \frac{m_0}{\gamma_1 + 2\gamma}, \quad m_h = \frac{m_0}{\gamma_1 - 2\gamma} \quad (2.51)$$

$$\gamma = \sqrt{\frac{2\gamma_2^2 + 3\gamma_3^2}{5}}$$

The parameters a , b and c in Eq. (2.49) are $a=0.679$, $b=-0.0686$ and $c=1/4+3\pi^2/64-2^{-1/3} \approx -0.0811$. For $w=0$ and $w=1$ the function $\zeta(w)$ equals $\zeta(0) \approx 0.7126$ and $\zeta(1) \approx 0.7937$. The fact that the exchange energy is smaller for holes than for electrons, $\zeta(w)$ is smaller than unity for all w , reflects the fact that the $J=3/2$ quadruplet has four internal degrees of freedom, where the electron doublet $J=1/2$ only has two. Consequently, it is easier to fulfil the Pauli exclusion principle, which reduces the exchange interaction. Furthermore, for the hypothetical case $w=0$ the exchange energy is lower than for an electron gas at the same density although there is only one type of holes present.

The correlation energy per hole can, within one milli-effective Rydberg, be parametrized as³²:

$$\epsilon_c(w, r_s) \approx a(w) f(b(w) r_s) Ry \quad (2.52)$$

The function $f(x)$ is

$$f(x) = \begin{cases} -0.1358 - 0.0179x + 0.0752 \ln x + 0.0024x \ln x & (x \leq 1), \\ 1/(-2.2568 - 3.5742\sqrt{x} - 0.7017x) & (x > 1) \end{cases} \quad (2.53)$$

and the fitting polynomials for $a(w)$ and $b(w)$ are

$$\begin{aligned} a(w) &\approx 1 + 0.960(w-0.5) - 0.112(w-0.5)^2 - 0.454(w-0.5)^3 + 2.106(w-0.5)^4 \\ b(w) &\approx 1 + 0.364(w-0.5) - 1.056(w-0.5)^2 - 1.667(w-0.5)^3 + 1.865(w-0.5)^4 \end{aligned} \quad (2.54)$$

In order to calculate the total band gap renormalization of a p-type heterostructure, the electron-hole correlation potential, which accounts for the correlation between the valence band holes and a single conduction band electron, is also required. For GaAs and r_s around 5, this potential can be written as³²

$$V_c^e(r_s) \approx -\frac{1}{C\sqrt{r_s}[1 + Ar_s^{1/4} + Br_s^{1/8}]} Ry \quad (2.55)$$

with $A=4.526$, $B=1.956$ and $C=0.273$. Note that Eq. (2.55) describes a correction to the conduction band potential.

As an illustration of the above, Fig. 2.7 displays the total valence band potential of the p-type GaAs/Al_{0.45}Ga_{0.55}As quantum well of 90 Å width and density $p=5 \cdot 10^{15} \text{ m}^{-2}$, together with the Hartree and exchange-correlation potentials. The electron-hole correlation potential, affecting the total electron potential, is also shown. Note that the Poisson potential does not alter the band gap, as it is felt by both the electrons and holes, whereas all other potentials do reduce the band-gap, which is why their combined action is often labeled band-gap renormalization.

Below, two peculiarities of the exchange and correlation interactions in a hole gas, as expressed by the formulas presented above, will be discussed. First, the exchange-correlation potential for the valence band states is equal for 'heavy' and 'light' hole subbands, which may appear surprising at first sight. However, this is a direct consequence of the LDA formalism, which treats the 2D system locally as *bulk*. To be consistent, one therefore has to use the *bulk* dispersion relations for calculating the local fractions of heavy and light holes. Using this procedure, it is obviously no longer important whether a 2D subband is labeled 'heavy' or 'light', and the only important parameter becomes the *total* local hole density. This local density is then used to calculate the valence band exchange-correlation potential, that is equal for 'heavy' and

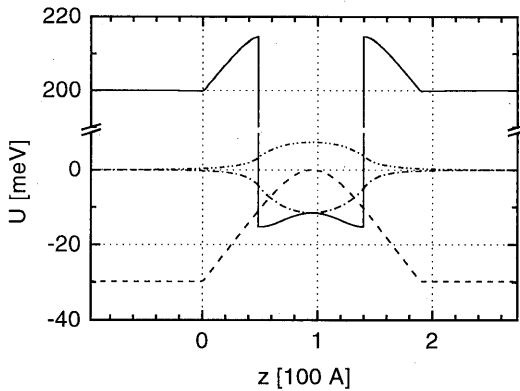


Fig. 2.7. Many-particle potentials for a 90 Å GaAs/Al_{0.45}Ga_{0.55}As QW with $p=5 \cdot 10^{15} \text{ m}^{-2}$. The solid line is the total valence band potential. The dashed line denotes the Hartree potential, the dash-dotted and dash-double-dotted lines denote the hole exchange-correlation potential and the electron-hole correlation potential, respectively. The kinks at $z=0$ and $z=140$ Å in the Hartree potential are due to the modulation doping planes at these positions.

'light' holes for the following reason. Although one can meaningfully assign an effective mass to a fraction of the total bulk density, in the sense that the dispersion relation of this fraction is characterized by this effective mass, there is no way of doing such a thing for an individual hole. In bulk, one can simply not identify a single hole as being 'light' or 'heavy' since the direction of J_z is fully arbitrary, and any superposition of hole basis states can be constructed for an individual hole. Furthermore, the Coulomb interaction is non-diagonal with respect to hole character. In other words, any scattering process, either scattering by an impurity or by

another hole, will in general change the character of the individual hole. Since the exchange and correlation interactions are nothing but inter-particle scattering processes, they must necessarily affect *all* valence band states. It should be stressed that no direct analogy can be made between hole character (m_h) and spin, since spin is conserved under Coulomb scattering, and hole character is not.

Second, occupied and unoccupied subbands experience the same exchange-correlation potential, which holds for both n- and p-type systems. For the correlation part of this potential this notion is more or less trivial, since the correlation is only driven by the Coulomb interaction. The equality of the exchange potentials for occupied and unoccupied subbands is less trivial, since the exchange interaction is only present between particles with an equal set of quantum numbers, which seems to exclude inter-subband exchange. However, although the subband index may be a good quantum number¹, the Coulomb interaction is non-diagonal with respect to this number. As an illustrative example, one may consider the exchange interaction between a particle in the

¹ The subband index is a good quantum number for parabolic particles. For holes, this is only the case for $k=0$, as discussed in paragraph 2.1.4.

heavy hole groundstate (H0) and one in the first excited heavy hole state (H1) of a symmetric QW. Using Eq. (2.47), where the H0 and H1 wave functions at $k=0$ are taken for Ψ_1 and Ψ_2 , will yield a non-zero result, although the direct inner product $\langle \Psi_1 | \Psi_2 \rangle$ is zero. The above is in marked contrast with several experiments on highly excited undoped quantum wells, in which it was shown that unoccupied subbands display far less renormalization than occupied subbands³⁴. On the other hand, in chapter 7 we find convincing evidence that, in p-doped quantum wells, occupied and unoccupied subbands experience the same exchange and correlation potential. Very likely, this difference is related to the fact that in the high-excitation experiments an equal number of electrons and holes is present in the structure, which situation electron-hole pairing can strongly alter the systems properties^{35,36}. It was shown by Bauer³⁶ that the occupied states in such a system can form an electron-hole condensate, that shows a far stronger renormalisation of the effective band gap than the unoccupied states. A further discussion of the model presented above and a comparison with other models for calculating the hole exchange-correlation potential and experiments, can be found in chapter 7.

2.5 Exciton (un)binding

Apart from electron-electron and hole-hole interactions that were discussed in the previous paragraph, also electron-hole interactions can strongly affect the physical properties of semiconductors, both in bulk and in systems of reduced dimensionality. This paragraph deals with the formation of excitons (bound electron-hole pairs) and their unbinding due to interactions with free carriers. Also the magnetic field dependence of the excitonic energy levels is briefly discussed. The excitons will be assumed to be free, i.e. not bound to impurities.

2.5.1 Free excitons in undoped heterostructures

Particularly in bulk semiconductors, a lot of insight can be gained by considering an exciton as a scaled hydrogen atom with an effective Rydberg Ry^* and an effective Bohr radius a_B^* that are scaled by the dielectric constant of the semiconductor ϵ_s and the reduced effective mass $\mu=(1/m_e+1/m_h)^{-1}$:

$$Ry^* = \frac{\mu^*}{m_0} \frac{1}{\epsilon_r^2} Ry, \quad Ry = 13.6 \text{ eV} \quad (2.56)$$

$$a_B^* = \epsilon_r \frac{m_0}{\mu^*} a_B, \quad a_B = 0.529 \text{ \AA}$$

For GaAs one has $\epsilon_r \approx 12.8$, $m_h \approx 0.4 m_0$ and $m_e \approx 0.067 m_0$ which gives $Ry^* \approx 4.7 \text{ meV}$ and $a_B^* \approx 118 \text{ \AA}$. For a perfectly two dimensional exciton Ry^* is enhanced by a factor 4 with respect to its bulk value, forming an upper bound for the exciton binding energy in a (quasi) 2D heterostructure. Two important conclusions can be drawn from these numbers. Firstly, the excitons under discussion here are large with respect to the GaAs lattice constant, so the envelope formalism is applicable. Secondly, the exciton binding energies are generally much smaller than the confinement energies of the lowest conduction and valence band states in e.g. quantum wells. Therefore the Coulomb interaction can, to a good approximation, be treated as a perturbation that does not alter the single particle wave functions. Under this assumption the total wave function of the exciton groundstate (1s) can in 2D be written as³⁷

$$F_{ex}(\mathbf{r}_\parallel, z) = F_0(z_e) G_0(z_h) \Phi_{rad}(\mathbf{r}_\parallel) \quad (2.57)$$

with the radial part given by^{37,38}

$$\Phi_{rad}(\mathbf{r}_\parallel) = \sqrt{\frac{2}{\pi}} \frac{1}{\lambda_{ex}} \exp\left(-\frac{r_\parallel}{\lambda_{ex}}\right) \quad (2.58)$$

where \mathbf{r}_\parallel is the in-plane spatial coordinate. The two-dimensional exciton radius λ_{ex} is determined variationally to minimize the exciton binding energy E_b

$$E_b(\lambda_{ex}) = -\frac{\hbar^2}{2\mu^* \lambda_{ex}^2} + \frac{e^2}{4\pi\epsilon_r\epsilon_0} \langle F_{ex} | \frac{1}{\rho} | F_{ex} \rangle \quad (2.59)$$

with $\rho = [r_\parallel^2 + (z_e - z_h)^2]^{1/2}$. In Eqs. (2.57-59) both holes and electrons were assumed to be characterized by a single effective mass. It is known that valence band non-parabolicity can strongly enhance the exciton binding energy with respect to its value in the parabolic approximation³⁹. This effect is particularly strong for the light hole ground state exciton in GaAs quantum wells, due to the negative light hole mass around the Γ point.

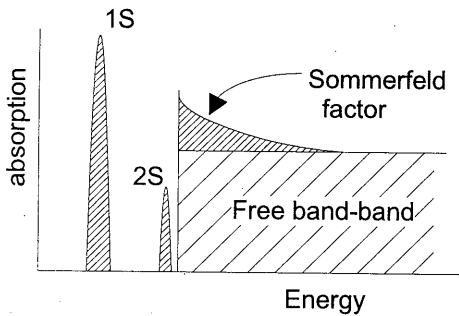


Fig. 2.8. Absorption spectrum of a 2D semiconductor. The hatched region is the free band-band absorption, the gray regions indicate excitonic effects.

Furthermore, the Coulomb interaction can mix the character of different subbands, which effect becomes more important in wider wells and for higher subbands. Extensive calculations that take these effects into account have appeared in the literature^{39,40,41,42}.

The formation of excitons has profound effects on the heterostructure absorption spectrum. Fig. 2.8 illustrates this schematically. Most pronounced are the 1s absorption peak and the enhancement of absorption over the excitonless value due to the Sommerfeld factor. This Sommerfeld enhancement is due to the continuum wave functions of the exciton, which represents the effect of electron-hole correlation in unbound states. In very high quality materials also the 2s and 3s peaks can be observed. With a schematic picture like Fig. 2.8 in mind, peaks in experimental absorption spectra are generally interpreted as being indicative for the presence of excitons. In chapters 4 and 5 it will be shown that this can be misleading.

2.5.2 Exciton bleaching by interactions with free carriers

When excitons coexist with other particles, either free electrons, free holes or other excitons, interactions with these other particles lead to a reduction of the exciton binding energy. This effect is generally referred to as exciton bleaching or exciton screening. In the following we will restrict the term 'screening' to a particular mechanism of exciton unbinding. In all experiments described in this thesis the exciton density is kept low, so exciton bleaching by interactions with other excitons can be neglected. Therefore, this will not be discussed here and only bleaching by free particles will, qualitatively, be discussed. Generally, three bleaching mechanisms are discerned: phase-space filling, exchange and Coulomb screening.

Phase-space filling is due to the fermion character of electrons and holes. Formally, one can think of an exciton as being built up out of products of free electron and hole states, cf. Eq. (2.57). When a state in the phase-space is occupied by a free particle, it can no longer be used in the formation of an exciton which leads to a

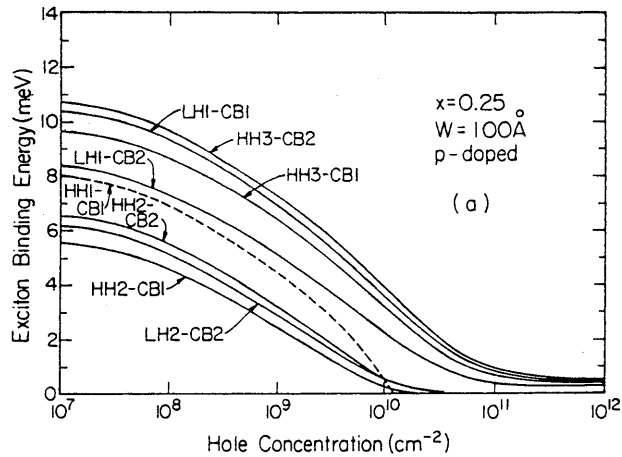


Fig. 2.9. Calculation of exciton binding energies in a p-doped GaAs/Al_{0.25}Ga_{0.75}As quantum well of 100 Å width with variable hole concentrations, taken from G. D. Sanders and Y. C. Chang, *Phys. Rev. B* 35, 4274 (1987). Note that the labeling differs from what is used throughout this thesis, e.g. HH1 is H0 in our notation, CB1 is E0 etc.

reduction of the exciton binding energy. A useful rule of thumb for estimating the density at which excitons are unbound by this mechanism is $a_B^* \approx 1/k_F$ ⁴³

Exchange interaction is also due to the fermion character of the electrons and holes. As this interaction was discussed in some detail in paragraph 2.4.2, it will not be further discussed here. Its bleaching effectiveness is about the same as that of the phase-space filling mechanism³⁸.

Coulomb screening is, unlike the two mechanisms discussed above, not restricted to excitons of occupied subbands. Qualitatively, Coulomb screening can be thought of as a rearrangement of free carriers in the presence of a disturbing electrostatic potential, e.g. of a photo-created electron or hole, which compensates the disturbing potential. It is usually accounted for by a dielectric constant $\epsilon(q)$ that modifies the electron-hole interaction¹. It can be shown⁴⁴ that for purely two-dimensional systems Coulomb screening cannot fully unbind the exciton, in the sense that at least one bound state (1s) always remains although its binding energy can be infinitesimally small. The two other bleaching mechanisms can totally unbind the exciton.

Fig. 2.9 illustrates the effects of phase-space filling and Coulomb screening in a 100 Å GaAs / Al_{0.25}Ga_{0.75}As quantum well. Clearly, the exciton of the occupied subband, represented by the dashed line, is totally unbound at a finite density. All other excitons

approach zero binding energy asymptotically, characteristic of Coulomb screening in 2D. The limits of the 2D approach to exciton screening will be discussed further in chapter 5. The enhancement of absorption strength, sketched in Fig. 2.8, vanishes, more or less parallel, with decreasing exciton binding energy.

2.5.3 Excitons in a magnetic field

The calculation of the energy levels of a quasi 2D exciton subjected to a perpendicular magnetic field is a far from trivial task. Even when hole and electron non-parabolicity are neglected, analytical expressions can only be derived in the high and low field limit. In all other situations, one has to rely on numerical solutions of the exciton Hamiltonian. Formally, one can write the exciton Hamiltonian as

$$H_{ex} = T_e(B, \hat{k}_z) + T_h(B, \hat{k}_z) + U_c(z) + U_v(z) + V_{e-h}(\mathbf{r}_e - \mathbf{r}_h) \quad (2.60)$$

where $T_{e(h)}$ is the kinetic energy of the electron (hole), $U_{c(v)}$ the confining conduction (valence) band potential and V_{e-h} the electron hole interaction. Taking the 4*4 Luttinger Hamiltonian for T_h , Bauer and Ando⁴¹ and Yang and Sham⁴⁵ have solved, but their discussion is beyond the scope of this chapter(2.60). As this procedure is extremely laborious, we will follow another approach that yields an approximate solution of Eq. (2.60). For a full discussion of the strengths and weaknesses of this method, the reader is referred to chapter 5. We solve the electron and hole Hamiltonians in a magnetic field separately and correct for the exciton binding energy afterwards. The field-dependent exciton binding energy is assumed to be the same as for the scaled 2D hydrogen atom, that is discussed by MacDonald and Ritchie⁴⁶. Our procedure is that we replace the linear contributions of the electron and hole, $\sim \hbar\omega_c^{e,h}(N-1/2)$, to the energy of the N -s state of the scaled hydrogen atom by more realistic Landau levels from Eqs. (2.26), (2.14) and (2.34). The exciton binding energy at zero field, $4Ry^*$, is used as a free parameter. In the following, the magnetic field dependency of the energy levels of the scaled two-dimensional hydrogen atom will be discussed, in which we will follow MacDonald and Ritchie⁴⁶.

In discussing excitonic levels, it is convenient to characterize the Coulombic and magnetic energy scales in terms of the effective Rydberg, see (2.56), and the cyclotron energy $\hbar\omega_c^*$ with $\omega_c^* = eB/\mu^*$, respectively. Furthermore, it is convenient to define their ratio γ :

$$\gamma \equiv \frac{\hbar\omega_c^*}{2Ry^*} \quad (2.61)$$

In the low magnetic field regime, i.e. $\gamma \ll 1$, the magnetic field may be treated as a perturbation to the zero-field hydrogenic levels. For the energy of the N -s ($L=0$) excitonic level one then finds⁴⁶

$$E_{ex}(N,B,Ry^*) = \left[-\frac{1}{(N-1/2)^2} + c_N \frac{\gamma^2}{4} \right] Ry^* \quad (2.62)$$

The coefficients c_N are for the lowest four s-states $c_1=3/8$, $c_2=14\ 5/8$, $c_3=103\ 1/8$ and $c_4=385\ 7/8$. The first term between brackets can be interpreted as the zero field binding energy of an N -s hydrogenic state, the second can be interpreted as its diamagnetic shift.

In the high field limit, i.e. $\gamma \gg 1$, the Coulomb interaction can be treated as a perturbation on the free electron and hole Landau levels. The excitonic energy levels for the N -s states are then given by⁴⁶

$$E_{ex}(N,B,Ry^*) = \left[2\gamma \left(N - \frac{1}{2} \right) - d_N \sqrt{2\pi\gamma} \right] Ry^* \quad (2.63)$$

The dimensionless coefficients d_N are, for the lowest four excitonic Landau levels $d_1=1$, $d_2=3/4$, $d_3=41/64$ and $d_4=147/256$. The first term between brackets describes the field dependence of the unperturbed Landau level with index N , the second term is a correction term that is proportional to $B^{1/2}$.

For intermediate fields, MacDonald and Ritchie⁴⁶ have constructed an interpolation scheme that reproduces the high and low field results Eqs. (2.62) and (2.63) and interpolates between them. This interpolation scheme shows accurate agreement with a numerical solution of the two-dimensional hydrogen Hamiltonian⁴⁷. As the use of this interpolation scheme is much faster than the numerical solution of the aforementioned Hamiltonian, we apply the former method to calculate excitonic energies at arbitrary fields.

2.6 The Broido-Sham transformation, interface conditions and numerical solutions

In this paragraph miscellaneous topics that are related to the numerical solution of the eigenvalue problems introduced in the preceding paragraphs, will be discussed.

2.6.1 The Broido-Sham transformation

The hole eigenvalue equation (2.18) describes a set of four coupled complex second order differential equations which forms a rather unfriendly system to solve. Using a unitary transformation \underline{U} it is possible to block-diagonalize the Luttinger Hamiltonian⁴⁸, i.e. $\underline{H}_{Lut}' = \underline{U}\underline{H}_{Lut}\underline{U}^\dagger$ is block diagonal. The transformation matrix \underline{U} is

$$\underline{U} = \frac{1}{\sqrt{2}} \begin{bmatrix} e^{-i\phi} & 0 & 0 & -e^{i\phi} \\ 0 & e^{-i\eta} & -e^{i\eta} & 0 \\ 0 & e^{-i\eta} & e^{i\eta} & 0 \\ e^{-i\phi} & 0 & 0 & e^{i\phi} \end{bmatrix} \quad (2.64)$$

This transformation is generally referred to as the Broido-Sham transformation. It mixes 'spin' up and down components but the heavy and light characters are conserved in the new basis. The angles ϕ and η are given by⁴⁹

$$\begin{aligned} \phi &= \frac{\Theta_b + \Theta_c}{2} + \frac{\pi}{4} \\ \eta &= \frac{\Theta_b - \Theta_c}{2} + \frac{\pi}{4} \end{aligned} \quad (2.65)$$

where Θ_b and Θ_c are the phase angles of the elements b and c in the Luttinger Hamiltonian, see Eq. (2.17). The transformed Luttinger Hamiltonian is

$$\underline{H}_{Lut}'(k_x, k_y, \hat{k}_z) = \frac{\hbar^2}{2m_0} \begin{bmatrix} H_h & \tilde{c} & 0 & 0 \\ \tilde{c}^\dagger & H_l & 0 & 0 \\ 0 & 0 & H_l & \tilde{c} \\ 0 & 0 & \tilde{c}^\dagger & H_h \end{bmatrix}, \quad \tilde{c} = |c| - i|b| \quad (2.66)$$

The symbols have the same meaning as in Eq. (2.16). Note also that the Hamiltonian Eq. (2.66) is real. The eigenvalue equation (2.18) remains unaltered, apart from the replacement of \underline{H}_{Lut} by \underline{H}_{Lut}' .

2.6.2 Interface conditions

In semiconductor heterostructures the material parameters, m^* and the γ_i 's, are usually different in each material layer. Consequently they become a function of z and do no longer commute with $\partial/\partial z$ and $\partial^2/\partial z^2$ at the interfaces. The usual cure for this problem is to replace all products of material constants and operators by their anti-commutator $\{a,b\} = (ab+ba)$. One obtains the following substitutions

$$\begin{aligned} \gamma_i \frac{\partial^2}{\partial x^2} &\rightarrow \frac{\partial}{\partial x} \gamma_i \frac{\partial}{\partial x} \\ \gamma_i \frac{\partial}{\partial x} &\rightarrow \frac{1}{2} \left\{ \gamma_i, \frac{\partial}{\partial x} \right\} \end{aligned} \quad (2.67)$$

and similarly for m^* . With this transformation, the electron and hole Hamiltonians still contain elements of the form $\partial/\partial z \gamma_i$ which is numerically undesirable since γ_i is usually assumed to be a step-like function of z . An elegant way around this numerical problem exists in the real-space approach that is used to solve the eigenvalue problems¹¹. Moreover, this method automatically fulfills the usual flux conserving interface conditions⁵⁰ and will be discussed in the next section.

2.6.3 Real-space numerical solution

The solutions of the electron and hole eigenvalue problems are obtained using a numerical routine that solves a system of N coupled first order differential equations of the shape

$$\frac{\partial}{\partial z} y_i = f_i(x, y_1, y_2, \dots, y_N), \quad i=1, \dots, N \quad (2.68)$$

The second order differential equations in Eq. (2.18) are transformed to the shape Eq. (2.68) by collecting, in each second order equation, the terms containing derivatives of

γ_i to the left hand side. The terms under the derivative on the left hand side are then defined as new dependent variable of which continuity is required. The continuity of these new variables fulfils the flux conserving interface conditions. As the eigenenergy E_i is also unknown, it is also regarded as a dependent variable y_i , which satisfies the differential equation $\partial/\partial z E = 0$. The whole procedure sketched above is discussed in full detail by Goldoni and Fasolino⁵¹. A comparative discussion of other methods used to solve the hole eigenvalue problem and our method can be found in chapter 3.

References

1. G. Bastard, *Wave Mechanics Applied to Semiconductor Heterostructures* (Les Editions de Physique, Les Ulis, 1988)
2. S. Gasiorowicz, *Quantum Physics* (John Wiley and Sons, New York, 1974)
3. E. O. Kane, J. Phys. Chem. Sol. **1**, 249 (1957); E. O. Kane, *Physics of III-V Compounds*, Vol. 1, edited by R. K. Willardson and A. C. Beer (Academic Press, New York, 1966); E. O. Kane, *Narrow Gap Semiconductors. Physics and Applications* edited by W. Zawadzki, *Lect. Notes Phys.*, Vol. 133 (Springer Verlag, Berlin, 1980).
4. E. D. Palik, G. S. Picus, S. Teitler, and R. F. Wallis, Phys. Rev. **122**, 475 (1961).
5. F. Ancillotto, A. Fasolino, and J. C. Maan, Phys. Rev. B **38**, 1788 (1988).
6. G. Edwards, E. C. Valadares, F. W. Sheard, Phys. Rev. B **50**, 8493 (1994).
7. J. M. Luttinger and W. Kohn, Phys. Rev. **97**, 869 (1955); J. M. Luttinger, Phys. Rev. **102**, 1030 (1956).
8. *Physics of Group IV Elements and III-V Compounds*, edited by O. Madelung, M. Schultz, and H. Weiss, Landolt-Börnstein, New Series, Group III, Vol. 17, Pt. a (Springer-Verlag, Berlin, 1982); *ibid.*, Vol. 22, Pt. a (Springer-Verlag, Berlin, 1987).
9. See, e.g., J. A. Kash, M. Zachau, M. A. Tischler, and U. Ekenberg, Surf. Science **305**, 251 (1994) and references therein.
10. G. Bastard, Phys. Rev. B **24**, 5693 (1981).
11. G. Goldoni and A. Fasolino, Phys. Rev. Lett. **69**, 2567 (1992).
12. C. G. van de Walle, Phys. Rev. B **39**, 1871 (1989).
13. M. Peressi, S. Baroni, A. Baldereschi, and R. Resta, Phys. Rev. B **41**, 12106 (1990).
14. M. Peressi, L. Colombo, R. Resta, S. Baroni, and A. Baldereschi, Phys. Rev. B **48**, 12047 (1993).
15. A. Taguchi and T. Ohno, Phys. Rev. B **39**, 7803 (1989).
16. K. Kunc and R. M. Martin, Phys. Rev. B **24**, 3445 (1981).
17. C. G. van de Walle and R. M. Martin, Phys. Rev. B **34**, 5621 (1986).

18. C. G. van de Walle and R. M. Martin, *Phys. Rev. B* **35**, 8154 (1987).
19. R. People and J. C. Bean, *Appl. Phys. Lett.* **47**, 322 (1985); **49**, 229 (1986).
20. J. W. Matthews and A. E. Blakeslee, *J. Cryst. Growth* **27**, 118 (1974).
21. See, e.g., M. Sugawara, N. Okazaki, T. Fujii, and S. Yamazaki, *Phys. Rev. B* **48**, 8102 (1993) and references therein.
22. G. L. Bir and G. E. Picus, *Symmetry and Strain-Induced Effects in Semiconductors* (Wiley, New York, 1974)
23. F. H. Pollak and M. Cardona, *Phys. Rev.* **172**, 816 (1968).
24. E. P. O'Reilly, *Semicond. Sci. Technol.* **4**, 121 (1989).
25. S. C. Jain, M. Wilander, and H. Maes, *Semicond. Sci. Technol.* **11**, 641 (1996).
26. A. Ghiti and U. Ekenberg, *Semicond. Sci. Technol.* **9**, 1575 (1994).
27. A. F. W. van de Stadt, Ph.D. thesis, Eindhoven University of technology, 1998; H. Tang and P. N. Butcher, *J. Phys. C: Solid State Phys.* **21**, 3313 and 3959 (1988)
28. U. Ekenberg and M. Altarelli, *Phys. Rev. B* **32**, 3712 (1985).
29. S.-R. E. Yang, D. A. Broido, and L. J. Sham, *Phys. Rev. B* **32**, 6630 (1985).
30. E. Bangert and G. Landwehr, *Surf. Sci.* **170**, 593 (1986).
31. D. C. Langreth and M. J. Mehl, *Phys. Rev. B* **28**, 1809 (1983).
32. P. A. Bobbert, H. Wieldraaijer, R. van der Weide, M. Kemerink, P. M. Koenraad, and J. H. Wolter, *Phys. Rev. B* **56**, 3664 (1997).
33. L. Hedin and B. I. Lundqvist, *J. Phys. C: Solid St. Phys.* **4**, 2064 (1971); O. Gunnarson and B. I. Lundqvist, *Phys. Rev. B* **13**, 4274 (1976); J. P. Pedrew and A. Zunger, *Phys. Rev. B* **23**, 5048 (1982).
34. J.A. Levenson, I. Abram, R. Raj, G. Dolique, J. L. Oudar, and F. Alexandre, *Phys. Rev. B* **38**, 13443 (1988); C. Weber, C. Klingshirn, D. S. Chemla, D.A. B. Miller, J. E. Cunningham, and C. Ell, *ibid.* **38**, 12748 (1988)
35. M. Potemski, J. C. Maan, K. Ploog, and G. Weimann, *Solid State Commun.* **75**, 185 (1990); R. Cingolani, G. C. La Rocca, H. Kalt, K. Ploog, M. Potemski, and J. C. Maan, *Phys. Rev. B* **43**, 9662 (1991).

-
36. G. E. W. Bauer, Phys. Rev. Lett. **64**, 60 (1990).
 37. M. Sugawara, J. Appl. Phys. **71**, 277 (1992).
 38. S. Schmitt-Rink, D. S. Chemla, and D. A. B. Miller, Phys. Rev. B **32**, 6601 (1985).
 39. U. Ekenberg and M. Altarelli, Phys. Rev. B **35**, 7585 (1987).
 40. R. Winkler, Phys. Rev. B **51**, 14395 (1995).
 41. G. E. W. Bauer and T. Ando, Phys. Rev. B **38**, 6015 (1988).
 42. L. C. Andreani, Superlatt. Microstruct. **9**, 1 (1992).
 43. A. E. Ruckenstein and S. Schmitt-Rink, Phys. Rev. B **35**, 7551 (1987).
 44. J. A. Brum, G. Bastard, and C. Guillemot, Phys. Rev. B **30**, 905 (1984).
 45. S.-R. E Yang and L. J. Sham, Phys. Rev. Lett. **58**, 2598 (1987).
 46. A. H. MacDonalds and D. S. Ritchie, Phys. Rev. B **33**, 8336 (1986).
 47. M. Volk, S. Lutgen, T. Marschner, W. Stolz, E. O. Göbel, P. C. M. Christianen, and J. C. Maan, Phys. Rev. B **52**, 11096 (1995).
 48. D. A. Broido and L. J. Sham, Phys. Rev. B **31**, 888 (1985).
 49. S. L. Chuang, Phys. Rev. B **40**, 10379 (1989).
 50. See, e.g., M. Altarelli, *Heterojunctions and Semiconductor Superlattices*, edited by G. Allan, G. Bastard, N. Boccara, and M. Voos (Springer-Verlag, Berlin, 1986).
 51. G. Goldoni and A. Fasolino, Phys. Rev. B **51**, 9903 (1995).

3 Enhancement of spin-dependent hole delocalization in degenerate asymmetric double quantum wells

(published in Phys. Rev. B **53**, 10000 (1996) and Superlatt. Microstruct. **21**, 217 (1997))

3.1 Introduction

In the past decades the energy bands of low-dimensional semiconductor structures have been intensively studied, both by experimental and theoretical means. For the $J=1/2$ electron states, originating from S-type molecular orbitals, an almost parabolic behavior was found. Only for large wavenumbers and high magnetic fields, the deviations from parabolicity are significant. The valence band, in contrast, is strongly non-parabolic. Since the hole states are formed from P-type molecular orbitals ($L=1$), the spin-orbit interaction becomes important and splits the hole states in a spin-orbit split-off doublet with $J=1/2$ and a heavy hole-light hole quadruplet with $J=3/2$. The interactions between these bands result in strongly non-parabolic dispersion relations. Due to this complexity, it has only recently been recognized that structures can be developed that take advantage of the physical properties of the valence band, both to explore new physics and to improve device performance¹.

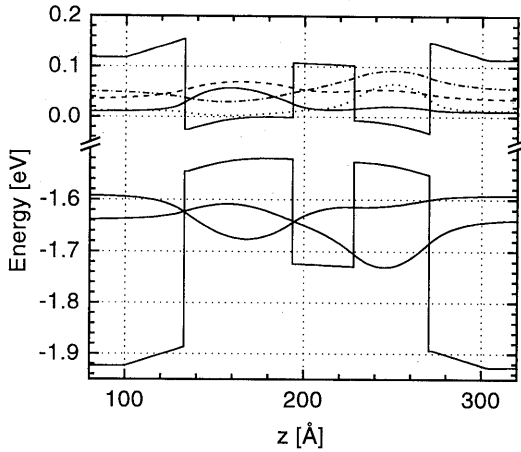


Fig. 3.1 Envelope functions of the first hole and electron levels in a self-consistent potential at zero in-plane wavevector. The wavefunctions are offset by their energy at $k=0$. The hole density is $1.5 \cdot 10^{16} \text{ m}^{-2}$. Hole levels, solid line, H0; dotted line, H1, dashed line, L0; dash-dotted line, L1. Electron levels, top to bottom: E0, E1.

One of the aforementioned structures that has been intensively studied in the past few years is the Asymmetric Double Quantum Well (ADQW)^[2-8], consisting of two (single) QW's of different width, separated by a tunnel-barrier, see Fig. 3.1. As a device application, such structures can, e.g., be used as bias-voltage tuneable infrared detectors^{2,3} or as velocity modulation transistors⁴. More fundamentally, ADQWs can show strong tunneling dependent level broadening when the scattering intensities in the left and right wells are different⁵. One of the most interesting features is the different leakage of hole wave functions of

different magnetic moment, leading to a *macroscopic* separation of 'spin' up and 'spin' down ($m_j = \pm 3/2$ or $\pm 1/2$) states. This effect was coined 'Spin-Dependent Hole Delocalization' (SDHD) by Goldoni and Fasolino^{6,7}. Due to the asymmetry of the potential, the degeneracy of the pseudo-spin m_j of the hole-levels is lifted, leading to spin dependent hole delocalization, even when there is no resonance between levels in the left and right well.

In most theoretical works dealing with ADQWs⁵⁻⁸ the effects of bandfilling on the hole states are not taken into account. These are essential to explain most experimental results quantitatively and as we point out, even qualitatively. In this chapter we will show the extreme sensitivity of the hole energy levels and optical oscillator strengths to the presence of a degenerate hole gas. Furthermore, we will show that the SDHD is strongly enhanced when the bandbending resulting from the presence of holes is included.

This chapter will be organized as follows: In paragraph 3.2 the theoretical framework in which the numerically exact solutions of both the Schrödinger and Poisson equations are obtained will be presented. In paragraph 3.3 numerical results will be presented which will be compared with experiments in paragraph 3.4. A summary will be given in paragraph 3.5.

3.2 Theory

In this paragraph we will outline our approach to solve the Luttinger Hamiltonian. We have used a commercially available routine to obtain exact eigenvalues and eigenfunctions from a set of coupled first-order differential equations. The used routine solves a two-point boundary-value problem, described by a set of coupled first-order differential equations, using a deferred correction technique and Newton iteration⁹. Since this method is not limited by a (finite) basis set of functions to expand the eigenstates in, it is numerically exact, i.e. within a user-specified tolerance, typically 10^{-5} . This is similar to expanding the eigenfunctions in an infinite basis-set.

In most theoretical studies^{10,11,12,13,14} on valence bands which appeared in the past decades, the hole eigenstates are expanded in a limited set of basisfunctions and are calculated by matrix diagonalization. This method is known to give rise to significant deviations for larger wavenumbers, unless the number of basis functions is drastically increased¹⁰. Other, exact, methods^{15,16,17} are only applicable to highly symmetric structures, such as empty single quantum wells. The method presented here is suited for any given potential, under the limitation that a good starting solution can be generated. Also the effects of strain or a magnetic field can easily be included¹⁸, and an easy access to wave functions and their derivatives is provided. However, in this chapter we will only be concerned with the asymmetric double quantum well in zero magnetic field. To calculate the hole energy levels we used the Luttinger Hamiltonian⁹, with inclusion of warping, in the spin-orbit basis with $m_j=(3/2,-1/2,1/2,-3/2)$. The confining potential U is assumed to be parallel to the z -axes, and hole-energy is counted positive. The split-off band components of the lowest hole levels of the $J=3/2$ multiplet are known to be negligible¹⁵, which reduces the Luttinger Hamiltonian to 4×4 . Furthermore we will neglect linear k terms, arising from the lack of inversion symmetry of the GaAs crystal, since they only give rise to small energy splittings^{11,20}.

$$\underline{H}_{Lut}(k_x, k_y, \hat{k}_z) = \frac{\hbar^2}{2m_0} \begin{bmatrix} H_h + U(z) & c & -b & 0 \\ c^\dagger & H_l + U(z) & 0 & b \\ -b^\dagger & 0 & H_l + U(z) & c \\ 0 & b^\dagger & c^\dagger & H_h + U(z) \end{bmatrix} \quad (3.1)$$

where

$$\begin{aligned}
H_h &= (k_x^2 + k_y^2)(\gamma_1 + \gamma_2) + \hat{k}_z^2(\gamma_1 - 2\gamma_2) \\
H_l &= (k_x^2 + k_y^2)(\gamma_1 - \gamma_2) + \hat{k}_z^2(\gamma_1 + 2\gamma_2) \\
b &= 2\sqrt{3}\gamma_3(k_x - ik_y)\hat{k}_z \\
c &= -\sqrt{3}[\gamma_2(k_x^2 - k_y^2) - 2i\gamma_3k_xk_y] \\
\hat{k}_z &= \frac{1}{i} \frac{\partial}{\partial z}
\end{aligned} \tag{3.2}$$

In order to reduce the numerical effort we have applied the Broido-Sham transformation^{11,21}, making Eq. (3.1) block-diagonal. The remaining set of coupled second-order differential equations is then transformed into first-order, giving two sets of six equations, when equations for normalization and energy continuity are included. Standard boundary conditions are applied at the outer boundaries of the calculation interval.

The choice between flux conservation or wave function continuity imposing interface conditions (IC), i.e. keeping $(1/m^*)(d\Psi/dz)$ or $(d\Psi/dz)$ continuous at the interfaces^{22,23}, can be made by simply taking the Luttinger parameters of the barrier material ($\text{Al}_x\text{Ga}_{1-x}\text{As}$) different or the same as those of the well material (GaAs), respectively. However, when flux-conserving IC are chosen, the Luttinger parameters γ_i become z -dependent and do no longer commute with the operators k_z and k_z^2 . Therefore

Level	empty structure		$p=1.5 \cdot 10^{+16} \text{ m}^{-2}$	
	$\frac{1}{m^*} \frac{\partial \Psi}{\partial z}$	$\frac{\partial \Psi}{\partial z}$	$\frac{1}{m^*} \frac{\partial \Psi}{\partial z}$	$\frac{\partial \Psi}{\partial z}$
H0	16.62	16.86	10.69	10.95
H1	27.10	27.58	12.62	12.56
L0	39.97	41.84	32.38	34.22
L1	63.81	68.37	48.32	52.52
E0	60.89	65.93	66.76	71.74
E1	93.55	104.21	107.81	118.49

Table 3.1 Energies in meV of the first two heavy, light and electron levels in a filled or empty ADQW (59.4 Å and 42.4 Å wells, 33.9 Å barrier) with 40% Al barriers for two different interface conditions, as indicated by the column headings. See text for further explanation.

expressions of the type $\gamma_i k_z$ and $\gamma_i k_z^2$ have to be replaced by their respective anti-commutators²⁴. Since we will assume low Al-content (25%) barriers, and focus on the lowest subbands, which penetrate only a few atomic layers into the barriers, the difference between the two approaches will be small, and will generally fall below experimental resolution. For the standard structure of paragraph 3.3 we have listed the first heavy, light and electron levels in Table 3.1, for both interface conditions. In the remainder of this paper we have applied the wave function continuity imposing IC's, unless stated otherwise. The parameters used in the calculations are $\gamma_1=6.85$, $\gamma_2=2.1$ and $\gamma_3=2.9$ for GaAs and $\gamma_1=3.45$, $\gamma_2=0.68$ and $\gamma_3=1.29$ for AlAs²⁵. Intermediate values are calculated using linear interpolation.

The actual calculation is split in two parts, a part for $k=0$ in which self-consistency is obtained, and one for finite k . The $k=0$ calculation starts with solving Eq. (3.1) for a flatband potential, taking advantage of the fact that Eq. (3.1) decouples into four Schrödinger-type equations, which are easily solvable. The starting solutions for this procedure are generated as even and odd combinations of half or whole-period sines, localized entirely in the separate wells. For the lowest subbands (a half period-sinus in each well) the even combinations correspond to the lowest energy, see Fig. 3.1.

The wave functions obtained in this way are used to calculate the charge distribution $\rho(z)$ in the system. Poisson's equation is then solved by numerical integration of $\rho(z)$ and the charged acceptor distribution.

$$\frac{\partial^2}{\partial z^2} U(z) = \frac{e}{\epsilon_0 \epsilon_r} \rho(z) \quad (3.3)$$

The charge present in the wells is distributed over the $k=0$ wave functions assuming parabolic bands with effective masses given by $m_0/(\gamma_1+\gamma_2)$ and $m_0/(\gamma_1-\gamma_2)$ for heavy and light bound bands, respectively, where m_0 is the electron rest mass. The doping is assumed to be distributed over two δ -layers on the left- and right-hand sides of the structure, in such a way that no net voltage drop is present over the structure. In practice this means that the doping is almost equally distributed. A weighted average of the new and old potentials is then used to calculate the next iteration. This procedure is iterated until the potential is stable within a pre-defined limit (10^{-5}). The final potential is then used for the calculation of all hole levels at finite k from Eq. (3.1).

For highly degenerate systems the parabolic approximation for charge distribution over the $k=0$ wave functions, implicitly assuming that the wave functions are independent of k , will induce an error in $\rho(z)$, but this effect was checked to be small.

The lowest hole levels (H0,1; L0,1) calculated exactly were within 0.5 meV of those calculated in the parabolic approximation of $\rho(z)$, for densities up to $1.5 \times 10^{16} \text{ m}^{-2}$. Because of the enormous difference in computational effort, we will use the latter method.

3.3 Numerical results

There are three relevant dimensions in any ADQW (the width of both wells and their separating barrier) which determine the effects of charging on the energy levels and on the SDHD. In the first place the lowest hole states need to be well bound for all reasonable densities, yielding a minimum well-width of about 30 Å. Secondly, the lowest $k=0$ solutions are to be mainly localized in one of the wells, but need to have amplitude in both wells. This means that the width of the central barrier should be of the order of a few times the penetration length of the heavy hole wave function ($\approx 25\text{-}60$ Å). Furthermore, one wants to avoid the complexity and ambiguity of many, hardly separated, bound states, occurring in wide wells (>100 Å). Within these limits, every ADQW behaves qualitatively the same, which allows us to consider one typical structure as general. The structure under consideration in this paragraph consists of a 59.4 Å (21 monolayers GaAs) and a 42.4 Å (15 ML) well, separated by a 33.9 Å (12 ML) barrier, with an Al content of 25%. In order to enhance the confinement of the bound states, the outer barriers have an Al content of 40%. The spacer layer between the doping and the nearest GaAs/AlGaAs interface is taken 33.9 Å. The thickness of the confining barriers is chosen such that no significant change of observables occurs upon a further increase.

3.3.1 Zero in-plane wavevector

In Fig. 3.1 the wave functions of the first two light and heavy-hole levels are depicted, together with the first two electron levels, for a sheet density of $1.5 \times 10^{16} \text{ m}^{-2}$. As can be expected, the groundstates of the heavy, light and electron levels are predominantly localized in the wide well and have an even character with respect to the middle of the central barrier, whereas the first excited states are odd-character functions, localized mainly in the narrow well.

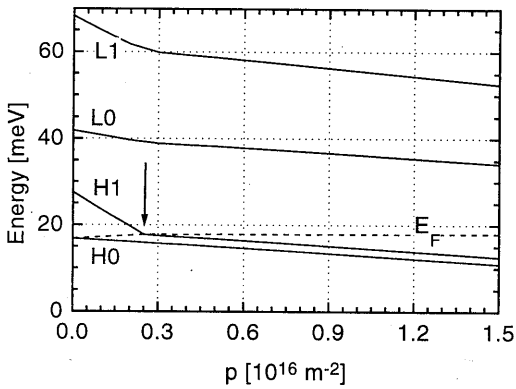


Fig. 3.2 Energies of L1, L0, H1 and H0 levels and Fermi energy as a function of doping concentration for the standard structure (see Fig. 3.1).

More remarkable is the density dependence of the energy separation between the first and second heavy-hole levels (H0 and H1), see Fig. 3.2. Upon the first introduction of charge, the H1 level rapidly shifts down to a few meV above the H0 level at $p \approx 0.2 \cdot 10^{16} \text{ m}^{-2}$. For higher sheet concentrations the H0-H1 separation remains independent of charge density. This behavior is a direct consequence of the electrostatic effect of the space charge.

For very low carrier concentrations, all charge will condense in the lowest level, H0. Since H0 is mainly localized in the wide well, the narrow well will be shifted down with respect to the wide well by the resulting electrostatic potential. Consequently, the H1 level, having its maximum amplitude in the narrow well, shifts down towards the H0 level. Fig. 3.1 illustrates this. A crossing of the H0 and H1 levels is avoided by the fact that the density of states (DOS) is almost the same for both levels: as soon as H1 drops below the Fermi level, all extra charge is equally distributed over both wells, resulting in a status-quo for the relative positions of H0 and H1. This point is indicated by the arrow in Fig. 3.2.

The density at which the H0 and H1 levels would become degenerate can be obtained by a simple back-of-the-envelope calculation of the electrostatic potential of a single charged plate, $V = ped/2\epsilon_0\epsilon_r$. Taking d as the distance between the centers of both wells and V the potential difference between H0 and H1 in the $p=0$ situation, we find $p = 0.16 \cdot 10^{16} \text{ m}^{-2}$, in reasonable agreement with the exact result. It is worthwhile to note that the above described alignment effect is not restricted to hole gasses, nor to the specific dimensioning of the ADQW.

3.3.2 Non-zero in-plane wavevector

The effect of self-consistency on the dispersion relations of an ADQW is depicted in Fig. 3.3. Clearly visible is the downward shift of the first excited heavy and light hole bands in the degenerate system [Fig. 3.3(b)], compared to the empty system [Fig. 3.3(a)],

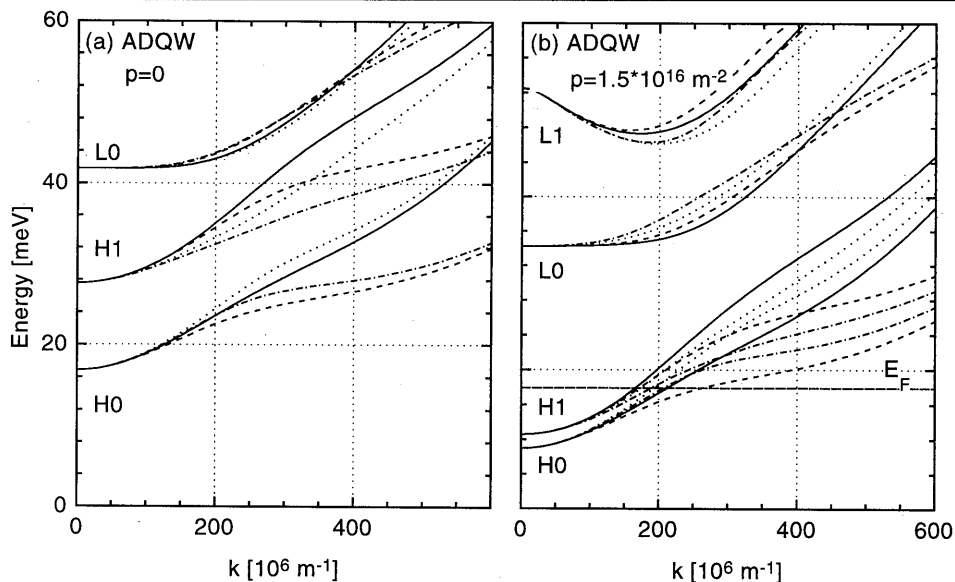


Fig. 3.3 (a) Dispersion relation of an empty 59.4-33.9-42.4 Å ADQW. (b) as (a), for a density of $1.5 \cdot 10^{16} \text{ m}^{-2}$. Solid lines, 'spin' up, $\langle 10 \rangle$ direction; dotted lines, 'spin' down, $\langle 10 \rangle$; dashed lines, 'spin' up, $\langle 11 \rangle$; dash-dotted lines, 'spin' down, $\langle 11 \rangle$.

due to the charge-induced bandbending. Note also the very similar dispersion curves for H0 and H1, implying the equality of their DOS. The spin-dependent hole delocalization for the empty and filled structures is represented in Fig. 3.4. Plotted is the expectation value of the z -operator, $\langle z \rangle = \int G^* z G dz$ with G the corresponding envelope function, for both spin directions of H0, L0 and H1 versus $|k|$ in the $\langle 10 \rangle$ direction. The zero of the z -axis is chosen at the left δ -doping layer. Note that the presence of charge does not affect $\langle z \rangle$ for H0 and H1 at $k=0$, but does so for the L0. This is a result of the smaller penetration length of the heavy-bound states, effectively localizing H0 and H1 almost completely in the separate wells, thus making $\langle z \rangle$ independent of their relative energy positions. The results for the empty ADQW confirm the observation by Goldoni and Fasolino⁶ that the H0 state, in contrast to the H1 and L0 states, does not show any appreciable spin dependent tunneling, i.e. the 'spin' up and 'spin' down states are not macroscopically separated. However, the spatial separation of 'spin' up and down states at $k \neq 0$ is clearly enhanced for the filled system, resulting in almost equal splittings for H0 and H1.

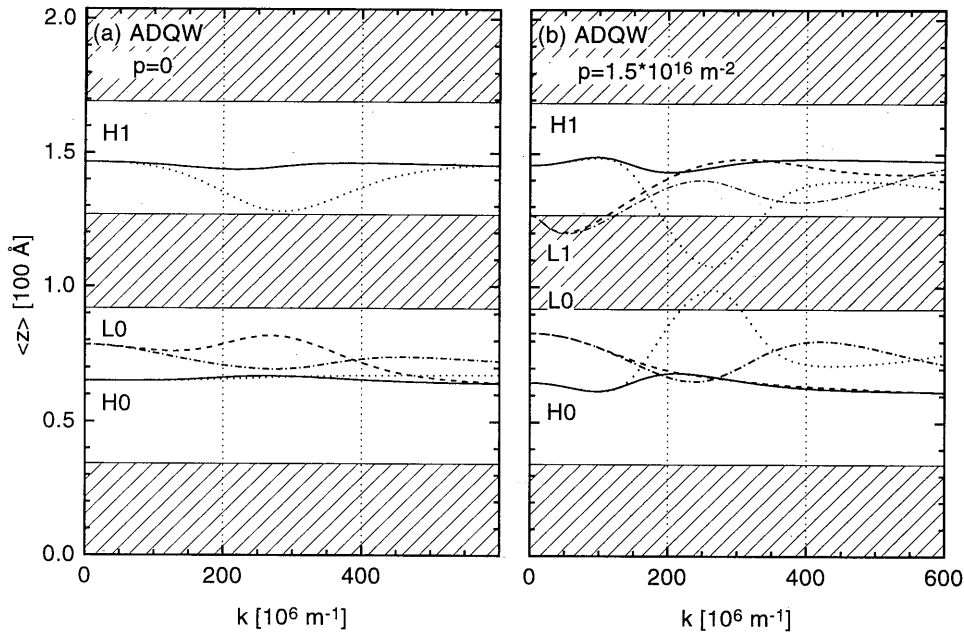


Fig. 3.4 (a) $\langle z \rangle$ versus $|k|$ for the ADQW of Fig. 3.3(a) in the $\langle 10 \rangle$ direction. (b) Idem, for Fig. 3.3(b) Solid lines, heavy, 'spin' up; dotted lines, heavy, 'spin' down; dashed lines, light, 'spin' up; dash-dotted lines, light, 'spin' down. The shaded areas indicate the AlGaAs barriers.

In Fig. 3.5 the light and heavy components of the envelope functions are shown at maximum spin splitting ($k=2.6 \cdot 10^8 \text{ m}^{-1}$). Only the components that are shifted towards the barrier obtain significant amplitude in the opposite well and will therefore 'feel' the potential-asymmetry, and become delocalized. Quite remarkable is the change of parity of the H0 and H1 wave functions with respect to the $k=0$ case: H0 has one node and H1 none. This is due to the fact that the H0 and H1 have already anticrossed at the present wavenumber [Fig. 3.3(b)], resulting in an exchange of the number of nodes.

The spin-dependent hole delocalization of the filled ADQW is augmented with respect to the empty system by two effects: first, by the extra asymmetry resulting from the bandbending and second, and most important, by the stronger mixing between the H0 and H1 bands at finite k , due to their small energy separation. To strengthen our argument about the general character of the SDHD enhancement, and to prove that this enhancement is mainly due to an increase of the coupling between H0 and H1 levels, we calculated $\langle z \rangle(k)$ traces for different densities. The results are depicted in Fig. 3.6. The main graph shows $\langle z \rangle(k)$ traces for an empty well, for $p=0.20 \cdot 10^{16} \text{ m}^{-2}$ (just before H1 becomes populated) and for $p=0.30 \cdot 10^{16} \text{ m}^{-2}$ (just after H1 is populated). Note the

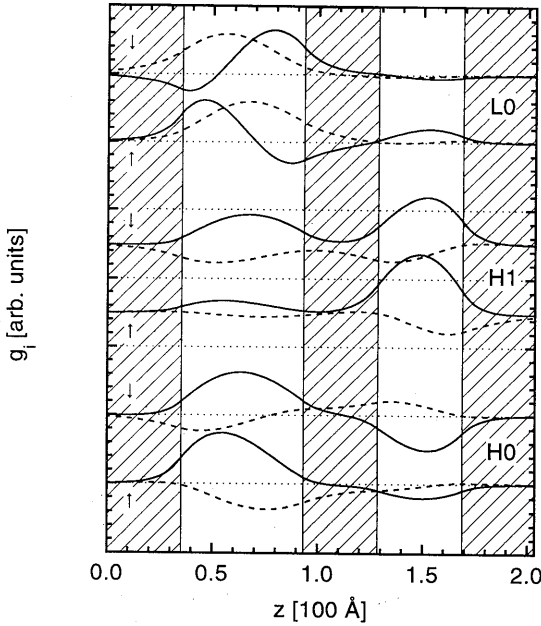


Fig. 3.5 Envelope function of wave function components at $k_{\parallel} = 2.6 \cdot 10^8 \text{ m}^{-1}$ in the $\langle 10 \rangle$ direction for the 59.4-33.9-42.4 Å ADQW with a density of $1.5 \cdot 10^{16} \text{ m}^{-2}$. Solid lines, heavy component; dashed lines, light component.

H0 and H1 states due to their decreased separation in energy, are inherent to any ADQW, as was shown in 3.3.1. However, the exact behavior of any structure is a function of its particular dispersion relation and wave functions, and is therefore dependent on sample dimensions.

Two more notes have to be made on the enhancement of spin-dependent hole delocalization by charging effects. First, the SDHD is, for both systems, induced by different couplings with other hole levels for 'spin' up and down states at *nonzero* wavevector⁶ and does not require resonance of levels. Second, the H0-H1 hybridization is not a result of a direct coupling, since (3.1) does not contain direct coupling terms between states with the same $|m_j|$. Consequently, the H0-H1 mixing must take place through interaction with light hole bands. It must be stated that the SDHD of the H0 and H1 wave functions can not arise from a direct hybridization with L0 and L1 wave functions, respectively, since this would result in a shift away from the central barrier at $k = 2.6 \cdot 10^8 \text{ m}^{-1}$ [Fig. 3.4(b)].

strong increase of spin-splitting of the H0 state at the density the H1 band becomes populated. This is also visible in the insert, where the maximum 'macroscopic' splitting ($|\langle z \rangle_{\text{up}} - \langle z \rangle_{\text{down}}|$) between 'spin' up and down branches is shown for both H0 and H1. It is important to note the stability of the spin splitting for densities above $p = 0.30 \cdot 10^{12} \text{ cm}^{-2}$, showing the relative unimportance of the increasing asymmetry of the structure.

Again, it should be stressed that the enhancement of the SDHD by charging effects is not restricted to the particular structure discussed above. The reason is that both responsible mechanisms, increasing asymmetry due to band bending and stronger mixing of

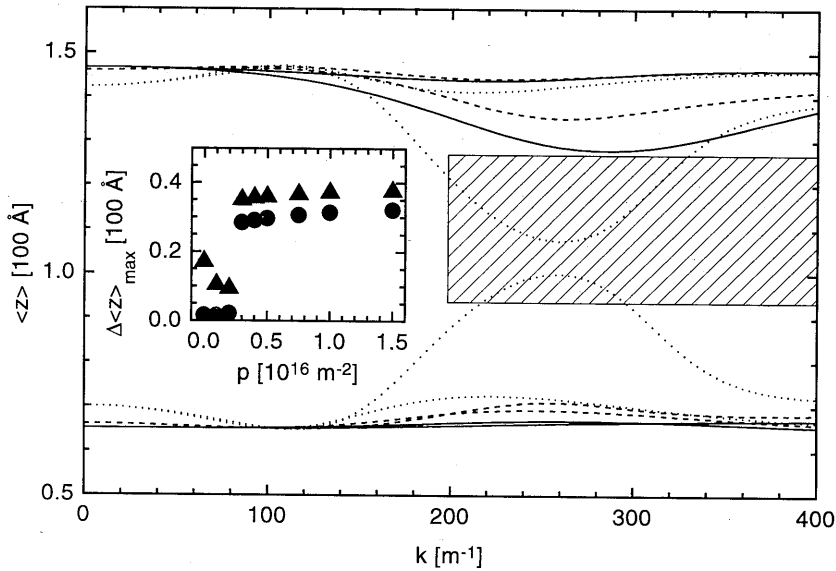


Fig. 3.6 $\langle z \rangle$ versus k for the 59.4-33.9-42.4 Å ADQW for $p=0$ (solid lines), $p=0.20 \times 10^{16} \text{ m}^{-2}$ (dashed) and $p=0.30 \times 10^{16} \text{ m}^{-2}$ (dotted). The shaded area indicates the central AlGaAs barrier. Insert: maximum macroscopic spin-splitting versus density. Circles, H0; triangles, H1.

The importance of well-bound light hole states for the enhancement of SDHD is illustrated in Fig. 3.7 where the maximum spin-splitting of H0 and H1 is depicted as a function of Al concentration in the confining barriers. The Al content of the central barrier is kept at 25%. Increasing this barrier only reduces the SDHD, since it weakens the coupling between the two wells. The SDHD is strongly enhanced when the Al concentration in the confining barriers is more than 30%. This coincides with a significant increase of the localization of the lowest light hole states (right y-axis), whereas the localization of the lowest heavy hole states is not significantly modified for $x > 20\%$. Both the maximum spin splitting and the confinement of the light hole states, as deduced from the flattening of the light hole energy curves, become saturated for $x > 50\%$. It is interesting to note that, although the maximum spin splitting is strongly modified by the Al concentration x , the wavenumber at which this occurs does not significantly shift with x .

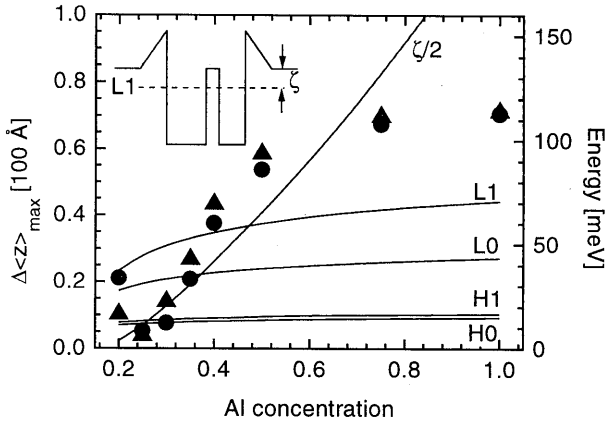


Fig. 3.7 Left axis: Maximum macroscopic spin-splitting versus Al concentration in the confining barriers of the standard structure. Circles, H0; Triangles, H1. Right axis: energies of the lowest light and heavy states, together with the L1 'effective binding energy' ζ .

So far, it has been shown that the spin dependent delocalization of hole levels is strongly dependent on the interactions between heavy and light hole bands. Due to the warped nature of the valence bands, also a direction dependence of SDHD is to be expected. Since the extrema in the dispersion surface due to warping occur along the $\langle 10 \rangle$ and $\langle 11 \rangle$ directions, we also calculated $\langle z \rangle$ in these directions, see Fig. 3.8. The spin dependent delocalization is clearly the most pronounced in the $\langle 10 \rangle$ direction, which confirms our argument that the spatial separation of heavy hole 'spin' up and down states arises from interactions with light hole bands. The dispersion relations of H0 and H1 in both directions are rather similar [Fig. 3.3(b)] but the $\langle 11 \rangle$ direction shows far less anticrossing behavior between heavy and light holes than the $\langle 10 \rangle$ direction. This results from a weaker interaction between light and heavy bands in the $\langle 11 \rangle$ direction.

3.4 Experimental results

In order to check our calculations, the sample described in paragraph 3.3 was grown, using 25% Al barriers. The doping concentration was chosen such that the Fermi-vector would lay approximately at maximum spin splitting, i.e. $k_f = 2.3 \cdot 10^8 \text{ m}^{-1}$ [Fig. 4(b)]. The aimed sheet density was $1.5 \cdot 10^{16} \text{ m}^{-2}$.

3.4.1 Transport experiments

The 'alignment'-effect described in paragraph 3.3.1 is confirmed by Shubnikov-de

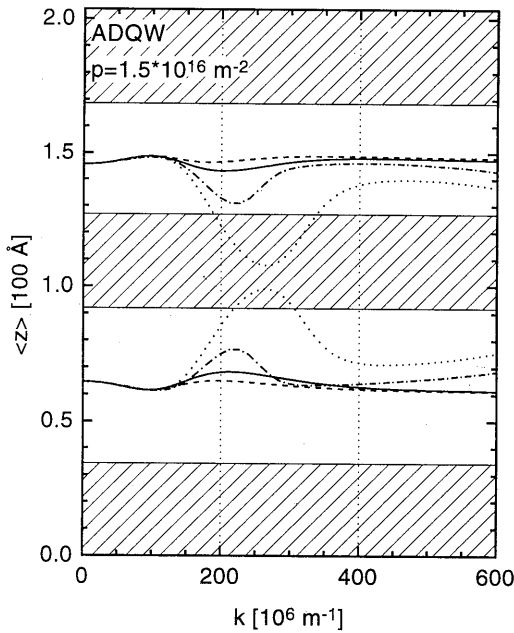


Fig. 3.8 $\langle z \rangle$ versus $|k|$ for the ADQW of Fig. 3.3(b) in the $\langle 10 \rangle$ and $\langle 11 \rangle$ directions. Solid lines, 'spin' up, $\langle 10 \rangle$; dotted lines, 'spin' down, $\langle 10 \rangle$; dashed lines 'spin' up, $\langle 11 \rangle$; dash-dotted lines, 'spin' down, $\langle 11 \rangle$.

Haas measurements on the aforementioned structure, see Fig. 3.9. A plot of $1/B$ versus extremum-number (see insert) revealed 3 distinct periodicities, with slopes related as 1:2:4. This is interpreted as follows: In the high field limit the Landau levels are non-degenerate, so each ρ_{xx} minimum corresponds to a filling-factor change of unity. In other words, Landau levels pass through the Fermi level one-by-one. Therefore the low- and intermediate-field regimes must correspond to the situations where four and two Landau levels pass through the Fermi level at the same time, respectively, and the filling factor changes in steps of four and two at each ρ_{xx} minimum. The values and positions of the Hall

plateaux give further evidence for this view. From both Shubnikov-de Haas and Hall measurements we found a sheet density of $1.5 \cdot 10^{16} \text{ m}^{-2}$. From Fig. 3.2 it becomes clear that a Landau level broadening of about one meV, which is quite reasonable, will prevent the H0 and H1 Landau levels from being resolved in the low field regime. Since spin up and down states are also degenerate at low fields, Landau levels will appear four-fold degenerate. Upon increasing the magnetic field, both the H0-H1 'degeneracy' and the spin degeneracy are lifted. Since this will most likely occur at different field strengths the described Shubnikov-de Haas behavior will result.

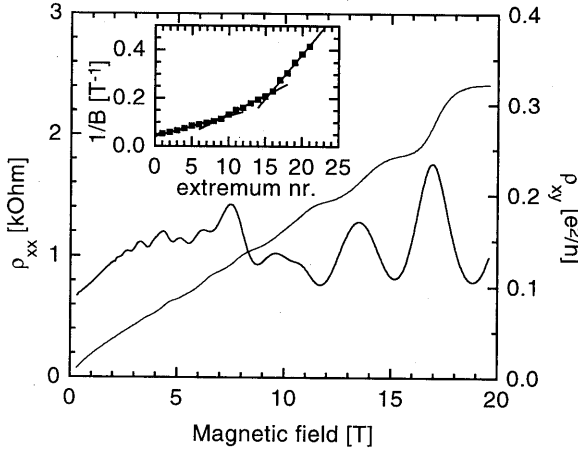


Fig. 3.9 Shubnikov-de Haas and Hall measurement on the standard ADQW with a carrier density of $1.5 \cdot 10^{16} \text{ m}^{-2}$. Insert: $1/B$ of the ρ_{xx} minima versus order-number (not filling factor) of the minima. Note the three distinct periodicities, related as 1:2:4.

light from a Ti:sapphire laser.

When we only take direct optical transitions into account, the PLE intensity is proportional to the product of the square of the matrix element and the joint density of states, integrated over the full k -space:

$$I(E) = \int d\mathbf{k}_{\parallel} M(\mathbf{k}_{\parallel})^2 \delta(E_t(\mathbf{k}_{\parallel}) - E) = \oint_E d\mathbf{k}_{\parallel} \frac{M(\mathbf{k}_{\parallel})^2}{\nabla E_t(\mathbf{k}_{\parallel})} \quad (3.4)$$

where the matrix element M is given by

$$\begin{aligned} M(\mathbf{k}_{\parallel}) &= \langle \Psi_e | p \cdot \epsilon | \Psi_h \rangle & \text{if } E_h > E_F \\ M(\mathbf{k}_{\parallel}) &= 0 & \text{if } E_h \leq E_F \end{aligned} \quad (3.5)$$

Here $E_t = E_h + E_e + E_g$, with E_h (E_e) the energy of the involved hole (electron) level, with respect to the top (bottom) of the valence (conduction) band, E_g is the bandgap of GaAs and E_F the Fermi energy. Ψ_h and Ψ_e are the total hole and electron wavefunctions, respectively, including the cell-periodic functions u_i . The Fermi energy was obtained by integration over the calculated dispersion surface. The Moss-Burstein shift (at $T=0$) is accounted for by $M(\mathbf{k})$, i.e. only empty states contribute to the PLE spectrum.

3.4.2 Optical experiments

The necessity of solving the Poisson and Schrödinger equations simultaneously for these samples is shown by the simulation of photoluminescence excitation (PLE) spectra. The top-panel of Fig. 3.10 displays an experimental spectrum of the same structure as the one on which the SdH measurements were performed, accompanied by the PL lines. The PL and PLE experiments were performed at 4.2 K, using normally incident, unpolarized

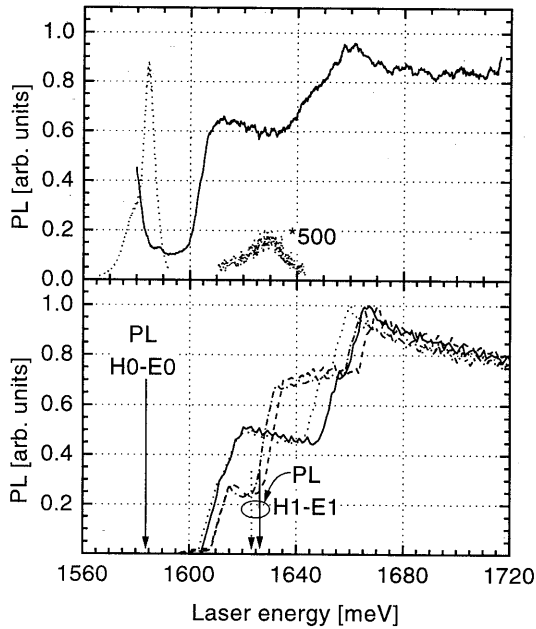


Fig. 3.10 Top panel: Experimental PL (dotted lines) and PLE (solid lines) spectra at 4.2 K. Bottom panel: calculated PLE spectra. The arrows denote the calculated PL onsets. Solid line: self-consistent, wave-function-continuity interface conditions; dotted line, idem, flux-conserving IC's; dashed lines, not-self-consistent, wave function-continuity IC's; dash-dotted line, idem, flux-conserving IC's.

non-self-consistent simulations deviate significantly from the experimental curve. The choice of interface conditions seems a rather arbitrary one for these calculations and it would be unwise to draw any conclusions from the minor deviations present. We will focus on the 'flux conserving' simulation in our last remark concerning Fig. 3.10.

A more detailed comparison of self-consistent and non-self-consistent calculated traces shows the need of calculating the exact matrix elements in order to obtain the correct intensities in the PLE spectrum. E.g., for both calculations the onsets of the first PLE step (E0-H0 at ~ 1.59 eV) and of the second step (E1-H1 at ~ 1.63 eV) lay on approximately the right energy positions, when the Moss-Burstein shift is properly taken into account. The significant differences between both calculations around these points arise mainly as a result of different matrix elements since the DOS of each band is almost independent of the inclusion of the effects of the charge distribution.

The dispersion relations and matrix elements were calculated for both interface conditions (flux- or wave function-continuity) in either a self-consistent or a non-self-consistent calculation, yielding four different sets of $M(\mathbf{k})$ and $E_i(\mathbf{k})$. The resulting $I(E)$ are depicted in the lower panel of Fig. 3.10. The only fitting parameter is a rigid shift in the bandgap, commonly encountered in doped systems and known as bandgap renormalization, which is used to position the first PL-peak, indicated by the arrow. The applied values are around 7 meV for the 'flux-conserving' calculations and around 11.5 meV for the 'continuous-wave function' calculations, which seems reasonable²⁶. Clearly visible in Fig. 3.10, there is excellent agreement between the experimental curve and the self-consistent simulations, whereas the

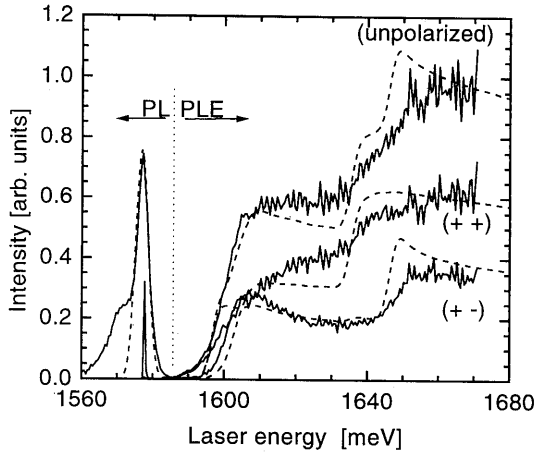


Fig. 3.11 *PL(E) spectra at 4.2 K of the same sample as Fig. 3.10, using normal incident, circular polarized light in both excitation and detection. Solid lines, experiment; dashed lines, calculation using flux-conserving IC's, after convolution with a 3 meV Gaussian.*

By using normal incident circular polarized light in excitation and detection, it is possible to separate the heavy and light hole contributions to the total absorption spectrum²⁷. Fig. 3.11 shows the experimental traces in cross polarization (+-), reflecting the light hole contributions, and in parallel polarization (++) , reflecting the heavy hole contributions. By incorporating the appropriate selection rules in (3.5), numerical simulations of these experimental spectra can be obtained. The dashed lines in 3.11 show the result of such a calculation, using flux conserving IC's. The numerical curves are convoluted with a 3 meV Gaussian to account for inhomogeneous spectral broadening and to reduce the numerical discretization noise. Again, the correspondence with the experimental traces is excellent. The same holds for the calculation with the other interface condition. In either case, the agreement with the experiment shows that also light and heavy hole components are calculated correctly within our model, which is, as we have shown, crucial for a proper calculation of the spin-dependent hole delocalization.

3.5 Summary

We have presented an exact and self-consistent method for solving the coupled Poisson equation and the 4*4 Luttinger Hamiltonian, with inclusion of anisotropy. The need for the inclusion of Coulombic effects on an asymmetric double quantum well has been investigated and shown to be of great importance for a meaningful comparison with transport experiments, as well as with optical experiments. In the same structure, the spin-dependent hole delocalization becomes strongly enhanced by the self-consistency due to a decrease of the energy separation between the first and second heavy hole

subbands and an increase in the asymmetry of the confining potential. The importance of confined light hole states for the SDHD was shown by variation of the height of the confining barriers. Furthermore, the influence of the interface conditions on the dispersion relations and wave function was inspected and found to be of minor importance for the structures under consideration.

References

1. e.g. E. P. O'Reilly, *Semicond. Sci. Technol.* **4**, 121 (1989) and references therein.
2. M. Z. Tidrow, K. K. Choi, C. Y. Lee, W. H. Chang, F. J. Towner and J. S. Ahearn, *Appl. Phys. Lett.* **64**, 1268 (1994)
3. K. Bernhard, A. Zrenner, G. Bohm, G. Trankle, G. Weiman, *Solid State Electronics* **37**, 1307 (1994)
4. Y. Ohno, M. Tsuchiya, H. Sakaki, *Appl. Phys. Lett.* **62**, 1952 (1993)
5. O. E. Raichev and F. T. Vasko, *Phys. Rev. B* **51**, 7116 (1995)
6. G. Goldoni and A. Fasolino, *Phys. Rev. Lett.* **69**, 2567 (1992)
7. G. Goldoni and A. Fasolino, *Surface Science* **305**, 333 (1994)
8. P. Lefebvre, P. Bonnel, B. Gil and H. Mathieu, *Phys. Rev. B* **44**, 5635 (1991)
9. V. Pereyra, 'Codes for Boundary Value Problems in Ordinary Differential Equations' in: *Lecture Notes in Computer Science* **76** (1979), Eds. B. Childs, M. Scott, J. W. Daniel, E. Denman and P. Nelson.
10. T. Ando, *J. Phys. Soc. Jpn.* **54**, 1528 (1985).
11. D. A. Broido and L. J. Sham, *Phys. Rev. B* **31**, 888 (1985).
12. U. Ekenberg and M. Altarelli, *Phys. Rev. B* **32**, 3712 (1985).
13. S.-R. Eric Yang, D. A. Broido and L. J. Sham, *Phys. Rev. B* **32**, 6630 (1985).
14. E. Bangert and G. Landwehr, *Surf. Sci.* **170**, 593, (1986)
15. For a general discussion of existing approaches see, e.g. R. Winkler and U. Rössler, *Phys. Rev B* **48**, 8918 (1993)
16. L. C. Andreani, A. Pasquarello and F. Bassani, *Phys. Rev. B* **36**, 5887 (1987).
17. G. Edwards, E. C. Valdares and F. W. Sheard, *Phys. Rev. B* **50**, 8493 (1994).
18. M. Kemerink, P. M. Koenraad, P. C. M. Christianen, R. van Schayk, J. C. Maan and J. H. Wolter, *Phys. Rev. B* **56**, 4853 (1997).
19. J. M. Luttinger, *Phys. Rev.* **102**, 1030 (1956).

20. G. Bastard, *Wave Mechanics Applied to Semiconductor Heterostructures*, Les Editions de Physique, Les Ulis, France (1988).
21. S. L. Chuang, *Phys. Rev. B* **40**, 10379 (1989)
22. It is still a point of discussion which interface conditions should be applied in the effective mass approximation. From a physical point of view, flux has to be conserved at any interface. However, to define the ratio of the wave function derivatives as the ratio of the effective masses, the Bloch basis functions need to be the same in GaAs and AlAs. Although this is a crucial assumption in the effective mass approximation, it is not fully true. See J. P. Cuypers and W. van Haeringen, *Phys. Rev. B* **47**, 10310 (1993)
23. For a review of problems and solutions concerning interface conditions in effective-mass theory see M. G. Burt, *J. Phys.: Cond. Matter* **4**, 6651 (1992)
24. G. Goldoni and A. Fasolino, *Phys. Rev. B* **51**, 9903 (1995)
25. *Physics of Group IV Elements and III-V Compounds*, ed. O. Madelung, M. Schultz and H. Weiss, Landolt-Börnstein Vols. 17a and 22a, Springer Verlag, Berlin (1987).
26. S. Haacke, R. Zimmermann, D. Bimberg, H. Kal, D. E. Mars, J. N. Miller, *Phys. Rev. B* **45**, 1736 (1992).
27. J. C. Maan, in *Physics and Applications of Quantum Wells and Superlattices*, Vol. 170 of *NATO Advanced Study Institute, Series B: Physics*, edited by E. E. Mendez and K. von Klitzing (Plenum, London, 1987)

4 The effect of strain on a second-order van Hove singularity in $\text{Al}_x\text{Ga}_{1-x}\text{As}/\text{In}_y\text{Ga}_{1-y}\text{As}$ quantum wells

(published in Phys. Rev. B 54, 10644 (1996))

4.1 Introduction

It is well known since the early 50's that analytic singularities in the frequency distribution $g(\nu)$ of crystal vibrations necessarily occur in infinite crystals due to the periodicity of the lattice¹. These so-called van Hove singularities occur whenever the condition $\nabla_{\mathbf{q}} v(\mathbf{q})=0$ is met, and can be categorized by the signs of the second derivatives of the dispersion function $v(\mathbf{q})$ to all coordinates \mathbf{q} and the dimensionality of the crystal¹. It was realized that the same applies for the joint density of states $J(E)$ in semiconductors, leading to singularities in the optical constants of both 2D and 3D bulk semiconductors². More recently, van Hove singularities have attracted attention in structures with artificial periodicity, such as transverse (normal) superlattices^{3,4,5}, lateral superlattices^{6,7} and bilayered systems⁸.

Since the lowest light hole state (L0) in $\text{GaAs}/\text{Al}_x\text{Ga}_{1-x}\text{As}$ quantum wells (QW's) has a negative effective mass for small in-plane wavenumbers, almost of the same magnitude as the electron mass, the joint density of states $J(E)$ can be expected to show

singular behavior around the L0-E0 transition. This singularity will be of a much stronger nature than the ordinary van Hove singularity, since this only requires the equality of the first derivatives, $\nabla_{\mathbf{k}}E_c(\mathbf{k})-\nabla_{\mathbf{k}}E_v(\mathbf{k})=0$. The equality of effective masses fulfills the much stronger condition $\Delta_{\mathbf{k}}E_c(\mathbf{k})-\Delta_{\mathbf{k}}E_v(\mathbf{k})=0$, with $E_c(\mathbf{k})$ and $E_v(\mathbf{k})$ the conduction and valance band dispersions, respectively, and Δ the Laplace operator. Although the negative L0 mass has been well established for a long time, both from theoretical⁹ and experimental¹⁰ studies, we are not aware of any experimental identification of this second-order van Hove singularity. Only recently Winkler¹¹ predicted a logarithmic van Hove singularity in the free electron-hole absorption spectrum of $\text{Al}_x\text{Ga}_{1-x}\text{As}/\text{GaAs}$ quantum wells.

In this chapter we will show clear experimental evidence for this second-order van Hove singularity in the Photo-Luminescence Excitation (PLE) spectrum of a highly degenerate, p-type, GaAs quantum well. The high doping concentration is necessary to suppress excitonic effects that dominate the singularity in empty systems¹¹. The doping has to be of p-type, instead of the more commonly used n-type, in order not to make the corresponding L0-E0 transitions forbidden due to k -space filling and momentum conservation. Furthermore, we will show how strain, resulting from the incorporation of indium in the well, increases the band parabolicity and isotropy and suppresses the van Hove singularity.

In paragraph 4.2 our experimental results will be presented and discussed. Results of both a numerical and an analytical analysis will be shown in paragraph 4.3. Paragraph 4.4 will summarize our conclusions.

4.2 Experiments

4.2.1 Sample description and experimental setup

In this study we will present results from two $\text{Al}_x\text{Ga}_{1-x}\text{As}/\text{In}_y\text{Ga}_{1-y}\text{As}$ quantum wells, with nominal indium concentrations of 0 and 10%. Both samples were grown by conventional MBE techniques on (100) oriented GaAs substrates and consisted of a single quantum well, separated by a thin bufferlayer from a short period superlattice. Both wells are nominally 95 Å wide, and symmetrically doped with Be δ -layers, which are separated from the well by 250 Å spacer layers. The GaAs well is confined by $\text{Al}_{0.45}\text{Ga}_{0.55}\text{As}$ barriers and grown at 690 °C. The $\text{In}_{0.10}\text{Ga}_{0.90}\text{As}$ well is confined by $\text{Al}_{0.25}\text{Ga}_{0.75}\text{As}$ barriers and grown at 500 °C to avoid indium diffusion. The indium

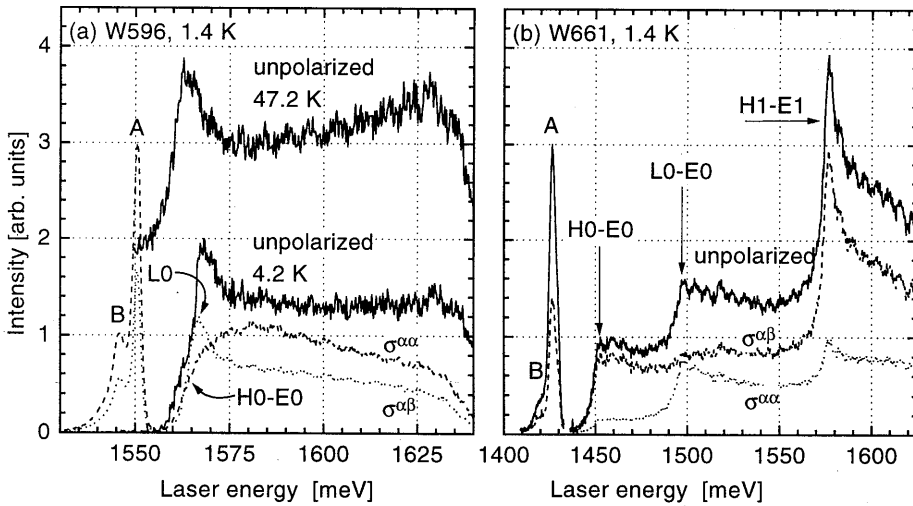


Fig. 4.1 (a) PL and PLE spectra of the GaAs QW. The dashed (dotted) lines indicate parallel (crossed) polarization. The solid lines indicate unpolarized measurements. Arrows indicate PLE onsets. The feature marked LO is identified as a second order van Hove singularity. (b) Same as (a) for the InGaAs QW. The arrows indicate the PLE onsets. Note the absence of a van Hove singularity in the LO-E0 transition. The peak marked H1-E1 is due to excitonic enhancement. All PLE spectra are normalized on the height of the first step in the unpolarized spectrum. The 47.2 K spectrum is offset by thermal background. The intensity drop above 1630 meV is due to laser fall-off.

concentration is confirmed by X-ray diffraction measurements. Both samples are capped by a 170 Å GaAs layer. The carrier densities, as obtained by transport measurements at 1.4 K, are $(9.0 \pm 0.1) \cdot 10^{15}$ and $(6.0 \pm 0.1) \cdot 10^{15} \text{ m}^{-2}$ for the GaAs and InGaAs sample, respectively. Transport mobilities for both samples are typically around $10 \text{ m}^2/\text{Vs}$.

The photoluminescence and -excitation (PL, PLE) spectra at 1.4 K were taken in a CryoVac ^4He bath cryostat in which magnetic fields up to 7 Tesla can be generated by means of a superconducting split-pair magnet. Measurements at 4.2 K and higher temperatures were performed in a CryoVac flow-cryostat. The samples were excited using normal incident light from a tunable Ti:sapphire laser, pumped by a 10 W argon laser. Typically, the output power of the Ti:sapphire laser was below 5 mW, with a spot size on the sample of approximately 3 mm^2 . In order to make sure that the optical spectra were not influenced by carrier heating effects, care was taken that no change in the spectra occurred upon a decrease of excitation power. The luminescence signal was focussed on the entrance slit of a Spex 0.75 m double monochromator and detected using

a cooled Hamamatsu photomultiplier connected to a Keithley dc electrometer. All experiments were performed in the Faraday configuration, using circular polarized light in excitation as well as in detection, unless stated otherwise.

4.2.2 Results

In Figs. 4.1(a) and (b) the PL and PLE spectra of both the GaAs and InGaAs quantum wells are depicted. The PL traces were taken using exciting light from the Ti:sapphire laser at 1598 meV. The traces denoted $\sigma^{\alpha\beta}$ and $\sigma^{\alpha\alpha}$ are polarization sensitive measurements, using circular (σ) polarized light. The indices α and β denote left or right oriented polarization, with $\alpha \neq \beta$. The first index denotes the polarization of the exciting light, the second of the detected polarization. The polarized light is used to separate light- and heavy-hole contributions to $PL(E)$ spectra, where the cross ($\sigma^{\alpha\beta}$) polarization is light hole sensitive, and the parallel ($\sigma^{\alpha\alpha}$) polarization is heavy hole sensitive¹². Due to the inversion symmetry of the quantum well potential, ‘spin’ up and down states are degenerate¹³, which implies the equivalence of $\sigma^{\alpha\beta}$ ($\sigma^{\alpha\alpha}$) and $\sigma^{\beta\alpha}$ ($\sigma^{\beta\beta}$).

We believe that the main luminescence line of both samples, marked A in Fig. 4.1 (GaAs: 1550.5±0.1 meV, InGaAs: 1426.8±0.2 meV), results from a nearly free H0-E0 transition. Both PL lines show a broadened shoulder, marked B (GaAs: 1546.5±0.2 meV, InGaAs: 1424±2 meV), on the low energy side. We will come back to the assignment of features A and B in the next part of this section. The luminescence intensity in the cross polarization is reduced by almost a factor of two with respect to the parallel polarization. This is a clear signature of the spin-memory effect¹⁴, commonly encountered in empty and n-type QW's. To our knowledge this effect has not been observed before in p-doped structures. The main luminescence lines of the GaAs and InGaAs samples have a Full-Width-Half-Maximum (FWHM) of 2.4 and 4.8 meV, respectively, showing the good quality of our samples.

The PLE traces in Fig. 4.1 show an apparent Moss-Burstein shift in the $\sigma^{\alpha\alpha}$ traces, corresponding to heavy hole transitions, reflecting the occupation of the H0 band. Going from GaAs to $\text{In}_y\text{Ga}_{1-y}\text{As}$ as well material, the total PLE spectrum can be seen to be redshifted by some 100 meV. This is the net result of the well-known redshift due to the smaller bandgap of InGaAs and the blueshift due to the compressive hydrostatic strain in the InGaAs structure. Furthermore, the energy gap between heavy- and light-hole ground states is enhanced in the $\text{In}_y\text{Ga}_{1-y}\text{As}$ QW with respect to the GaAs QW, due to the shear strain. We will discuss these points in more detail in paragraph 4.3 where numerical

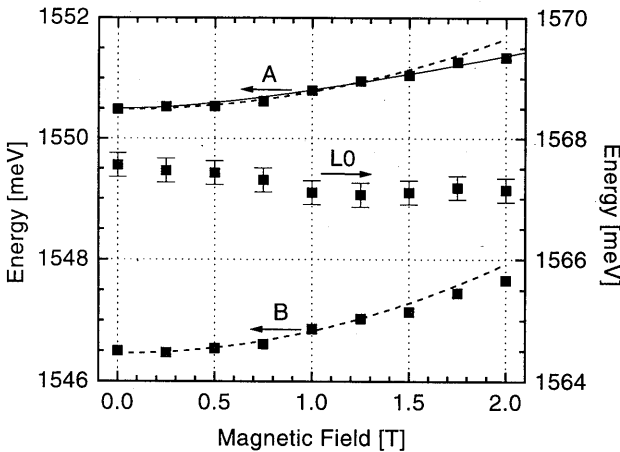


Fig. 4.2 Position of features A, B (left y-axis) and L0 (right y-axis) versus magnetic field for the GaAs QW. The dashed and dashed-dotted lines are fits with (4.1) in the range 0 to 1 T. The solid line is the result of a more sophisticated analysis along the lines of Ref.16, using an exciton binding energy of (0.8 ± 0.1) meV. Errorbars on A and B are of the size of the markers.

simulations will be presented. However, the most remarkable feature in Fig. 1(a) is the peak marked L0. We believe that this peak is the result of a second-order van Hove singularity, resulting from the negative L0 mass around $k=0$, and that it is not a result of excitonic effects. Since our interpretation strongly differs from the common interpretation of peaklike structures near the edge of an un-populated band, we will use paragraph 4.2.3 to argue why we do not attribute this peak to excitonic enhancement of transition probability.

More-over, in paragraph 4.3 we will demonstrate that this peak can be modelled without the inclusion of any coulombic interaction between holes and electrons.

4.2.3 Excitonic effects

On qualitative grounds it can be expected that the binding energy of the H0-E0 and L0-E0 excitons will be rather low in our structures and that free band-band transitions will dominate the optical spectra of these transitions. In the first place, both samples have a high 2D carrier concentration, which will screen the Coulomb interaction between the sea of (heavy) holes and the photo-generated electrons. Furthermore, phase-space filling and exchange interaction will block exciton formation in occupied subbands. The first argument will apply for all subbands, whereas the second is restricted to the occupied-ground state heavy holes. However, the overlap between the light and heavy hole ground states is very strong, resulting in an efficient screening of the L0-E0 exciton, see also chapter 5 of this thesis. These arguments can be illustrated by the PLE spectrum of the InGaAs QW, see Fig. 4.1(b). It is obvious that both the H0 and L0 to E0

transitions do not show significant excitonic enhancement of the PLE intensity, whereas the H1-E1 transition shows a clear excitonic peak at 1570 meV, which we will discuss in more detail below. Applying this reasoning to the GaAs sample leads to the conclusion that the large feature marked L0 cannot purely be of excitonic nature.

In order to quantify our arguments about the weakness of the exciton binding energy in our samples, we performed PL(E) measurements as a function of (perpendicular) magnetic field and temperature. In Fig. 4.2 the energetic positions of features A, B and L0 of the GaAs sample are depicted as a function of magnetic field. The energies of A and B are obtained from a phenomenological lineshape analysis, using a double Gaussian fit to the PL spectrum. It is known from QW bandstructure calculations for free carriers that, for low magnetic fields, the lowest H0 Landau level is linearly dependent on magnetic field, as is the lowest E0 Landau level¹⁵. In contrast to what is thus to be expected for a purely free H0-E0 transition, the main PL line (A) shows a prominent quadratic field dependence in the low field regime. This, of course, is the expected behavior of an exciton in a weak magnetic field. In a 2-dimensional system the exciton binding energy is given by¹⁶:

$$E(B) = \left[-4 + \frac{3}{8} \frac{\gamma^2}{4} \right] Ry^* , \quad \gamma = \frac{\hbar\omega_c}{2Ry^*} \quad (4.1)$$

where Ry^* is the effective Rydberg and ω_c the cyclotron frequency eB/μ^* , with $\mu^* = (1/m_e^* + 1/m_h^*)^{-1}$ the effective exciton mass. Fitting the energy of feature A with (4.1) in the range 0 to 1 T yields an exciton binding energy of (0.33 ± 0.04) meV, when we take $m_e^* = 0.067 \cdot m_0$ and $m_h^* = 0.4 \cdot m_0$ for the effective free electron and hole masses, respectively. As can be seen from the dashed line in Fig. 4.2, significant deviations arise at higher magnetic fields. Since (4.1) is only valid in the low-field regime ($\gamma < 1$) and $\gamma \approx 3$ at 1 T, the observed behavior can be more appropriately modeled with the Padé approximants of Ref. 16. These functions interpolate between the well-known analytic expressions for the exciton energy in low- and high-field regimes and are valid for all values of γ . The result of such an analysis is also shown in Fig 4.2 by the solid line. The used input parameters are the same as above. The best fit to the experimental data was obtained for an exciton binding energy of (0.8 ± 0.1) meV. This shows once more the relative unimportance of excitons at the H0-E0 transition in the GaAs sample under consideration. Note that this has to be compared to similar empty QW's where binding energies around 10 meV are found. It should here be pointed out that the excitonic oscillator strength is usually less affected by screening than the exciton binding energy¹⁷.

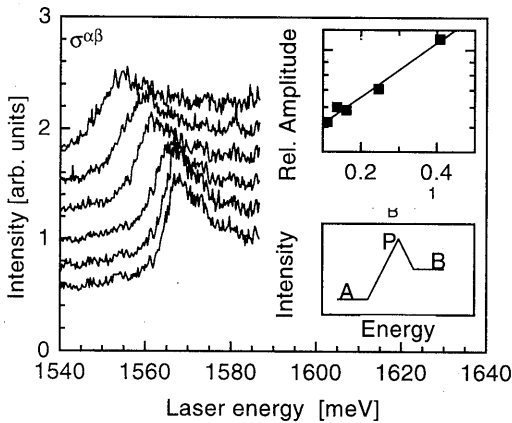


Fig. 4.3 Main graph: Temperature-dependent PLE spectra of the H1-E1 transition of the InGaAs sample. The spectra are offset for clarity and normalized on the height of the high-energy side plateau. Upper insert: Relative amplitude of the peak in the PLE spectra versus inverse thermal energy. The solid line is a linear fit corresponding to an activation energy of 2.5 meV. Lower insert: Schematic representation of the spectra in the main graph.

binding energy as above. However, from the lack of field dependence of the feature we can conclude that $1/m_e - 1/m_{L0} \approx 0$. This implies the equality of the electron and light-hole masses, what should be the case at a singularity in their joint density of states.

Convincing evidence for the irrelevance of excitonic effects to the L0 feature can be found in temperature dependent PLE measurements. If the L0 peak would be (partially) due to excitonic effects, a decrease in intensity would be expected when the thermal energy becomes of the same magnitude as the exciton binding energy, resulting from thermal dissociation of the exciton. In Fig. 4.1(a) the unpolarized PLE spectra are shown at 4.2 and 47.2 K. The spectra are normalized on the height of L0, measured from the low-energy foot of the peak to the top of the peak. The offset in the 47.2 K trace is due to the increased background of substrate luminescence. The observed broadening of some meV is in good agreement with the thermal energy $k_B T$, being 4.1 meV at 47.2 K. For higher temperatures the total PLE spectrum became unobservable, due to the increasing substrate luminescence background and, probably, due to the thermal opening of non-radiative recombination channels. As can be seen from the figure, no significant change in the relative amplitude of L0 occurs up to 50 K. This behavior can be the

From the energetic position and field dependence, we assign the PL shoulder B to a weak acceptor-bound exciton. Assuming a Be-bound exciton, application of Haynes' rule¹⁸ yields an estimated binding energy of 3 meV, in reasonable agreement with the observed values of 4 and 3 meV for GaAs and InGaAs, respectively.

The field dependence of the L0 feature in the GaAs PLE spectrum, also shown in Fig. 4.2, reflects the non-parabolic nature of the lowest light hole band¹⁵, since a L0 band that is characterized by a (positive) effective mass, would show a far stronger field dependence. As a result, it is impossible to estimate the exciton

explained in terms of a free band-band transition, of which the van Hove singularity is a special case, or in terms of a very strongly bound exciton, which would be the common interpretation¹⁹. The latter interpretation implies an exciton binding energy that exceeds the thermal energy by at least a factor 2, giving a lower bound of about 8 meV to the binding energy. The L0-E0 exciton binding energy, found experimentally in high-quality empty GaAs/AlGaAs wells of comparable width, is around 10 meV²⁰. It seems very unlikely to us that the binding energy in our highly degenerate sample would be almost the same as in an empty well, for reasons explained above. Therefore, we believe that the described (lack of) temperature dependence of the L0 feature strengthens our interpretation in terms of free band-band transitions.

To enlighten the contrast between the L0-feature and features of excitonic nature, the H1-E1 peak at 1570 meV in the InGaAs PLE spectrum was also studied as a function of temperature. The PLE spectra at temperatures ranging from 6.3 K up to 103.4 K are displayed in Fig. 4.3. The spectra are normalized on the height of the plateau on the high-energy side, marked B in the lower insert. Unlike the GaAs sample, the InGaAs sample showed no temperature dependent background, due to the larger separation in energy between substrate- and well-luminescence lines. As is obvious from the spectra, the relative amplitude of the peaked structure, marked P in the lower insert, is strongly decreasing with increasing temperature. This is made quantitative in the upper insert of Fig. 3, in which the relative amplitude, defined as $(P-B)/(B-A)$, of the H1-E1 peak is plotted logarithmically versus the inverse thermal energy. The solid line is a linear fit corresponding to an activation energy of 2.5 ± 0.1 meV. When we define the relative amplitude as $(P-A)/(B-A)$ we find a binding energy of 1.0 ± 0.1 meV. The first definition corresponds to the assumption that the excitonic peak is placed on top of the free band-band continuum, whereas the second reflects an excitonic structure that is placed in front of the continuum. Since the exciton binding energy is comparable to the spectral broadening, the correct value of the binding energy will be in between. Both results are in agreement with our interpretation of the structure in terms of excitonic enhancement of absorption intensity. The relatively low value of the obtained exciton binding energy is far below the H1-E1 binding energy in empty wells²¹, showing the importance of Coulomb screening for unoccupied subbands. However, the present result shows that the screening of the H1-E1 exciton by the free ground state heavy-holes is less efficient than the screening of the L0-E0 exciton. We relate this to differences in wavefunction overlap between H0, L0 and H1, which subject is discussed further in chapter 5. It is important to note that the L0 feature in the GaAs spectrum at 47.2 K shows an *increased* relative amplitude with respect to the 4.2 K trace, independent of the exact definition of relative

amplitude. Due to the temperature and energy dependent background, it is impossible to make this statement more quantitative.

4.3 Simulations

In the first two sub-paragraphs of this paragraph we will present the results of our numerical calculations on the bandstructure of the GaAs and $\text{In}_{0.10}\text{Ga}_{0.90}\text{As}$ quantum wells. Since our model has been described in detail in chapter 2 and in an earlier publication²², we will only give a brief outline of the model. In the last sub-paragraph an analytical expression for the second-order van Hove singularity will be presented and compared with both the numerical and the experimental results.

4.3.1 Numerical formalism

We calculated the light and heavy hole states, within the envelope function approximation, as exact eigenfunctions and eigenvalues of the full 4*4 Luttinger Hamiltonian²³. Standard flux-conserving interface conditions²⁴ were applied at the interfaces. The wavefunctions and the Coulomb potential were calculated self-consistently by iteration. The $\text{Al}_x\text{Ga}_{1-x}\text{As}$ bandgap is calculated using²⁵ $E_g(x)=1519.2+1360x+220x^2$ and we use the common 35:65 rule for the band-offset distribution. Strain and band-offsets for the GaAs/InGaAs system are incorporated according to the model-solid theory of Van de Walle²⁶ by addition of the appropriate terms on the diagonal of the Hamiltonian matrix. We used the formula of Goetz²⁷ *et al.* for the bandgap of $\text{In}_y\text{Ga}_{1-y}\text{As}$: $E_g(y)=1519.2-1583.7y+475y^2$. Electron energies and wavefunctions were calculated in the effective mass approximation, using linear interpolation between the effective electron masses in GaAs ($0.067\cdot m_0$) and InAs ($0.023\cdot m_0$).

The PLE simulations are obtained by defining a fine 2-dimensional mesh in k -space, with a typical grid size of $5\cdot 10^6 \text{ m}^{-1}$, and two 1-dimensional meshes in energy-space, $\sigma^{\alpha\alpha}(E)$ and $\sigma^{\alpha\beta}(E)$, reflecting the polarized PLE spectra, with an energy-step of 0.5 meV. On every k -meshpoint the optical matrix elements $M(\mathbf{k})$ of the H_i-E_j and $L_\Gamma-E_j$ ($i,j=0,1$) transitions are calculated¹⁵ and added to the appropriate element of one of the arrays $\sigma^{\alpha\alpha}(E)$ or $\sigma^{\alpha\beta}(E)$. Here, $E=E_g+E_{\text{hole}}(\mathbf{k})+E_{\text{el}}(\mathbf{k})$, with E_g the bandgap in the well and E_{hole} , E_{el} the hole and electron energies. As a result of this definition, only momentum-

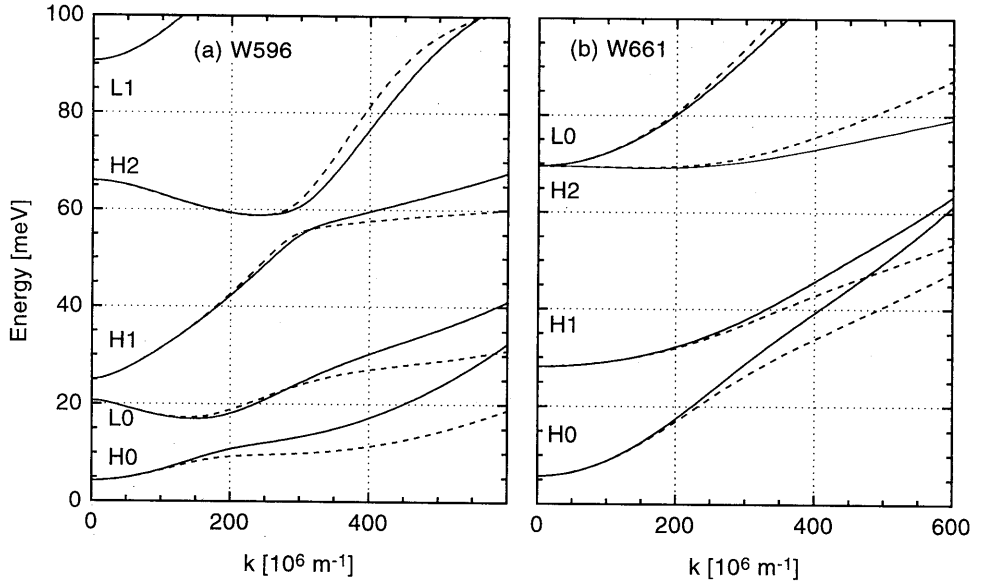


Fig. 4.4 Calculated dispersion relations of a 95 Å $\text{Al}_{0.45}\text{Ga}_{0.55}\text{As}/\text{GaAs}$ QW, filled with $9.0 \cdot 10^{15} \text{ m}^{-2}$ holes (a) and a 95 Å $\text{Al}_{0.25}\text{Ga}_{0.55}\text{As}/\text{In}_{0.11}\text{Ga}_{0.89}\text{As}$ QW, filled with $6.0 \cdot 10^{15} \text{ m}^{-2}$ holes (b). Solid (dashed) lines indicate the $\langle 10 \rangle$ ($\langle 11 \rangle$) direction. The InGaAs H2 level is just below L0 at $k=0$.

conserving transitions are taken into account. The Moss-Burstein shift, reflecting the H0 bandfilling, is accounted for by taking the optical matrix element equal to zero when $E_{\text{hole}}(\mathbf{k})$ is smaller than the Fermi energy. The calculated spectra are slightly smoothed to reduce discretization noise. The advantage of the PLE-spectrum calculation described above over the mathematically more elegant method of Ref. 21 is its insensitivity to singularities in the joint density of states. These were found to occur for the L0-E0 transition in the GaAs well. The obtained numerical resolution is beyond experimental resolution. Strictly spoken, the calculated spectrum is an absorption spectrum. However, the PLE spectrum is known to resemble the absorption spectrum closely, due to the efficient relaxation of photo-excited carriers to Γ point, where the radiative recombination takes place.

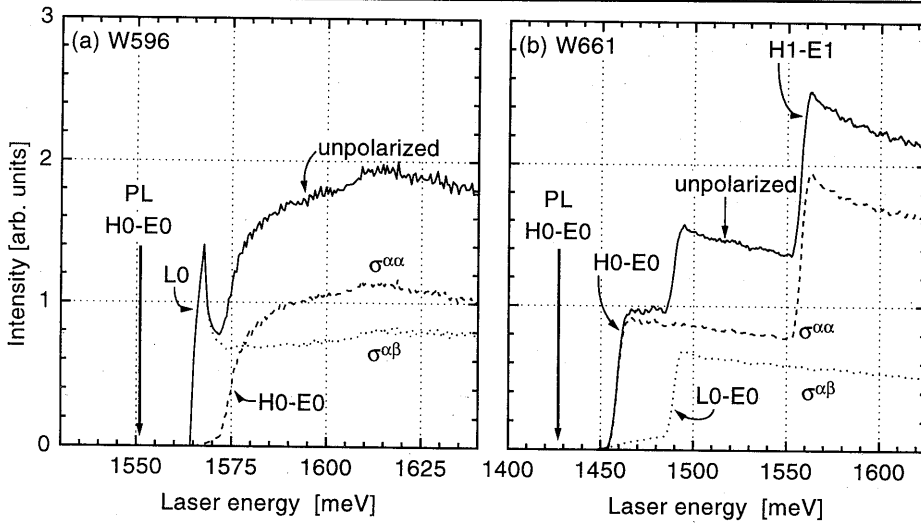


Fig. 4.5 Simulated PLE spectra of the GaAs (a) and InGaAs QW (b) of Fig. 4.4. Notation is the same as in Fig. 4.1. The fat arrows denote the position of the main PL line.

4.3.2 Numerical results and discussion

The calculated dispersion relations of the 95Å GaAs well, shown in Fig. 4.4(a), clearly exhibit the negative light hole ground state mass described earlier for small wavenumbers. A quantitative analyses revealed that the LO and E0 effective masses are nominally the same for k -vectors up to about $1 \cdot 10^8 \text{ m}^{-1}$, resulting in a second-order van Hove singularity in the joint density of states, as explained in the introduction. The extreme non-parabolicity of the light hole ground state is absent in the strained InGaAs QW [Fig. 4.4(b)] as a result of the weaker heavy-light hole interaction, which, in turn, is due to their increased separation. The InGaAs simulations are performed for an indium concentration of 11%, instead of 10%, although the latter was found in the X-ray diffraction measurements. This was chosen in order to lessen the difference between calculated and observed transition energies. For lower indium concentrations the energetic ordering of the H2 and LO bands is reversed, resulting in a sharp anticrossing near the zone center.

The PLE spectra corresponding to the dispersion curves in Fig. 4.4 are displayed in Fig. 4.5. It is obvious from a comparison with the experimental spectra in Fig. 4.1 that

our simulations account for all features present in the ground state transitions, including the second-order van Hove singularity at 1565 meV. This, again, confirms our claim that both heavy and light hole ground state transitions can be treated as free band-to-band transitions in the heavily doped samples under consideration. In contrast, the simulated H1-E1 transition in the InGaAs spectrum lacks the structure which is present in the experimental spectrum, and which thus must be attributed to excitonic effects.

It is worthwhile to note that not only the parabolicity of the valence bands is increased due to strain, but also the isotropy of the heavy-hole ground state, as can be deduced from the intersection of the H0 dispersion curves in the $\langle 10 \rangle$ and $\langle 11 \rangle$ directions with the Fermi-energy, see Fig. 4.4. This anisotropy is reflected by the steepness of the Moss-Burstein-shifted onset of H0-E0 transitions in the PLE spectra (the traces marked $\sigma^{\alpha\alpha}$ in Figs. 4.1 and 4.5) by the following mechanism. In general the photon energy of a k -conserving transition is given by $E(\mathbf{k})=E_g+E_{hole}(\mathbf{k})+E_{el}(\mathbf{k})$. Since the PLE onset is due to transitions at k -vectors on the Fermi contour, the Moss-Burstein-shifted H0-E0 onset energy becomes $E_B(\mathbf{k}_F)=E_g+E_F+E_{E0}(\mathbf{k}_F)$. Because the onset in the PLE spectrum reflects an average over all \mathbf{k}_F directions, the onset will only be sharp when E_B is the same in all directions of \mathbf{k}_F . This requires a constant magnitude of \mathbf{k}_F in all directions, since the conduction band is isotropic. This condition can only be fulfilled for an isotropic H0 band. In simulation as well as in experiment, the GaAs well displays a far more rounded H0-E0 onset than the InGaAs well, indicating the enhanced isotropy in the strained sample.

Another interesting feature in the $\sigma^{\alpha\beta}$ -PLE spectrum of the $\text{In}_y\text{Ga}_{1-y}\text{As}$ QW is the 'foot' below the L0-E0 onset at 1485 meV. This is a result of admixture of light-hole character in the heavy-hole ground state at non-zero wavenumber. This foot is also present in the experimental spectrum.

The spectra depicted in Fig. 4.5 are slightly red-shifted in order to obtain the correct PL energy, indicated by the arrows. This shift is commonly encountered in heavily doped systems and known as bandgap renormalization, and usually described in terms of exchange- and correlation effects. The applied values for the GaAs and InGaAs simulations are 14.5 and 11.0 meV, respectively.

It can be noted that the predicted Moss-Burstein shift overestimates the experimentally observed shift, for both the GaAs and $\text{In}_y\text{Ga}_{1-y}\text{As}$ QW's. A deviation of this kind was also observed in a similar simulation of a p-doped asymmetric double quantum well²¹. In Table 4.1 we have summarized the observed and predicted Moss-Burstein shifts. The Moss-Burstein shifts are calculated in two limiting situations, which will briefly be discussed in the following. The first calculation is based on full k -

conservation, as are the PLE simulations in Fig. 4.5. This method has yielded good results for similar n-type QW's²⁸. Assuming k -conservation, the observed deviations in the Moss-Burstein shift have to be caused by incorrectness of the calculated dispersion relations. This is unlikely since the over-all similarity of observed and calculated PLE spectra does not suggest significant errors in the calculated bandstructure. Moreover, the overestimation would have to result mainly from a severe incorrectness in the calculation of the very well understood electron band, since the difference between the H0 energies at $k=0$ and $k=k_F$ is less than the observed overestimation. The second calculation is based on full k -relaxation, in which case the Moss-Burstein shift equals $E_F - E_{H0}(k=0)$. The k -conservation selection rule could, e.g., be lifted by strong electron localization. Good results in the simulation of PL spectra of bulk semiconductors have been obtained by calculations based on this assumption²⁹. Since full k -relaxation strongly underestimates the Moss-Burstein shift, a partial relaxation is more likely. However, to account for the observed deviation of 10 meV, still a strong relaxation is required. As a consequence, PLE onsets and PL lines will become broadened on a similar energy scale. This is obviously not supported by the experiments. Other effects to explain the discrepancy between the calculated and observed Moss-Burstein shifts, such as non-parabolicity of the electron bands or thermal effects, are far too small to explain the deviation. Exciton effects can be ruled out since they only increase the separation between PL and PLE spectra.

It is interesting to note that a similar effect in the Moss-Burstein shift has been observed by Deppe *et al.*³⁰ in highly doped bulk $\text{In}_{0.53}\text{Ga}_{0.47}\text{As}$ layers. For p-type doping no appreciable Moss-Burstein shift was found, while in n-type layers a significant shift was observed. No explanation for this effect is given by the authors. To conclude the

sample	Calculation		Experiment
	k-cons. [meV]	k-relax. [meV]	[meV]
GaAs	25.4	5.9	14.0
InGaAs	32.9	10.9	21.5

Table 4.1 Calculated and observed Moss-Burstein shifts. The models used for the calculations are discussed in the text. The Moss-Burstein shifts are measured from the main PL-line to the half-height of the H0-E0 PLE onset, in the parallel polarization. The typical error is 1 meV.

considerations on the Moss-Burstein-shift, we are unable to find a sensible explication for the overestimation, but we believe that the observed deviation is caused by a non-trivial effect. A more systematic study is, however, required to resolve this problem.

4.3.3 Analytical results

In Ref. 2 analytical expressions are derived for the various types of Van Hove singularities under the usual condition of equality of the first derivatives of the electron and hole dispersions. Below we will derive an expression for an isotropic system, in which also the second derivatives of the valance and conduction band dispersion relations are equal. As we will mainly follow the lines of Ref. 2, only a brief outline of the derivation will be given.

We start from the well known expression for the joint density of states in a two dimensional system,

$$J(E) = \frac{2}{(2\pi)^2} \int dk_x dk_y \delta(E_c(k_x, k_y) - E_v(k_x, k_y) - E) \quad (4.2)$$

where the integral runs over the full Brillouin zone and E_c and E_v are conduction and valance band dispersion relations, respectively. Under the conditions mentioned above, we can, for an isotropic system, expand $E_c - E_v$ around the singular point at energy E_0 as

$$E_c(k_x, k_y) - E_v(k_x, k_y) = E_0 + \frac{\hbar^2 k^4}{2a} + O(k^6) \quad (4.3)$$

with $k = (k_x^2 + k_y^2)^{1/2}$. The cubic and higher odd-power contributions are zero since the dispersion relations are invariant under the transformation $\mathbf{k} \rightarrow -\mathbf{k}$ because of the inversion symmetry of the potential. Substitution in (4.2), transformation to polar coordinates and using the property of the delta function

$$\int_a^b dx g(x) \delta(f(x)) = \sum_{x_0} g(x_0) \left| \frac{df}{dx} \right|_{x=x_0}^{-1} \quad (f(x_0) = 0) \quad (4.4)$$

yields

$$\begin{aligned} J(E) &= A(E - E_0)^{-\frac{1}{2}} + B & \text{if } E > E_0 \\ J(E) &= B & \text{if } E < E_0 \end{aligned} \quad (4.5)$$

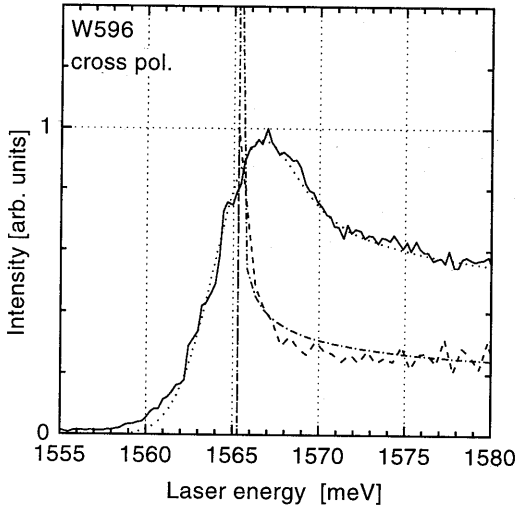


Fig. 4.6 Solid line: experimental PLE spectrum (normalized) of the GaAs QW in cross polarization. Dashed line: unsmoothed numerical PLE simulation (normalized). Dashed-dotted line: joint density of states $J(E)$ of L0-E0 transition, calculated from (4.5) with $E_0=1565.3$ meV and A and B used as adjustable parameters. Dotted line: *idem*, but convoluted with a 2.9 meV wide Gaussian profile and normalized.

interpretation.

4.4 Summary

In this chapter we have reported the first experimental identification of a second-order van Hove singularity in the photo-luminescence excitation spectrum of an $\text{Al}_x\text{Ga}_{1-x}\text{As}/\text{GaAs}$ quantum well. We have shown the relative unimportance of excitonic effects in the light and heavy hole ground states, in both samples. We believe this is due to the efficient screening of the unpopulated L0 state by the sea of free heavy holes. The observed spectra are in agreement with the theoretical predictions of Winkler¹¹ in the sense that a singularity is found in the free electron-hole absorption spectrum. Although Winkler identified this singularity as a logarithmic van Hove singularity, fulfilling the usual condition $\nabla_{\mathbf{k}}E_c(\mathbf{k})-\nabla_{\mathbf{k}}E_v(\mathbf{k})=0$, we have shown that it fulfills the far more restrictive condition $\Delta_{\mathbf{k}}E_c(\mathbf{k})-\Delta_{\mathbf{k}}E_v(\mathbf{k})=0$, which gives rise to a $1/\sqrt{x}$, with $x \rightarrow 0$, divergence. The

with $A=1/(4\pi)(\hbar^2/2a)^{-1/2}$ and B a constant that depends on the detailed bandstructure. As is apparent from (4.5) a $1/\sqrt{x}$, with $x \rightarrow 0$, divergence is to be expected at the onset of the L0-E0 transition in the PLE spectrum. In comparison, the usual Van Hove condition gives a quadratic term in (4.3) and only a step in $J(E)$ at E_0 ^{2,31}. In Fig. 4.6 $J(E)$, calculated from (4.5), is plotted, together with the numerically calculated PLE signal. Obviously there is excellent agreement between the numerical and analytical curves. Also shown are the experimental PLE signal in cross-polarization and $J(E)$, convoluted with a 2.9 meV wide Gaussian profile. Again, the similarity is striking, justifying our

derived analytical expression was found to be in excellent agreement with both the numerical and the experimental results.

It is interesting to note that Gravier *et al.*³² observed a similar structure in the cross-polarization PLE spectrum of a 80 Å p-type QW. These authors attribute this peak to excitonic effects. Although the carrier density in their sample is a factor three lower than in ours, we still feel that this feature can also be a second order van Hove singularity.

Furthermore, it was experimentally shown how the strain in an AlGaAs/InGaAs QW increases the band parabolicity, which translates into the elimination of the second-order van Hove singularity. From the steepness of the Moss-Burstein-shifted onsets of the H0-E0 transitions in PLE it was deduced that the severe warping of the heavy-hole ground state in the GaAs well is strongly reduced in the InGaAs well. Experimental results were found to be in good agreement with numerically obtained dispersion relations and PLE spectra. Although most numerical details were quantitatively covered by the experiments, the predicted Moss-Burstein-shift exceeded the observed shift significantly. No consistent interpretation of this effect was found.

References

1. L. Van Hove, Phys. Rev. **89**, 1189 (1953)
2. See, e.g. *Electronic States and Optical Transitions in Solids* by F. Bassani and G. Pastori Parravicini (Ed. R.A. Ballinger), Pergamon Press, Oxford (1975).
3. H. Chu and Y.-C. Chang, Phys.Rev.B **36**, 2946 (1987).
4. K. Fujiwara, K. Kawashima, T. Yamamoto, N. Sano, R. Cingolani, H. T. Grahn, and K. Ploog, Phys.Rev.B **49**, 1809 (1994).
5. H. A. Fertig and S. Das Sarma, Phys.Rev.B **42**, 1448 (1990).
6. R. W. Winkler, J. P. Kotthaus, and K. Ploog, Phys.Rev.Lett. **62**, 1177 (1989).
7. D. Weiss, K. von Klitzing, K. Ploog, and G. Weimann, Surf. Sci. **229**, 88 (1990)
8. L. Smrčka and T. Jungwirth, J.Phys.:Condens.Matter **7**, 3721 (1995).
9. See e.g. *Wave Mechanics applied to Semiconductor Heterostructures* by G. Bastard, (Halsted Press :Les Editions de Physique, Les Ulis, 1988) and references therein.
10. R. K. Hayden, D. K. Maude, L. Eaves, E. C. Valdares, M. Henini, F. W. Sheard, O. H. Hughes, J. C. Portal, and L. Cury, Phys.Rev.Lett. **66**, 1749 (1991).
11. R. Winkler, Phys.Rev.B **51**, 14395 (1995).
12. J. C. Maan in: *Physics and applications of quantum wells and superlattices*, ed. E. E. Mendez and K. von Klitzing, Nato-ASI series, Plenum, London 1987
13. L. C. Andreani, A. Pasquarello, and F. Bassani, Phys.Rev.B **36**, 5887 (1987).
14. M. Potemski, J. C. Maan, A. Fasolino, K. Ploog, and G. Weimann, Phys.Rev.Lett.**63**, 2409 (1989).
15. F. Ancillotto, A. Fasolino, and J. C. Maan, Phys.Rev.B **38**, 1788 (1988).
16. A. H. MacDonald and D. S. Ritchie, Phys.Rev.B **33**, 8336 (1986).
17. G. D. Sanders and Y.-C. Chang, Phys. Rev. B **35**, 7551 (1987).
18. *Doping in III-V Semiconductors* by E. F. Schubert, Cambridge University Press (1993).

19. See, e.g. C. Weisbuch and B. Vinter, *Quantum Semiconductor Structures* (chapter 3), Academic Press London (1991).
20. E. S. Koteles and J. Y. Chi, *Phys.Rev.B* **37** 6332 (1988).
21. G. D. Sanders and Y.-C. Chang, *Phys. Rev. B* **35**, 1300 (1987).
22. M. Kemerink, P. M. Koenraad, P. C. M. Christianen, A. K. Geim, J. C. Maan, J. H. Wolter, and M. Henini, *Phys. Rev. B* **53**, 10000 (1996).
23. J. M. Luttinger, *Phys.Rev.* **102**, 1030 (1956).
24. See, e.g. M. Altarelli in *Heterojunctions and Semiconductor Superlattices*, ed. G. Allan, G. Bastard, N. Boccara, and M. Voos, Springer Verlag, Berlin (1986).
25. M. Guzzi, J. L. Steahly in *Physics of DX Centers in III-V Ternary Compounds*, ed. J. C. Bourgoin, Trans Tech, Aedermannsdorf 1989.
26. C. G. Van de Walle, *Phys.Rev.B* **39**, 1871 (1989).
27. K. H. Goetz, D. Bimberg, H. Jürgensen, J. Solders, A. V. Solomonov, G. F. Glinskii, and M. Razeghi, *J.Appl.Phys.* **54**, 4543 (1983).
28. R. Cingolani, W. Stolz, and K. Ploog, *Phys.Rev.B* **40**, 2950 (1989).
29. J. De-Sheng, Y. Makita, K. Ploog, and H. J. Quesser, *J.Appl.Phys.* **53**, 999 (1982), B. G. Arnaudov, D. S. Domanevskii, A. M. Issusov, P. L. Gardev, and S. K. Evtimova, *Semicond.Sci.Technol.* **5**, 620 (1990).
30. D. G. Deppe, N. D. Gerard, C. J. Pinzone, R. D. Dupuis, E. F. Schubert, *Appl.Phys.Lett.* **56**, 315 (1990).
31. In fact, the usual Van Hove condition is fulfilled for almost all transitions at $k=0$, since it only requires equality of the first derivatives of hole and electron dispersions, which are usually zero at the Γ -point. However, the resulting effect on the joint density of states is a step of height $m^*/\pi\hbar^2$ ($m^{*-1}=m_e^{-1}+m_h^{-1}$), which is just the density of states of a parabolic band.
32. L. Gravier, M. Potemski, A. Fisher, and K. Ploog, *Solid-State Electron.* **40**, 697 (1996).

5 Magneto-optical study on exciton screening in p-type $\text{Al}_x\text{Ga}_{1-x}\text{As}/\text{In}_y\text{Ga}_{1-y}\text{As}$ quantum wells

(published in Phys. Rev. B **56**, 4853 (1997) and Phys. Stat. Sol. (a) **164**, 73 (1997))

5.1 Introduction

The unbinding or bleaching of excitons in semiconductor heterostructures has been subject of numerous investigations during the past decade. Theoretically, exciton unbinding by interaction with either a sea of a single type of free carriers^{1,4}, or photo-created carriers or excitons^{5,6} has been considered. Usually, a distinction is made between Coulomb screening and bleaching mechanisms that are related to the Pauli exclusion principle, i.e. phase-space filling and exchange. Qualitatively, Coulomb screening can be thought of as a rearrangement of free carriers in the presence of a disturbing electrostatic potential, e.g. of a photo-created electron or hole, which compensates the disturbing potential. Bleaching mechanisms that are due to the exclusion principle are based on the fermion character of electrons and holes: once a state is occupied by a particle, free or bound, it cannot be used to form an exciton. This mechanism is usually referred to as phase-space filling. Furthermore, the presence of other electrons or holes leads to a modification of the electron-hole interaction, which results in an enhancement

of the exciton radius and hence a reduction of its binding energy. This mechanism is generally referred to as exchange. It is important to note that Coulomb screening affects excitons of all subbands, whereas the other mechanisms are restricted to occupied subbands. A more extensive discussion of exciton bleaching mechanisms can be found in chapter 2, paragraph 5.

In experiments on exciton bleaching by photo-created free-carriers or excitons contradictory results have been obtained regarding the relative importance of Coulomb screening and effects related to the Pauli exclusion principle⁷⁻¹¹. Furthermore, the bleaching effectiveness of various states of the photo-generated carriers, i.e. hot or cold plasma or excitons, seems to be a source of disagreement between theory and experiment¹⁰⁻¹². The study of exciton bleaching by a single type of carriers circumvents the latter problem, whereas the former question concerning the relative importance of Coulomb screening and Pauli effects can be addressed by using p-type doping, since it allows to discriminate unambiguously between them, as will be shown below. Most authors dealing experimentally with exciton unbinding in doped systems have only studied these effects qualitatively¹³⁻¹⁶. In particular, peaks in optical absorption spectra are usually taken as an indication for the presence of excitons. This method can be misleading due to the presence of Van Hove singularities¹⁷, see also chapter 4, or due to carrier-induced broadening of absorption peaks¹⁸.

In this chapter, we will quantify the effects of a sea of free heavy holes on the exciton binding energy of various subbands in GaAs and InGaAs QWs. We will show that excitons of occupied subbands are fully unbound at hole densities in the range $(6-9) \cdot 10^{15} \text{ m}^{-2}$. Excitons of unoccupied subbands, in contrast, will be shown to have a finite binding energy at these densities. However, its value is far below what is found in an undoped well. Furthermore, it seems likely that, in p-doped wells, the excitons of excited subbands are less efficiently screened than those of the light-hole groundstate, due to the lesser overlap of the screening groundstate heavy-holes with the excited subbands than with the groundstate light holes.

The remainder of this chapter will be organized as follows. In paragraph 5.2 we will outline the model that was used to interpret the magneto-absorption spectra that are presented in paragraph 5.3. The data will be discussed in paragraph 5.4. Paragraph 5.5 will summarize our conclusions.

5.2 Theory

The total Hamiltonian describing the relative motion of an electron-hole pair in a confining electrostatic potential can in general be written as $H_{ex}=T_h+T_e+U_{e-h}+U_v+U_c$. The first two terms on the right hand side describe the kinetic energy of the hole and electron, respectively. The third term describes the screened Coulomb interaction and the last two terms describe the confining potentials of the valence- and conduction band, respectively. The corresponding eigenvalue problem has been solved by Bauer and Ando¹⁹ and Yang and Sham²⁰ for a quantum well potential in a perpendicular magnetic field. This is, however, an extremely laborious and far from trivial task. Therefore we simplify the problem by solving the hole and electron Hamiltonians, with inclusion of their respective electrostatic potentials $U_{v,c}$, separately, as a function of magnetic field, and correct for the exciton binding energy afterwards. A posteriori exciton corrections to free Landau-levels have already successfully been used in the high-field limit^{21,22}. The price paid for this simplification consists mainly of the fact that anti-crossings between excitonic states that are coupled by the Coulomb interaction cannot be reproduced. Despite this hiatus, the calculated exciton energies will be shown to match experimental data closely, except in the vicinity of apparent anti-crossings.

The hole Landau levels are calculated from the 4*4 Luttinger Hamiltonian on the basis $m_j = (3/2, -1/2, 1/2, -3/2)$. The magnetic field B is assumed to be parallel to the quantization axis z, i. e. perpendicular to the plane of the QW. Starting from the matrix expression for $B=0$ ^{23,24}, we follow the usual procedure²⁵ of replacing k_x and k_y by their operator expressions, written in terms of the standard raising and lowering operators. Making the eigenvector ansatz²⁵

$$G_N = \left(g_N^{h+}(z) \cdot u_{N-2}, g_N^{l-}(z) \cdot u_N, g_N^{l+}(z) \cdot u_{N-1}, g_N^{h-}(z) \cdot u_{N+1} \right) \quad (5.1)$$

where the u_N are the harmonic oscillator eigenfunctions, we arrive at the following Hamiltonian:

$$\frac{H_{ax} = \frac{\hbar^2}{m_0}}{\left[\begin{array}{cccc}
\frac{\gamma_1 + \gamma_2}{l_c^2} \frac{2N-3}{2} + \frac{\gamma_1 - 2\gamma_2}{2} k_z^2 & \frac{\sqrt{3}}{l_c^2} \gamma \sqrt{(N-1)N} & \frac{\sqrt{6}}{l_c} \gamma_3 \sqrt{N-1} k_z & 0 \\
\frac{\sqrt{3}}{l_c^2} \gamma \sqrt{(N-1)N} & \frac{\gamma_1 - \gamma_2}{l_c^2} \frac{2N+1}{2} + \frac{\gamma_1 + 2\gamma_2}{2} k_z^2 & 0 & \frac{\sqrt{6}}{l_c} \gamma_3 \sqrt{N+1} k_z \\
\frac{\sqrt{6}}{l_c} \gamma_3 \sqrt{N-1} k_z & 0 & \frac{\gamma_1 - \gamma_2}{l_c^2} \frac{2N-1}{2} + \frac{\gamma_1 + 2\gamma_2}{2} k_z^2 & \frac{\sqrt{3}}{l_c^2} \gamma \sqrt{(N+1)N} \\
0 & \frac{\sqrt{6}}{l_c} \gamma_3 \sqrt{N+1} k_z & \frac{\sqrt{3}}{l_c^2} \gamma \sqrt{(N+1)N} & \frac{\gamma_1 + \gamma_2}{l_c^2} \frac{2N+3}{2} + \frac{\gamma_1 - 2\gamma_2}{2} k_z^2
\end{array} \right]} \quad (5.2)$$

where l_c is the classical cyclotron orbit $(\hbar/eB)^{1/2}$. We have neglected the bandwarping by taking $\gamma_3 - \gamma_2 = 0$ and $\gamma = (\gamma_2 + \gamma_3)/2$. Since $u_i = 0$ for $i < 0$, the corresponding elements in Eq. (5.2) should be set to zero, and Eq. (5.2) is reduced to 3×3 , 2×2 , 1×1 for $N=1, 0, -1$ respectively. The total eigenvalue equation for the holes now becomes

$$\left[\frac{H_{ax}}{l_c^2 m_0} + \frac{\hbar^2 \kappa}{l_c^2 m_0} \underline{M}_J + \underline{U}(z) \right] G_N^j = E_N^j G_N^j \quad (5.3)$$

\underline{M}_J and \underline{U} are 4×4 diagonal matrices, with on the diagonal m , and the strain dependent valence band potential, respectively. The second term in Eq. (5.3), in which κ is the hole g-factor, describes the Zeeman splitting of the holes.

Eq. (5.3) is solved numerically, by the method outlined in chapter 2 and Ref. 24. This method is numerically exact but requires that Eq. (5.3) is transformed into a set of coupled first order real differential equations²⁶. Since Eq.(5.3) is second order and complex, this would yield 16 equations, plus two for normalization and energy continuity. We found by observation that G_N can be decoupled in two independent spinors, that both contain the same information as G_N . The two spinors are:

$$G_N^{(l)} = \begin{pmatrix} i \operatorname{Im}(g_N^{h+}(z)) \cdot u_{N-2} \\ i \operatorname{Im}(g_N^{l-}(z)) \cdot u_N \\ \operatorname{Re}(g_N^{l+}(z)) \cdot u_{N-1} \\ \operatorname{Re}(g_N^{h-}(z)) \cdot u_{N+1} \end{pmatrix}, \quad G_N^{(ll)} = \begin{pmatrix} \operatorname{Re}(g_N^{h+}(z)) \cdot u_{N-2} \\ \operatorname{Re}(g_N^{l-}(z)) \cdot u_N \\ i \operatorname{Im}(g_N^{l+}(z)) \cdot u_{N-1} \\ i \operatorname{Im}(g_N^{h-}(z)) \cdot u_{N+1} \end{pmatrix}, \quad G_N = G_N^{(l)} + G_N^{(ll)} \quad (5.4)$$

$\operatorname{Re}()$ an $\operatorname{Im}()$ denote the real and imaginary parts of the expression between brackets, respectively. Since any linear combination of these two spinors is a solution to Eq. (5.3), we can set one of these to zero, without changing the eigenvalue. By doing so, the number of first order differential equations is reduced to 10. This set of equations is

solved together with the Poisson equation to ensure self-consistency of the wavefunctions and electrostatic potentials. The parameters used in the calculations are listed in Table 5.1.

Electron eigenvalues and -functions are calculated from the standard one-dimensional Schrödinger equation, and corrected for non-parabolicity²⁷ by the expression $E_N = E(N, B, k_z)(1 + (K_2/E_g) * E(N, B, k_z))$, where $E(N, B, k_z)$ is the expectation value of the kinetic energy of the electron. The non-parabolicity parameter K_2 is calculated with the expression derived by Lindemann *et al.*²⁸. For GaAs and $\text{In}_{0.10}\text{Ga}_{0.90}\text{As}$ one obtains $K_2 = -0.83$ and -0.81 , respectively, using the parameters given in Table 5.1.

The strain dependent potentials $U_{v,h}$ and $U_{v,l}$ in Eq. (5.3) are calculated within the framework of the model-solid theory of van de Walle²⁹. Deformation potentials and elastic moduli are also taken from Ref. 29. For the band offset ratio of unstrained GaAs/ $\text{Al}_x\text{Ga}_{1-x}\text{As}$, for which material system reliable experimental data are available, we used the commonly accepted value of 0.7/0.3.

The exciton binding energy, E_b , was modeled using a modified version of the 2D hydrogen model described by MacDonald and Ritchie³⁰:

$$E_{ex}(n, \gamma) = E_{2D-H}(n, m=0, \gamma) - \gamma(2n+1)Ry_{scale} \quad (5.5)$$

In Eq. (5.5), $\gamma = \hbar\omega_c/2Ry_{scale}$, with Ry_{scale} the exciton effective Rydberg, that is used as a scaling parameter, and $\omega_c = eB/\mu^*$. μ^* is the effective exciton mass, $(1/m_e^* + 1/m_h^*)^{-1}$, with m_e^* and m_h^* the effective in-plane electron and hole masses, respectively. $E_{2D-H}(n, m=0, \gamma)$ is the energy of a two-dimensional n -s exciton with a zero-field binding energy of $4Ry_{scale}$. In Ref. 30 Ry_{scale} is equal to the *bulk* Rydberg, Ry^* . In the high-field regime ($\gamma \gg 1$) Eq. (5.5) reduces, for the 1s exciton ($n=0$), to

$$E_{ex}(B, Ry_{scale}) = - \left[\pi Ry_{scale} \frac{\hbar e B}{\mu^*} \right]^{\frac{1}{2}} \quad (5.6)$$

The effects of dimensionality and screening are accounted for by using Ry_{scale} as a free parameter. This scaling is essentially different from the one used in Refs. 21 and 22, where the high-field 2D result from Akimoto and Hasegawa³¹, is scaled with a dimensionality parameter D_j , with $D_j = 1$ ($1/4$) for 2D (3D):

$$E_{ex}(n, B, Ry^*) = -3D_j Ry^* \left[\frac{\hbar e B}{2(2n+1)\mu^* Ry^*} \right]^{\frac{1}{2}} \quad (5.7)$$

The zero field binding energy becomes $4D_j Ry^*$. It is obvious that Eqs. (5.6) and (5.7) are mathematically equivalent, apart from a constant factor. As a result, different exciton binding energies will be found when experimental data are fitted with either Eq. (5.6) or (5.7). We will come back to this in paragraph 5.3.

The question remains how Eq. (5.5) should be scaled in arbitrary magnetic fields, i.e. whether a dimensionality pre-factor, as in Eq. (5.7), should be used, or if the effective Rydberg should be scaled, as in Eq. (5.6). Belle³² has shown that the exact 2D result is a very close approximation to the adiabatic³³ 3D result. A prerequisite for this equality is that, in both limits, the magnetic field and energies are scaled as $\hbar\omega_c/Ry_{scale}$ ($=2\gamma$) and E/Ry_{scale} , respectively. Ry_{scale} should be taken Ry^* in the 3D limit and $4Ry^*$ in the 2D limit. As a consequence, the proper way to scale Eq. (5.5) is to scale the effective Rydberg Ry_{scale} .

It is worthwhile to point out that the basic assumption of our model is the following. Although it is known that the valence band non-parabolicity strongly effects the size of the exciton binding energy^{3,34}, the effect of non-parabolicity on its field dependence will probably be much smaller. The former effect can simply be compensated by adopting the appropriate value of Ry_{scale} which is the only free parameter in our description of the field dependence of energy levels.

In the above we have proposed that the dimensionality of the exciton can be

	GaAs	AlAs	InAs
γ_1	6.85	3.45	20.4
γ_2	2.1	0.68	8.3
γ_3	2.9	1.29	9.1
κ	1.2	0.12	7.68
ϵ_r	12.79	10.00	15.15
m_{el}^*	0.067	0.150	0.0239
Δ_{SO} [meV]	340	280	380
$Eg(\text{Al}_x\text{Ga}_{1-x}\text{As})$	$1519.2 + 1360 x + 220 x^2$ [meV]		
$Eg(\text{In}_y\text{Ga}_{1-y}\text{As})$	$1519.2 - 1583.7 y + 475 y^2$ [meV]		

Table 5.1 Parameters used in the numerical calculations. Where possible low-temperature (4.2K) values are taken. For ternary compounds linear interpolation is used. The parameters are taken from Ref. 46, bandgaps from Refs. 47 and 48.

accounted for by scaling the effective Rydberg. It is, however, not obvious that the effects of screening and bandfilling on the exciton energy and its field dependence can be caught by such a simple scaling. For example, Henriques *et al.* have shown that the Coulomb screening of an exciton in an unoccupied subband is strongly reduced in high magnetic fields due to the shrinkage of the exciton wavefunction³⁵. In paragraph 5.3 we will show experimentally that also screened excitons can be described by this 'scaled hydrogen model'.

5.3 Experiments

5.3.1 Samples and setup

In this study we will present results from two series of samples. The first consists of two p-doped $\text{Al}_x\text{Ga}_{1-x}\text{As}/\text{In}_y\text{Ga}_{1-y}\text{As}$ single quantum wells (SQW), with nominal indium concentrations of 0% and 10% and one undoped GaAs/ $\text{Al}_x\text{Ga}_{1-x}\text{As}$ 10-period multi-quantum well (MQW) structure. The second series consists of three p-doped Asymmetric Double Quantum Wells (ADQW). All samples were grown by conventional MBE techniques on $\langle 100 \rangle$ oriented GaAs substrates. The p-doped samples of the first series consist of a single quantum well, separated by a thin buffer layer from a short period superlattice. Both wells are nominally 95 Å wide, and symmetrically doped with Be δ -layers, which are separated from the well by 250 Å spacer layers. The GaAs well is confined by $\text{Al}_{0.45}\text{Ga}_{0.55}\text{As}$ barriers and grown at 690 °C. The $\text{In}_{0.10}\text{Ga}_{0.90}\text{As}$ well is confined by $\text{Al}_{0.25}\text{Ga}_{0.75}\text{As}$ barriers and grown at 500 °C to avoid indium diffusion. The MQW sample consists, nominally, of ten periods of a 100 Å GaAs SQW, confined by 500 Å $\text{Al}_{0.33}\text{Ga}_{0.67}\text{As}$ barriers. Each period was separated from its neighbors by 100 Å AlAs layers. The whole MQW was grown at 800 °C, on top of a short-period superlattice. The ADQW samples were also grown at 690 °C, and were separated by a 0.35 μm spacer layer from a short-period GaAs/AlAs superlattice. The Al-content of the $\text{Al}_x\text{Ga}_{1-x}\text{As}$ barriers was 40 percent. The Be-doping was distributed symmetrically over two δ -doping layer on either side of the single ADQW, that were separated by 150 Å spacer layers from the active layers. All samples are capped by a 170 Å GaAs layer. Fig. 5.1 shows the self-consistent valence band profiles and wavefunctions of a SQW and a ADQW sample. The MQW sample was characterized by high-resolution röntgen diffraction measurements. The well width was found to be 80 ± 2 Å and the Al content of the confining barriers was found to be 36 ± 1 %. X-ray diffraction spectra of the single

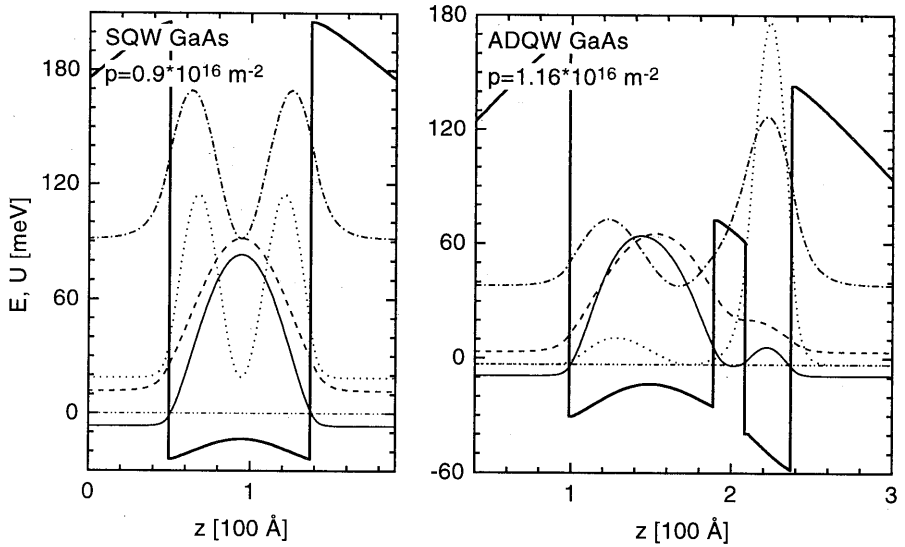


Fig. 5.1 Self-consistent potential and hole probability densities for the GaAs doped QW (left) and the ADQW with $p=11.6 \cdot 10^{15} \text{ m}^{-2}$. The lines have the following meaning: solid H0, dashed L0, dotted H1, dash-dotted L1, dash-double dotted E_F .

QW samples turned out to be hardly affected by the actual parameters of the single well. This is due to the relative narrowness of the single well, compared to the thickness of the total structure. The carrier densities, as obtained by transport measurements at 1.4 K, are $(9.0 \pm 0.1) \cdot 10^{15}$ and $(6.0 \pm 0.1) \cdot 10^{15} \text{ m}^{-2}$ for the GaAs and InGaAs SQW samples, respectively. Transport mobilities for both samples are typically around $10 \text{ m}^2/\text{Vs}$.

The magneto-photoluminescence and -excitation (PL, PLE) spectra were measured at 4.2 K. The samples were excited using normal incident light from a tunable Ti:Sapphire laser, pumped by an Argon ion laser. In order to assure that the optical spectra were not influenced by heating effects, care was taken that no change in the spectra occurred upon a decrease of excitation power. All experiments were performed in the Faraday configuration, using circular polarized light in excitation as well as in detection. This allows to separate the light and heavy hole components to the total absorption by using either cross (σ^+ or σ^-) or parallel (σ^{++} or σ^{--}) polarizations³⁶.

Part of the zero and low field measurements were performed in a different setup, which was described in an earlier publication¹⁷. Some PL(E) results on the single QW samples were also presented in this publication.

In the remainder of this chapter we will mainly focus on the first series of samples

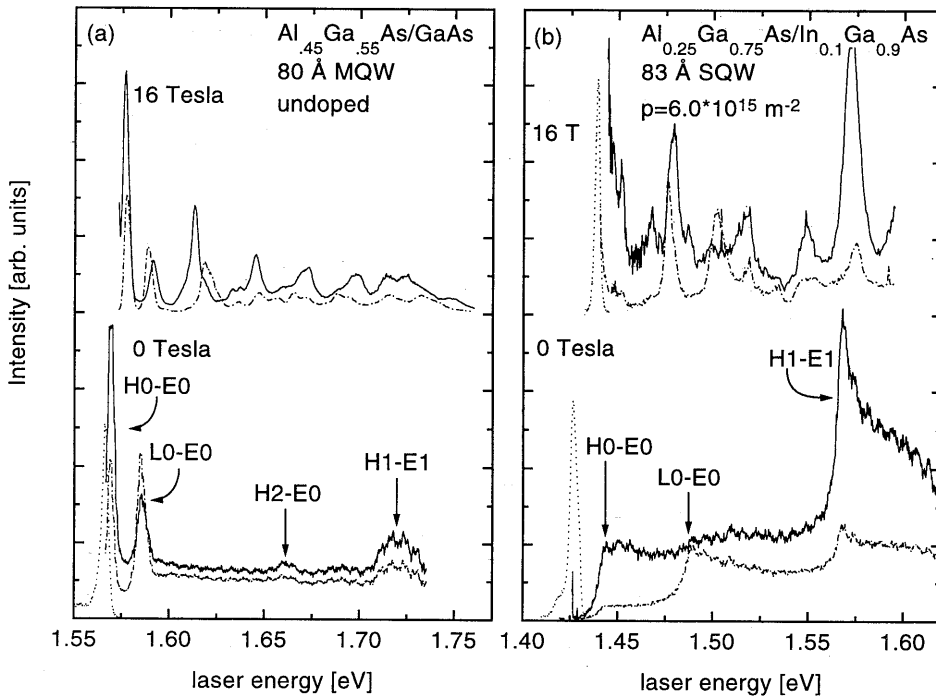


Fig. 5.2. Low-temperature (4.2 K) PL and PLE spectra at 0 and 16 Tesla for the undoped GaAs MQW (a) and the doped InGaAs SQW (b). Solid (dash-dotted) lines denote PLE spectra in σ^- (σ^+) polarization. The dotted lines are PL spectra.

(SQWs) since the ADQW samples show spectra that are qualitatively very similar to those of the SQW samples.

5.3.2 Results

In Fig. 5.2(a) raw PLE spectra of the undoped GaAs MQW sample are shown for zero and high magnetic field. In the zero field traces the strong absorption peaks of the H0-E0 and L0-E0 excitons, at 1.57 and 1.59 eV, are clearly visible. (In our notation Hi (Li) stands for a heavy (light) hole state with quantum number i . E.g., H0 is the heavy hole groundstate, and H1 the first excited heavy level.) Their relatively large full width at half maximum (FWHM) is the result of well width variations in the 10-period MQW structure. This also explains the absence of sharp absorption peaks for the H1-E1 (at

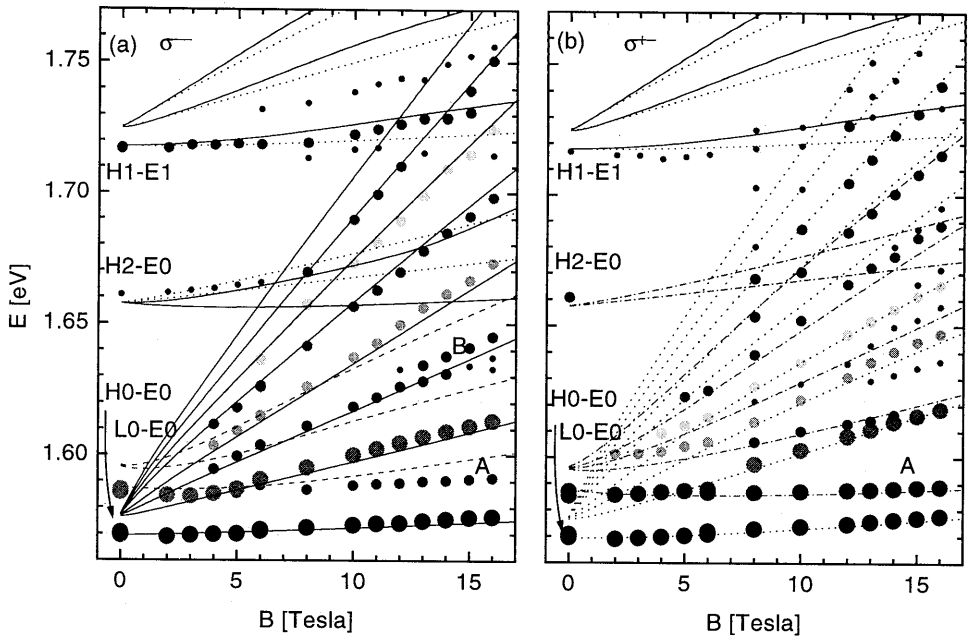


Fig. 5.3 Magnetic field dependence of PLE maxima of the undoped GaAs MQW, observed in σ^- (a) and σ^+ (b) polarization. The size of the dots is indicative for the absorption strength. The lines are calculations, using the model outlined in the text. Solid (dotted) lines denote $H \uparrow$ ($H \downarrow$) to $E \uparrow$ ($E \downarrow$) transitions. Dashed (dash-dotted) lines denote $L \uparrow$ ($L \downarrow$) to $E \uparrow$ ($E \downarrow$) transitions. For clarity, in the groundstates only those transitions are depicted that, at $k=0$ and $B=0$, can be excited by the incoming light, according to the selection rules for circular polarized light.

1.72 eV) and H2-E0 (at 1.66 eV) excitons. Since the binding energies of these excited subbands are more sensitive to well width fluctuations than those of the ground states, the exciton absorption peak is also much stronger smeared out for these higher subbands. In the following we will show that these transitions still are of excitonic nature, although the corresponding enhancement of oscillator strength is blurred. The 16 Tesla PLE traces in Fig. 5.2(a) show pronounced, but again broadened, Landau levels.

The zero field PLE spectra of both doped SQWs qualitatively differ from the ones of the undoped MQW. In Fig. 5.2(b) this is illustrated by the spectra of the InGaAs SQW. Both the H0-E0 and L0-E0 absorption onsets lack the excitonic enhancement that is present in the spectra of Fig. 5.2(a), whereas the H1-E1 onset still shows excitonic effects. This already suggests that the Coulomb screening by the sea of free (H0) holes is more efficient for the L0-E0 exciton than for the H1-E1 exciton. Note that the

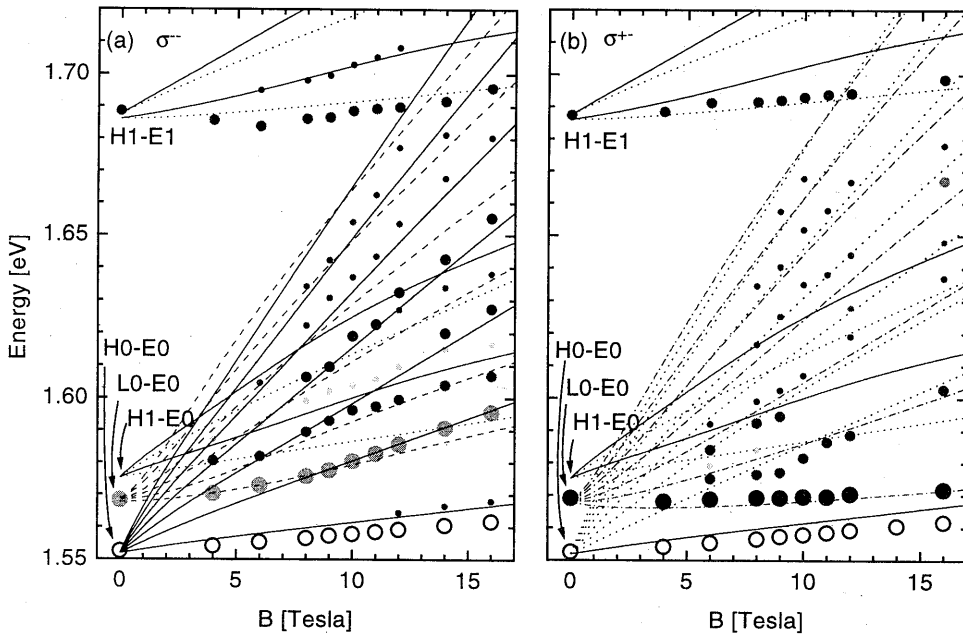


Fig. 5.4 Same as Fig. 5.3, for the doped GaAs SQW. The open symbols are taken from PL maxima instead of PLE.

enhancement of the H1-E1 absorption onset cannot be due to a second order van Hove singularity, since the H1 mass differs significantly from the electron mass¹⁷.

The summary of all magneto-PL(E) measurements in two polarization configurations is displayed by the dots in Figs. 5.3, 5.4 and 5.5. The size of the dots is indicative of the strength of the absorption. Errorbars are typically of the size of the smallest dots (1-2 meV), except for the H2-E0 and H1-E1 transitions in the undoped GaAs MQW and for the H1-E1 transition in the doped GaAs SQW, where the errorbar is approximately of the size of the intermediate dot (4 meV). The lowest lines of the doped QWs are taken from emission (PL) spectra, since absorption (PLE) is prohibited by the occupation of the lowest Landau levels. Being due to emission, the detected PL line is selected by the detection polarization, in contrast with the PLE lines, which are selected by the excitation polarization.

The lines in Figs. 5.3-5 are calculated using the model outlined in the previous section. The parameters used in the calculations are listed in Table 5.1. In the numerical calculations, the well width and, for the doped samples, the band gap renormalization

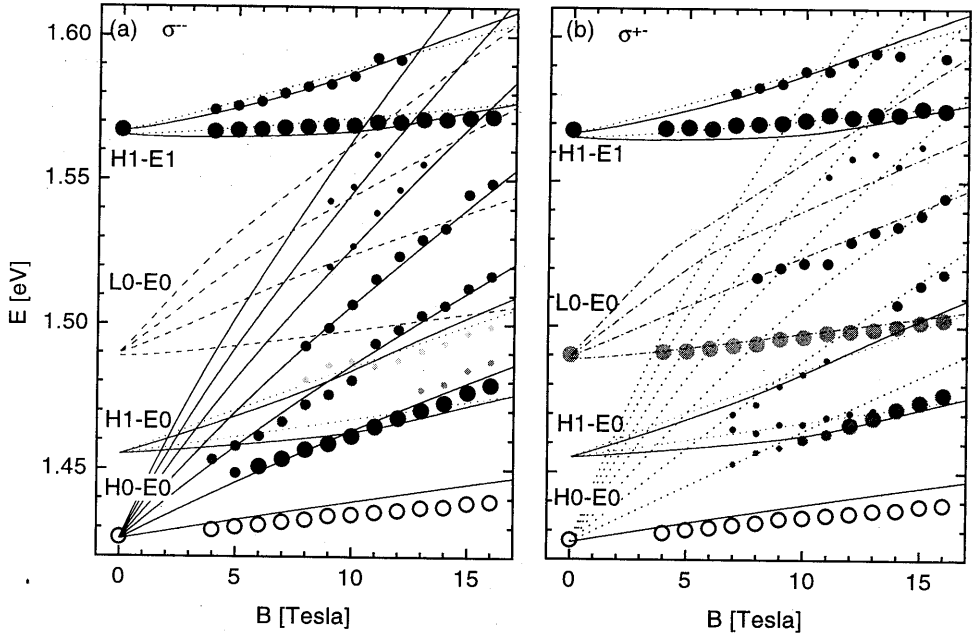


Fig. 5.5 Same as Fig. 5.3, for the doped InGaAs SQW. The open symbols are taken from PL maxima instead of PLE.

(BGR) were used as free parameters. The BGR was incorporated as a rigid shift of all bands. Recent LDA calculations, in which the complications due to the coexistence of both heavy and light holes were taken into account, proved this assumption to be justified within a few meV³⁷. Therefore, the well width was fully determined by the energetic separation between the H0-E0, L0-E0 and H1-E1 transition onsets, which were corrected for their respective exciton binding energies. These exciton binding energies, in turn, were obtained by minimizing the difference in magnetic field dependence of the calculated and measured transition energies. The total procedure is, of course, a sort of self-consistency problem, which was solved by iteration. Fortunately, the calculated free Landau levels hardly depend on small changes in well width, which effectively makes the exciton binding energy the only free parameter in describing the field dependence of the various levels. For the MQW, the well dimensions could also be obtained from high resolution X-ray diffraction measurements. The value found was 80 ± 2 Å for both methods. The BGR that was found for the GaAs SQW was 17 ± 2 meV, were the calculations³⁷ gave 20 meV.

The effective hole mass, needed in Eq. (5.5) for the calculation of the field dependence of the exciton binding energy, was taken as the average mass of the lowest calculated Landau level, in the field range from zero to 20 Tesla, $m_{av}^* = \frac{1}{2} \hbar e \Delta B / \Delta E$. The used values are given in Table 5.2. These masses are only meant to characterize the lowest LL of each subband and should not be confused with the effective mass at the Fermi level, which is obtained by e.g. temperature dependent Shubnikov-de Haas measurements. It should be noted that the field dependence of the exciton binding energy is hardly dependent on the hole mass used in Eq. (5.5). For a zero field 1s binding energy of 10 meV and an electron mass of $0.067 m_0$ the binding energy at 20 T is 22.6 meV for a hole mass of $0.3 m_0$ and 21.8 meV for a hole mass of $0.6 m_0$. For higher excitons the difference is even smaller.

5.4 Discussion

5.4.1 Spectral features

The general agreement between the observed and calculated magneto-optical fan charts, as depicted in Figs. 5.3-5, is apparent. Several features, however, are worth some further discussion.

First, as was indicated in paragraph 5.2.1, our model does not account for anticrossings that result from the Coulomb interaction between different excitons. In situations where the anticrossing is abrupt, i. e. has a small anticrossing gap, this is not troublesome for the present purposes. This can, for example, be illustrated by the level marked A in Fig. 5.3(b), which is the $L0\downarrow-E0\uparrow$ 1s exciton. Although Bauer and Ando¹⁹ have shown that this state ($l_1(1s)$ in their notation) experiences a sharp anticrossing -with $h_1(3d)\downarrow$ - in the low field region, the state that is optically active follows the field dependence of the non-anticrossing $L0\downarrow-E0\uparrow$ 1s exciton. Only in very narrow QWs, where this anticrossing gap is much larger, the actual anti-crossing can be resolved³⁸. A situation in which our model fails can be found in Fig. 5.3(a), at the level marked B. Here an anticrossing with, probably, a $H1-E0$ state is observed. This anticrossing was also observed by Rogers *et al.*²². Such a 'missed anticrossing' might also explain the deviation between calculation and experiment at A in Fig. 5.3(a). In this polarization (σ^-) the low-field anticrossing between $l_1(1s)$ and $h_1(3d)$ is far less abrupt than in σ^+ polarization¹⁹. This enhances the magnetic field region where the anticrossing levels deviate from the non-anticrossing ones, which could cause the deviation of our model from the

experimental points. For the degenerate samples, 'missed anticrossings' are irrelevant since the Coulomb interactions involved are much smaller due to the screening by the free holes.

Secondly, in the doped SQWs only Landau levels that are above or at the Fermi energy are visible in absorption. As an example, the filling factor of the InGaAs SQW is 6 at 4.1 T and 4 at 6.2 T, which corresponds quite closely to the visibility onsets of the corresponding H0-E0 absorption lines in Fig. 5.5(a). The lowest H0-E0 transition is, due to the phase space filling, only visible in PL. At the highest magnetic fields a small, additional peak arises in the PLE spectra, a few meV above the PL line, see Fig. 5.4(a) and (b)³⁹. We attribute this to absorption in the high-energy tail of the lowest H0, \uparrow and \downarrow , Landau levels. Therefore, these points should lay above the calculated transition energies. The PL energies are red-shifted with respect to the calculated energies due to the Stokes shift, which results from local variations in the QW properties.

sample	binding energy [meV]				Hole masses		
	H0-E0	L0-E0	H1-E1	Width [Å]	H0	L0	H1
GaAs MQW undoped	8±1	9±1	8±2	80±2	\uparrow :0.46 \downarrow :0.19	\uparrow :0.063 \downarrow :-0.19	\uparrow :0.045 \downarrow :0.19
GaAs SQW $p=9 \cdot 10^{15} \text{ m}^{-2}$	0	1±1	2±1	89±2	\uparrow :0.43 \downarrow :0.19	\uparrow :0.061 \downarrow :-0.19	\uparrow :0.042 \downarrow :0.19
InGaAs SQW $p=6 \cdot 10^{15} \text{ m}^{-2}$	0	1±1	2±1	83±2	\uparrow :0.10 \downarrow :0.19	\uparrow :0.083 \downarrow :0.14	\uparrow :0.15 \downarrow :0.19
GaAs ADQW $p=1.4 \cdot 10^{15} \text{ m}^{-2}$	3±1	7±1	12±2	90/28	\uparrow :0.45 \downarrow :0.19	\uparrow :0.067 \downarrow :-0.93	\uparrow :0.074 \downarrow :0.19
GaAs ADQW $p=6.5 \cdot 10^{15} \text{ m}^{-2}$	0	3±1	8±1	90/28	\uparrow :0.45 \downarrow :0.19	\uparrow :0.073 \downarrow :2.9	\uparrow :0.154 \downarrow :0.19
GaAs ADQW $p=1.2 \cdot 10^{16} \text{ m}^{-2}$	0	1±1	5±1	90/28	\uparrow :0.41 \downarrow :0.19	\uparrow :0.10 \downarrow :0.10	\uparrow :0.19 \downarrow :0.19

Table 5.2 Exciton binding energies, well widths and hole effective masses used in the calculations for Figs. 3, 4 and 5 (See text), and for the ADQW samples. The width values of the ADQW samples denote the nominal values of the wide and narrow well, respectively. The estimated uncertainty in the shown values is 3 Å.

Thirdly, the experimental Landau fans show several transitions that are forbidden by either parity or polarization, when the hole levels are considered parabolic, i.e. when the non-diagonal terms in Eq. (5.2) are neglected. These transitions can, however, be easily explained by non-parabolicity effects. Ancilotto *et al.*²¹ have discussed these effects extensively for an empty SQW, so we will limit ourselves to two illustrative examples. The visibility of the H1-E0 transition in Figs. 5.4 and 5.5 may seem surprising, but is a direct consequence of admixture in non-zero fields of states with quantum number 0 to the H1 state. This change of parity is due to k_z operators in non-diagonal elements of Eq. (5.2). Admixture of states with the same parity as the original state can explain the observation of transitions that are forbidden by the polarization selection rules. This is the case in Fig. 5.5(b), where H0 \uparrow -E0 \uparrow is observed in σ^+ polarization, due to admixture of L0 \downarrow to H0 \uparrow . We would like to point out that, although the strain in InGaAs/GaAs QWs enhances the parabolicity of the hole states in the sense that the effective mass remains constant over a wider range of fields and energies, the bandmixing cannot be neglected in In $_y$ Ga $_{1-y}$ As QWs.

5.4.2 Exciton screening

The H0-E0 transitions in the doped SQWs can be accurately described by setting the exciton binding energy to zero, i.e. setting Ry_{scale} to zero in our model, see also Table 5.2. This is in agreement with both theoretical^{1,3} calculations and other experimental work⁴⁰. It could be suggested that the increase with field of the energetic separation between the PL line and the calculated lowest Landau level is an indication that a finite binding energy still exists for the H0-E0 exciton. There are, however, several arguments against this hypothesis. Firstly, all higher Landau levels, that are observed in absorption instead of emission, seem to lay at the correct energies. Secondly, the small absorption peaks just above the PL lines are in accordance with the calculations, as argued above. Furthermore, Gravier *et al.*⁴¹ experimentally observe, for a similar p-doped SQW, that the difference between the Stokes shifted PL line and the lowest PLE line, increases with magnetic field. Since PLE lines are generally regarded as a correct measure for the 'true' transition energy, the observation by Gravier *et al.* supports our argument.

For the L0-E0 and H1-E1 transitions, the correspondence between measurement and calculation is significantly better when a finite exciton binding energy is used, than when it is omitted. This shows that a finite exciton binding energy remains present up to very high free carrier concentrations when the screening is purely of Coulombic nature.

This is a very strong confirmation of various theoretical works in which it was argued that 2D Coulomb screening cannot fully destroy the exciton binding energy, and one bound state remains at all densities^{1,3,42}. However, the conclusion of Ref. 9 that 'intersubband effects via Coulomb screening are negligible' in modulation doped QWs, seems unjustified. The fact that, in the doped wells, a smaller binding energy is found for the L0-E0 exciton than for the H1-E0 exciton, is in good qualitative agreement with the zero-field absorption spectra. As can be seen from Fig. 5.2(b), an excitonic enhancement of the L0-E0 absorption is fully absent, whereas it is clearly present for H1-E1.

The extremely small binding energy that is obtained for the L0-E0 excitons (1 ± 1 meV) is in good agreement with the results of Refs. 1 and 3 who find 0.2 and 0.5 meV, respectively. In contrast, the H1-E1 binding energy seems to be underestimated in the calculations of Ref. 3 by almost its full value: we find 2 ± 1 meV, versus (almost) zero in Ref. 3. This discrepancy is probably due to the purely 2D model in which the screening was calculated. Although the finite extent of the screening subband, H0, in the z -direction is taken into account by a formfactor, only the average electrostatic potentials of the screened excitons and the average density of the screening subband are used, as was pointed out by Henriques⁴. This leads to a dielectric constant $\epsilon(\mathbf{q})$ that is independent of z . Due to the fact that the H0 subband and the H1-E1 exciton have their maximum charge densities ($\sim |G(z)|^2$) at different z values, this procedure results in an overestimation of the screening efficiency and hence an underestimation of the exciton binding energy. For the L0-E0 exciton this effect is of minor importance due to the similarity of the H0, L0 and E0 wavefunctions. It is important to note that the InGaAs H1-E1 exciton binding energy found in this work, 2 ± 1 meV, is consistent with the result from temperature dependent absorption strength measurements on the same sample, which yielded an E_b between 1.0 and 2.5 meV¹⁷.

The absence of exciton binding for H0-E0, and its presence for L0-E0, shows the effects of occupation, by phase-space filling and exchange, on the exciton bleaching. Since the H0 and L0 wavefunctions are almost equal, the effect of Coulomb screening will be almost the same for the H0-E0 and L0-E0 excitons, as discussed above. Differences in exciton bleaching between these two subbands therefore necessarily arise from the difference in occupation. Our results do therefore also confirm the theoretical claim that no excitonic bound state exists for highly degenerate subbands.

In order to verify our hypothesis on the importance of subband overlap for Coulomb screening, we performed similar measurements on a series of ADQWs with various hole densities. As the overlap effect in these samples is much more pronounced

than in the single quantum wells (the groundstates are mainly localized in the wide well, whereas the first excited states are dominant in the narrow well, see Fig. 5.1), the differences in binding energy between the L0-E0 and H1-E1 excitons should also be much larger than for the single wells. It can directly be seen in table 5.2 that this indeed is the case. Again, even at the highest densities the L0-E0 exciton preserves a finite binding energy. As both H0 and L0 are groundstates, their wavefunctions are rather similar and the Coulomb screening of the L0-E0 exciton by the H0 holes still is approximately as efficient as in the single QW. The spatial separation of the H0 and H1 states is much larger in the ADQW structures than in the single QWs, which leads to a strongly reduced screening efficiency of the H1-E1 exciton.

5.4.3 Comparison with other models

When we compare the exciton binding energies for the undoped MQW (Table 5.2) with those found by other authors for similar QWs -see e.g. Fig. 5 in Ref. 43 for a summary of various experimental results- it appears that our values for the H0 and L0 excitons are about 2 meV below the average for 80 Å QWs. The H0 binding energy is however still somewhat above the value reported by Ossau *et al.*⁴⁴, who determined E_b from the diamagnetic shift of the H0 exciton. A comparison with the results of Rogers *et al.*²², who determined the exciton binding energy of H0-E0 both from extrapolation of low field data and from fitting high-field data can easily be made. The high-field model used in Ref. 22 assumed linear Landau levels, that were corrected for electron non-parabolicity, and for excitonic effects. The latter correction was made using Eq. (5.7). Since the full expression Eq. (5.5) for E_b reduces to Eq. (5.6) in high fields, we can convert our E_b 's to the binding energies that fitting with Eq. (5.7) would yield by demanding equality of Eqs. (5.6) and (5.7). Table 5.3 summarizes all relevant binding energies. It is obvious that our full results compare more favorable with the binding energies obtained by low-field extrapolation, whereas our results using Eq. (5.7) agree with the corresponding high-field values found by Rogers. Although the latter values are somewhat closer to the values reported in Ref. 43, we stick to our original values since we doubt the scaling used in Eq. (5.7), for reasons pointed out in paragraph 5.2. The H1-E1 binding energy of 8 meV seems to be in reasonable agreement with the theoretical results of Refs. 34 and 3 who report 9.2 meV for a 150 Å well with $\text{Al}_{0.40}\text{Ga}_{0.60}\text{As}$ barriers and 6.5 meV for a 100 Å well with $\text{Al}_{0.25}\text{Ga}_{0.75}\text{As}$ barriers, respectively.

As was discussed in the introduction, various authors have used a model in which

the electron-hole pairs are described in terms of a scaled 2D hydrogen model^{38,40,41,45}. In our model, this comes down to replacing the exact hole Landau levels by their linear counterparts, and neglecting the electron non-parabolicity. When we fit to our experimental fan charts with this model, we find, for the undoped GaAs MQW, $E_b=8$ meV and $m_{H0}=0.6 m_0$ for the H0-E0 exciton, and $E_b=9$ meV and $m_{L0}=-0.6 m_0$ for the L0-E0 exciton. Considering the extreme non-linearity of the L0 Landau levels it may seem surprising that the L0-E0 binding energy is found to be the same as when the Luttinger model is used to calculate the hole energies. However, this correspondence reflects the fact that, in undoped QWs, the Coulomb energy fully dominates over the nonlinearities in the light and heavy hole Landau levels. Since the lowest H0 Landau levels are almost linear, the agreement between the simple and the full model is less surprising in this case. Large deviations are found when the fan charts of the doped GaAs QW are fitted in the 2D hydrogenic model. Here, the exciton binding energy no longer dominates over the Landau level nonlinearities, which makes the approximation of the exact Landau levels by their linear counterparts no longer valid. For the H0 we find an effective mass of 0.6. The L0-E0 could best be fitted with a L0 mass of -1.0, and a binding energy in the range of 4 to 7 meV. This, of course, is in flagrant contradiction with theoretical predictions, the result of the Luttinger model, and earlier work on the same sample¹⁷. It should be pointed out that the agreement with the experimental points is, in all aforementioned cases, far better for our model than for the 2D hydrogen model, particularly for the L0-E0 transition in the doped GaAs SQW. Due to the strain-enhanced linearity of the hole Landau levels in the InGaAs system, the 2D hydrogen model works satisfactory for the InGaAs SQW.

	This work		Rogers <i>et al.</i> (Ref. 22)			
	full	high field	low field		high field fit	
width	80 Å	80 Å	75 Å	100 Å	75 Å	100 Å
H0-E0	8±1	10±1	10	8	12±1	9.5±.5
L0-E0	9±1	14±1	11	9	-	-

Table 5.3 Comparison between exciton binding energies in an undoped GaAs QW, found in the current work and those found by Rogers *et al.* (Ref. 22). All values are in meV. See text for further explanation.

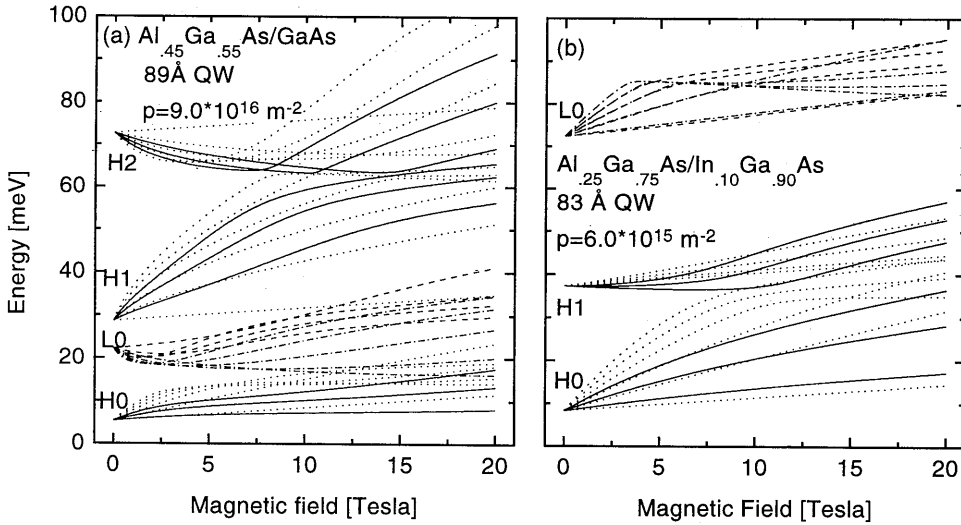


Fig. 5.6 Valence band Landau diagrams for (a) an unstrained 89 Å GaAs well, with $\text{Al}_{0.45}\text{Ga}_{0.55}\text{As}$ barriers and a hole concentration of $9.0 \times 10^{15} \text{ m}^{-2}$ and (b) a strained 83 Å $\text{In}_{0.10}\text{Ga}_{0.90}\text{As}$ well between $\text{Al}_{0.25}\text{Ga}_{0.75}\text{As}$ barriers, with a hole concentration of $6.0 \times 10^{15} \text{ m}^{-2}$. For clarity, only Landau levels with $N \leq 4$ are shown. The solid (dotted) lines are $H \uparrow$ ($H \downarrow$) Landau levels, the dashed (dash-dotted) lines denote $L \uparrow$ ($L \downarrow$) levels.

5.4.4 Numerical results

The hole Landau levels that are used for the generation of the lines in Figs. 5.3-5 are shown in Fig. 5.6. Fig. 5.6(a) displays the fan diagram for the unstrained 80 Å GaAs well, embedded between two $\text{Al}_{0.45}\text{Ga}_{0.55}\text{As}$ barriers, with a hole concentration of $9.0 \times 10^{15} \text{ m}^{-2}$. Fig. 5.6(b) shows the same for the strained 83 Å $\text{In}_{0.10}\text{Ga}_{0.90}\text{As}$ well between $\text{Al}_{0.25}\text{Ga}_{0.75}\text{As}$ barriers, with a hole concentration of $6.0 \times 10^{15} \text{ m}^{-2}$. The doping was assumed to be symmetrically distributed over two delta-layers on the left and right-hand side of the sample. Due to the axial component of the compressive strain in the InGaAs QW, the light hole levels are shifted upward with respect to the heavy hole levels. The two most striking effects of this shift are the disappearance of the negative L0 mass and the decreased H0 mass for higher Landau levels. Since the negative L0 mass in the GaAs QW is the result of a strong repulsive interaction between H1 and L0²¹, it changes sign as soon as the H1 level drops below L0. As this repulsive interaction is still present in the InGaAs QW, the H1 mass is strongly increased compared to the H1 mass in the GaAs SQW. The kink in the L0 Landau levels at 87 meV, see Fig. 5.6(b), is due to an

anticrossing with the H2 state. The disappearance of the negative LH0 mass is confirmed by the change in field dependence of the lowest L0-E0 transition in Figs. 5.4(b) and 5.5(b). The decrease of the H0 mass, going from GaAs to InGaAs, is also a consequence of the shift in the position of the L0 level. Since the extreme bending of the H0 Landau levels and its high effective mass are, in the GaAs QW, mainly caused by the anti-crossing with the L0 level, the 'removal' of the L0 level in the InGaAs SQW results in a smaller effective mass and a larger range in which the H0 Landau levels can be considered as linear.

The hole masses listed in Table 5.2 are, on first sight, remarkably constant for the heavy holes with 'spin' down ($m_j = -3/2$). For the GaAs wells, this can be understood by realizing that the masses listed are those of the lowest Landau level of each state. For the heavy hole down state, the lowest Landau level has $N = -1$ and the Hamiltonian Eq. (5.2) is reduced from 4×4 to 1×1 . In other words, heavy hole down states do not interact with other states and, consequently, their effective mass only depends on the Luttinger parameters. The constancy of the heavy hole down mass in going from GaAs to InGaAs is due to a cancellation of a decreasing in-plane mass [$\propto 1/(\gamma_1 + \gamma_2)$] and an increasing Zeeman energy⁴⁹ [$\propto (-\kappa)$ for 'spin' down states].

5.5 Conclusion

We have shown that in degenerate p-type samples, both the L0-E0 and H1-E1 excitons, which are only screened by the Coulomb interaction with the free groundstate heavy holes, are strongly screened. However, a finite binding energy remains present up to very high free carrier densities ($6\text{-}9 \times 10^{15} \text{ m}^{-2}$), in agreement with 2D screening theory. The H0-E0 exciton, in contrast, is totally unbound at these densities, due to the combined effects of Coulomb screening and occupation related bleaching. Furthermore, we have experimentally proven that the usual 2D RPA screening theory overestimates the screening strength for excited subbands. This is due to neglecting the z -dependence in the charge density of various subbands. Due to the similarity of H0 and L0 wavefunctions, the screening of the L0-E0 exciton is, for the studied QWs, predicted correctly by standard 2D screening theory.

We have successfully used a simplified model to describe the excitonic transitions in III/V heterostructures, which is based upon a separation of the full Hamiltonian into parts, that are solved separately. The extreme non-linearity of the H0 and L0 Landau levels can be reduced by incorporating compressive strain in the QW material, as was

found from both the experimental and the numerical results. However, for high fields and high Landau indices bandmixing remains important, as was confirmed by experimental observations on an $\text{In}_{0.10}\text{Ga}_{0.90}\text{As}$ QW.

References

1. D. A. Kleinman, *Phys. Rev. B* **32**, 3766 (1985).
2. A. E. Ruckenstein and S. Schmitt-Rink, *Phys. Rev. B* **35**, 7551 (1987).
3. G. D. Sanders and Y.-C. Chang, *Phys. Rev. B* **35**, 1300 (1987).
4. A. B. Henriques, *Phys. Rev. B* **44**, 3340 (1991).
5. S. Schmitt-Rink, D. S. Chemla, and D. A. B. Miller, *Phys. Rev. B* **32**, 6601 (1985).
6. R. Zimmermann, *Phys. Stat. Sol. (b)* **146**, 371 (1988).
7. W. H. Knox, C. Hirlimann, D. A. B. Miller, J. Shah, D. S. Chemla, and C. V. Shank, *Phys. Rev. Lett.* **56**, 1191 (1986).
8. E. Lach, M. Walther, G. Traenkle, A. Forchel, and G. Weimann, *Phys. Stat. Sol. (b)* **150**, 679 (1988).
9. K.-H. Schlaad, Ch. Weber, J. Cunningham, C. V. Hoof, G. Borghs, G. Weimann, W. Schlapp, H. Nickel, and C. Klingshirn, *Phys. Rev. B* **43**, 4268 (1991).
10. P. C. Becker, D. Lee, A. M. Johnson, A. G. Prosser, R. D. Feldman, R. F. Austin, and R. E. Behringer, *Phys. Rev. Lett.* **68**, 1876 (1992).
11. S. Hunsche, K. Leo, H. Kurz, and K. Koehler, *Phys. Rev. B* **49**, 16565 (1994).
12. W. H. Knox, R. L. Fork, M. C. Downer, D. A. B. Miller, D. S. Chemla, C. V. Shank, A. C. Gossard, and W. Wiegmann, *Phys. Rev. Lett.* **54**, 1306 (1985).
13. R. C. Miller and D. A. Kleinman, *Journ. Lum.* **30**, 520 (1985).
14. C. Delalande, G. Bastard, J. Orgonasi, J. A. Brum, H. W. Liu, M. Voos, G. Weimann, and W. Schlapp, *Phys. Rev. Lett.* **59**, 2690 (1987).
15. D. Huang, H. Y. Chu, Y. C. Chang, R. Houdre, and H. Morkoc, *Phys. Rev. B* **38**, 1246 (1988).
16. H. Yoshimura and H. Sakaki, *Phys. Rev. B* **39**, 13024 (1989).

17. M. Kemerink, P. M. Koenraad, and J. H. Wolter, *Phys. Rev. B* **54**, 10644 (1996).
18. D. R. Wake, H. W. Yoon, J. P. Wolfe, and H. Morkoc, *Phys. Rev. B* **46**, 13452 (1992).
19. G. E. W. Bauer and T. Ando, *Phys. Rev. B* **38**, 6015 (1988).
20. S.-R. E. Yang and L. J. Sham, *Phys. Rev. Lett.* **58**, 2598 (1987).
21. F. Ancilotto, A. Fasolino, and J. C. Maan, *Phys. Rev. B* **38**, 1788 (1988).
22. C. Rogers, J. Singleton, R. J. Nicholas, C. T. Foxon and K. Woodbridge, *Phys. Rev. B* **34**, 4002 (1986).
23. A. Broido and L. A. Sham, *Phys. Rev. B* **31**, 888 (1985).
24. M. Kemerink, P. M. Koenraad, P. C. M. Christianen, A. K. Geim, J. C. Maan, J. H. Wolter, and M. Henini, *Phys. Rev. B* **53**, 10000 (1996). Note that a factor 2 was accidentally omitted in the expression for b in eq. 2 of this publication. The matrix used in the actual calculations was correct.
25. S. -R. E. Yang, D. A. Broido, and L. J. Sham, *Phys. Rev. B* **32**, 6630 (1985).
26. G. Goldoni and A. Fasolino, *Phys. Rev. B* **51**, 9903 (1995).
27. E.D. Palik, G. S. Pikus, S. Teitler, and R. F. Wallis, *Phys. Rev.* **122**, 475 (1971).
28. G. Lindemann, R. Lassnig, W. Seidebush, and E. Gornik, *Phys. Rev. B* **28**, 4693 (1983).
29. C. G. Van de Walle, *Phys. Rev. B* **39**, 1871 (1989).
30. A. H. MacDonald, D. S. Ritchie, *Phys. Rev. B* **33**, 8336 (1986).
31. O. Akimoto and H. Hasegawa, *J. Phys. Soc. Jpn.* **22**, 181 (1967).
32. G. B. Belle, in *Magneto-Optical Studies of Quantum Wells and Superlattices*, Ph. D. Thesis, University of Nijmegen, section III.8 (1985).³³ The adiabatic approximation requires that the exciton wavefunction can practically be decoupled into contributions parallel and perpendicular to the magnetic field. This

procedure is only valid if $\gamma \gg 1$.

34. U. Ekenberg and M. Altarelli, Phys. Rev. B **35**, 7585 (1987).

35. A. B. Henriques, E. T. R. Chidley, R. J. Nicholas, P. Dawson, and C. T. Foxon, Phys. Rev. B **46**, 4047 (1992).

36. J. C. Maan, in *Physics and applications of Quantum Wells and Superlattices*, edited by E. E. Mendez and K. von Klitzing, Vol. 170 of *NATO Advanced Study Institute, Series B: Physics* (Plenum, London, 1987).

37. P. A. Bobbert, H. Wieldraaijer, R. van der Weide, M. Kemerink, P. M. Koenraad, and J. H. Wolter, Phys. Rev. B **56**, 3664 (1997).

38. M. Potemski, L. Viña, G. E. W. Bauer, J. C. Maan, K. Ploog, and G. Weimann, Phys. Rev. B **43**, 14707 (1991).

39. In Fig. 5.5 (a) and (b) (InGaAs SQW) these additional peaks should also be visible. However, these spectra suffer from 'ghost' lines, that are due to the monochromator and lay very close to the laser energy. This makes a proper analyses of peaks in this energy range impossible.

40. R. Stepniewski, M. Potemski, H. Buhmann, D. Toet, J. C. Maan, G. Martinez, W. Knap, A. Raymond and B. Etienne, Phys. Rev. B **50**, 11895 (1994).

41. L. Gravier, M. Potemski, A. Fisher, and K. Ploog, Solid State Electron. **40**, 697 (1996).

42. J. A. Brum, G. Bastard, and C. Guillemot, Phys. Rev. B **30**, 905 (1984).

43. E. S. Koteles and J. Y. Chi, Phys. Rev. B **37**, 6332 (1988).

44. W. Ossau, B. Jäkel, E. Bangert, G. Landwehr, and G. Weimann, Surf. Sci. **174**, 188 (1986).

45. M. Volk, S. Lutgen, T. Marschner, W. Stolz, E. O. Goebel, P. C. M. Christianen, and J. C. Maan, Phys. Rev. B **52**, 11096 (1995)

46. *Physics of Group IV elements and III-V Compounds*, edited by O. Madelung, M.

Schultz, and H. Weiss, Landolt-Börnstein, New Series, Group III, Vol. 17, Pt. a (Springer-Verlag, Berlin, 1982); *ibid.*, Vol. 22, Pt. a (Springer-Verlag, Berlin, 1987).

47. M. Guzzi and J. L. Steahly, in *Physics of DX Centers in III-V Ternary compounds*, edited by J. C. Bourgoin (Trans Tech, Aedermannsdorf, 1989).

48. K. H. Goetz, D. Bimberg, H. Jürgensen, J. Solders, A. V. Solomonov, G. F. Glinskii, and M. Razeghi, *J. Appl. Phys.* **54**, 4543 (1983).

49. For electronic Landau levels the Zeeman terms are not included when the effective mass is determined. For hole Landau levels the 'effective mass' is determined by the interaction with all other subbands. As these subbands in turn also experience a Zeeman energy, there is no consistent way of defining an effective mass without the Zeeman splitting.

6 Exchange interaction in p-type GaAs/ $\text{Al}_x\text{Ga}_{1-x}\text{As}$ heterostructures studied by magneto transport

(accepted for publication in Phys. Rev. B)

6.1 Introduction

In the past decades there has been considerable interest in the magnetic field dependence of the electronic g -factor, g^* . An enhancement of the electron g -factor owing to exchange interactions was first proposed by Janak¹ to explain experiments by Fang and Stiles². Later it was shown by Ando and Uemura³ that g^* should be an oscillatory function of the magnetic field with maxima at odd filling factors, i.e. when the Fermi level is in between the spin up and down states of a Landau level, and minima at even filling factors. The physical idea behind this periodic g -factor enhancement is the following: At large magnetic fields the spin up and down states of a Landau level near the Fermi energy have different occupations and therefore experience different exchange energies, leading to an enhanced gap between the two spin states. This enhanced splitting is usually described in terms of an enhanced g -factor. At odd filling factors, with E_F in between, say, $N\uparrow$ and $N\downarrow$, the occupation difference between the up and down levels is at a maximum, resulting in a maximum in g^* . From a similar reasoning the minimum in

g^* at even filling factors can be understood. At even filling factors the same effect should lead to an increase of the Landau level splitting $\hbar\omega_c$. This effect is usually neglected as for electronic LL, in most III/V semiconductors, the energy associated with this exchange interaction is much smaller than the LL spacing.

Experimentally, the exchange enhancement of g^* has been studied in various donor doped semiconductor heterostructures and in some of them oscillatory behavior has been reported^{4,5,6}. To our knowledge no experimental evidence has been reported for such effects in acceptor doped heterostructures.

In this work we report on magneto-transport experiments on a acceptor doped GaAs/Al_xGa_{1-x}As quantum well. We find direct evidence that, in this structure, exchange effects are important at odd and even filling factors. Furthermore, we find from numerical simulations that exchange effects are extremely important at magnetic fields as low as 1.5 T. As a result, the effective mass that is determined from temperature dependent Shubnikov-de Haas measurements should be treated with extreme care and can often be regarded as meaningless.

The remainder of this chapter is organized as follows. In paragraph 6.2 the experimental setup and results are discussed. In paragraph 6.3 we outline the model used for the numerical simulations that are presented and discussed in paragraph 6.4. Our conclusions are summarized in paragraph 6.5.

6.2 Experiments

The experiments were performed on a single 89 Å GaAs/Al_{0.45}Ga_{0.55}As quantum well (QW). The sample is p-modulation doped with Be and grown by standard MBE techniques on a (001) GaAs substrate. The carrier density, as obtained from Hall and SdH measurements, is $9.55 \cdot 10^{15} \text{ m}^{-2}$. The sample was wet-etched to a standard Hall-bar geometry and contacted with Au/Zn or Au/Sn in-diffused contacts.

Measurements in the temperature range of 60 to about 900 mK were performed with the sample mounted on the cold finger of a dilution refrigerator. For the temperature range of 1.2 to 4.2 K a pumped bath cryostat was used. Magnetic fields up to 11 T were generated by means of a superconducting coil. To exclude undesired carrier heating the measurement current was kept more than an order of magnitude below the value at which heating effects became observable. Typical values for the channel current and sheet resistance were around 25 nA and $500 \Omega\text{m}^{-2}$, respectively. Furthermore, all wiring of the dilution refrigerator was equipped with low-pass filters to prevent heating by RF noise.

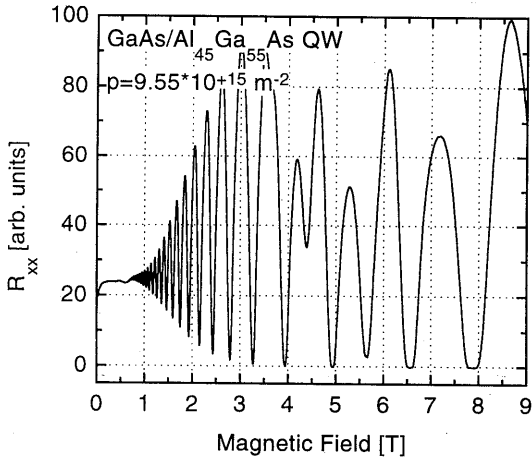


Fig. 6.1 Shubnikov-de Haas trace at 60 mK for the single quantum well.

heavy hole ‘spin’ ($m_j = \pm 3/2$) degeneracy at 4 T. The ratio of high- and low field periodicities deviates from the expected value of 2, which is assigned to exchange effects, that will be discussed in paragraph 6.4.

In studying thermal activation of resistance minima three magnetic field regimes can be identified. In the low magnetic field regime the densities-of-(extended)states (DOS) of many Landau levels overlap at the Fermi level. Only in this regime the Lifshitz-Kosevich¹⁰ formula applies and effective masses can be extracted from the temperature dependence of the oscillation amplitude. The high magnetic field regime, on the other hand, is characterized by the existence of mobility gaps. These are regions in between well separated Landau levels in which only localized states exist, and that, at low temperatures, give rise to plateaus in the Hall resistance and plateaus of zero conductance in the SdH traces. As long as $k_B T$ is much smaller than this mobility gap, the temperature dependence of conduction minima will show linearly activated behavior due to the thermal activation of carriers into the extended states¹¹. In the intermediate field regime the mobility gap is small or absent, and only the DOS of neighboring LL overlap. Here, activation measurements on conductance minima will only yield information about the shape of the DOS tails.

In order to analyze thermal activation of SdH minima in the high and intermediate magnetic field regimes one should, in principle, invert the longitudinal resistance R_{xx} to longitudinal conductance S_{xx} , using the well known tensor relation $\sigma_{xx} = \rho_{xx} / (\rho_{xx}^2 + \rho_{xy}^2)$. Here, σ_{xx} , ρ_{xx} and ρ_{xy} respectively denote the longitudinal conductivity, the longitudinal

A low temperature Shubnikov-de Haas (SdH) trace of the QW sample is displayed in Fig. 6.1. The SdH trace is very similar to those reported in publications on similar structures by other groups^{7,8,9}. By plotting extrema indexes vs. $1/B$ (not shown) we find low- and high- field periodicities of 18.6 and 39.5 T^{-1} , respectively. The latter corresponds to the density that is deduced from the position of the center of the Hall plateaus. The observed periodicity doubling is obviously due to a lifting of the

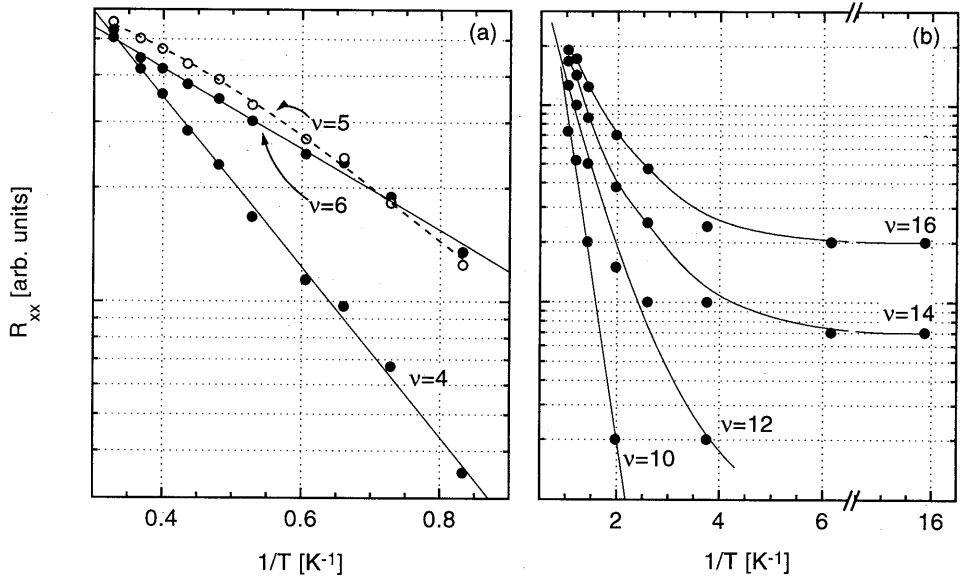


Fig. 6.2 (a) Temperature dependence of the resistance minima at $\nu=4, 5$ and 6 for the quantum well sample. The solid lines are linear least-squares fits, the dashed line is a fit with $A \exp[-(B/T)^2]$. (b) as panel (a), but for $\nu=10, \dots, 16$. Here, the solid lines guide the eye.

resistivity and the transverse or Hall resistivity. In our experiments ρ_{xx} is always at least one order of magnitude smaller than ρ_{xy} for magnetic fields above 1.5 T, so we may safely assume proportionality between ρ_{xx} and σ_{xx} . We therefore analyze the temperature dependence, at constant magnetic field, of R_{xx} , being the raw measurement data.

In Fig. 6.2 (a) we have plotted the high-field minima at $\nu=4, 5$ and 6 versus $1/T$, with $1.4 < T < 3$ K. Obviously there is a marked difference between the filling factors 4 and 6 on one hand and 5 on the other. The linearly activated behavior ($\nu=4, 6$) of resistance minima is what is to be expected in the absence of exchange effects, i.e. from the single particle picture sketched above. In the presence of exchange effects the same activation is at work, but then the separation between the two successive extended Landau levels, usually the spin up and down states of one single LL, is -partially- due to the exchange and hence a function of their occupancy. As the temperature is raised the occupation difference between these states is decreased and consequently their separation is decreased. Since the exchange splitting is, in first order, linearly proportional to the occupation difference³, the total activation behavior will be quadratic in T . The dashed line through the data points of $\nu=5$ is a fit to $A \exp[-(B/T)^2]$, validating the importance of exchange splitting for this conduction minimum. The behavior described for the p-

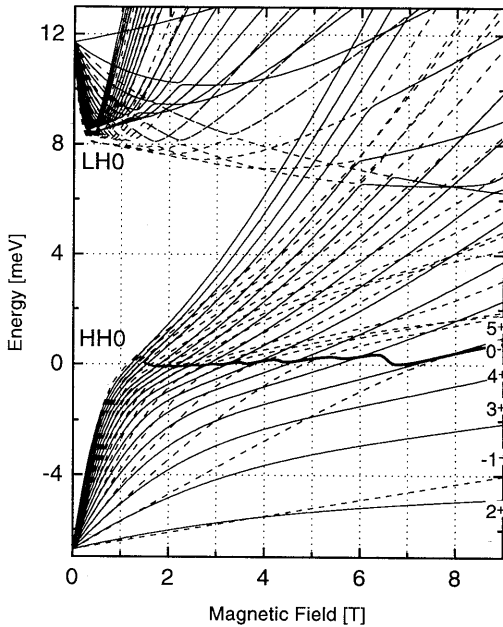


Fig. 6.3 Landau level diagram for the quantum well sample. Hole anisotropy has been included. Solid (dashed) lines indicate 'spin' up (down) levels. For the meaning of the numbers see text. The fat line denotes the Fermi level.

type QW is the same as what is to be expected for n-type systems or any system in which the Landau splitting is much bigger than the Zeeman energy.

Interesting information can also be obtained from the thermal activation of filling factor minima in the intermediate field regime. In Fig. 6.2 (b) the SdH minima at $\nu=10, \dots, 16$ are depicted for temperatures below 1 K. Here, the solid lines are guides to the eye. The most remarkable feature of Fig. 6.2 (b) is the nearly constant value of the resistance minima of $\nu=14$ and 16 at the lowest temperatures. We find that the observed behavior can not be explained in terms of simple, linear thermal activation nor be described in terms of the Lifshitz-Kosevich formula. The latter would

predict a far stronger temperature dependence in the low temperature regime when applied to the current minima. It is tempting to relate this non-linear behavior to exchange effects, like for $\nu=5$ in Fig. 6.2 (b). In paragraph 6.4 we will show that this indeed is the case.

6.3 Model

The numerical calculation of SdH traces consists of two parts. In the first part hole Landau levels are calculated that are used as input for the second part that calculates the actual R_{xx} traces. Exchange effects on the 'spin' splitting are included in the second part. Both steps will be outlined below in somewhat more detail.

The Landau level energies E_N were calculated from the 4×4 Luttinger Hamiltonian according to a method outlined elsewhere^{12,13}. Valence band anisotropy^{14,15,16} (warping)

was included using standard perturbation theory in which we used the unwarped LL as basis functions for the final, warped, levels. At zero magnetic field B , the energy levels and the electrostatic potential were calculated self-consistently. In this zero-magnetic field calculation, exchange-correlation potentials that account for the complications in the valence bands, were included¹⁷. The resulting fan chart for the quantum well structure is shown in Fig. 6.3. The numbers in the figure follow the Broido/Sham¹⁸ convention for hole Landau level indexing. From the small Landau level spacings at the Fermi level, one may draw the conclusion that, in the absence of exchange effects, the QW sample will show a very strong temperature dependence (\propto larger effective mass) of the SdH oscillation amplitude. One should bear in mind that the meaning of the effective mass that can be extracted from this temperature dependence is rather limited, considering the extremely non-linear nature of the Landau levels.

The calculation of the Shubnikov-de Haas traces follows in principle the work of Ando and Uemura¹⁹. According to Ref. 19 σ_{xx} is given by

$$\sigma_{xx} = \frac{e^2}{h} \sum_{N,i} \int_0^{\infty} -\frac{df}{dE} \left[\frac{\Gamma_{N,i}^{tr}}{\Gamma_{N,i}} \right]^2 \left[\exp \left(-2 \left(\frac{E - E_{N,i}}{\Gamma_{N,i}} \right)^2 \right) \right] dE \quad (6.1)$$

where $f(E)$ is the Fermi-Dirac distribution and the sum runs over all occupied subbands i and Landau levels N . From the original Ando-formulas¹⁹ the following analytical expressions were derived²⁰:

$$\begin{aligned} \left[\frac{\Gamma_{N,i}}{\Gamma_i} \right]^2 &= \frac{\sum_{k=0}^N \binom{N}{k}^2 \alpha^{4k}}{(\alpha^2 + 1)^{2N+1}} \\ \left[\frac{\Gamma_{N,i}^{tr}}{\Gamma_i} \right]^2 &= \frac{2N+1 + \sum_{k=1}^N \binom{N}{k}^2 \alpha^{4k-2} ((2(N-k)+1)\alpha^2 - 2k)}{2(\alpha^2 + 1)^{2N+2}} \end{aligned} \quad (6.2)$$

The quantity $\alpha = d/l$ relates the magnetic length l ($l^2 = \hbar/eB$) to the range of the scatterers d . Γ_i is usually given by the Born approximation for delta-shaped scatterers in low magnetic fields:

$$\Gamma_i = \left[\frac{2}{\pi} \hbar \omega_c \frac{\hbar}{\tau_0} \right]^{1/2} \quad (6.3)$$

In this work we used the value of Γ_i at $B=1$ T, $\Gamma_{ext,1/1}^{1T}$, as a free parameter for each ‘spin’ up resp. down subband, of which we only assumed proportionality to $B^{1/2}$. The reason for this is that Eq. (6.3) is no longer valid when the effective mass m^* becomes a function of the magnetic field B . Furthermore, it was shown in Ref. 21 that, even when the effective mass is independent of B , Γ_i is no longer proportional to $B^{1/2}$ in high magnetic fields. The latter effect turned out to be unimportant in the range of fields in which we used our model.

In Eq. (6.1) we assumed a Gaussian profile of the LL instead of the semi-elliptic profile that was calculated by Ando and Uemura¹⁹ and Xu and Vasilopoulos²¹. The reason was that it turned out to be impossible to produce Shubnikov-de Haas traces that resembled the experimental ones even slightly when semi-elliptic profiles were used. This is in accordance with other experimental observations^{22,23} and recent calculations based on a Gaussian random potential with long-range spatial correlations^{24,25}.

A fraction ϵ of the carriers in each Landau level was assumed to be localized due to strong localization. The localized states were also assumed to have Gaussian-shaped profiles, with a width $\Gamma_{loc,1/1}^{1T}$ at $B=1$ T, that are centered at the Landau energy E_N . In simulating experimental SdH traces it turned out that the best simulations were obtained when the width of the localized states was made so large that, effectively, a constant background of localized states arose. This, again, is in agreement with earlier experimental work^{22,23}.

The longitudinal conductance σ_{xx} calculated from (6.1) was transformed to the longitudinal resistance ρ_{xx} using the standard tensor relations and the classical approximation for the Hall conductivity $\sigma_{xy}=ne/B$, with n the total 2D carrier density. Shubnikov-de Haas effective masses in the low magnetic field regime were determined by calculating ρ_{xx} as a function of temperature and analyzing the resulting traces with standard Fourier filtering techniques and the well-known formula

$$\frac{\Delta\rho_{xx}(B)}{\rho_0} = 4 \sum_{s=1}^{\infty} \exp\left[\frac{-\pi s}{\mu_{q,l} B}\right] \cos\left[\frac{2\pi s(E_F - E_l)}{\hbar\omega_c} - \pi s\right] \frac{sX}{\sinh(sX)} \quad (6.4)$$

where $X=2\pi^2 k_B T / \hbar\omega_c$.

In order to validate our model we calculated SdH masses by the procedure outlined above, but using linear LL as input, i.e. assuming parabolic bands. We found that the resulting masses were, at least up to two decimal places, the same as those used for the calculation of the LL. This agreement was totally independent of the used parameter set, as long as the minima in ρ_{xx} did not reach zero. Using semi-elliptic

broadening profiles instead of Gaussian profiles did not alter this agreement.

The effects of exchange on the splitting between 'spin' up and down LL were included *a posteriori*. We used a simplified version of the model proposed by Ando and Uemura³, which was derived for, and successfully applied to, electron systems^{4,5,6}. The exchange energy of a Landau level N is written as

$$E_{Ex}^N = E_{Ex}^0 (n_1^N - n_{\bar{1}}^N) \quad (6.5)$$

where E_{Ex}^0 is a constant for which we assume^{5,6}

$$E_{Ex}^0 = E_{Ex}^{1T} B^{1/2} \quad (6.6)$$

where E_{Ex}^{1T} is the maximum exchange splitting at 1 T which is used as a free parameter and n_1^N and $n_{\bar{1}}^N$ are the relative occupations of the two spin states of the N -th Landau level. For hole LL the question remains which N should be assigned to the various hole Landau levels. The only consistent way to do this is by assigning the lowest 'spin' up and down Landau levels (2^+ and -1^- in Fig. 6.3) to the up and down states of the $N=0$ Landau level, and by assigning subsequent up and down hole LL to $N=1, 2, \dots$

Several objections can be made against the application of Eq. (6.5) to a 2D hole gas. Bobbert *et al.*¹⁷ have shown that the change from a spin doublet ($s=\pm 1/2$) for electrons to a 'spin' quadruplet ($m_j=\pm 3/2, \pm 1/2$) for holes strongly affects the exchange interaction. Furthermore, in the derivation of Eq. (6.5) pure spin states were assumed. Due to the strong bandmixing 'spin' is a poorly defined quantity in hole systems. Since there seems to be no theory on exchange in the Landau level regime that includes these features, we will use Eq. (6.5) as an 'educated guess'. In the next paragraph we will show that most experimental features can be explained qualitatively within the model outlined above.

Finally, it should be pointed out that the Fermi energy and the E_{Ex}^N are mutually dependent, and therefore form a self-consistency problem that is solved by iteration.

When linear Landau levels are used as input and exchange effects are excluded, the model outlined above is very well suited to study the intricacies of the SdH periodicity in systems in which not all carriers have the same mass. Examples are the 'spin' up and down branches of hole states in III/V's at nonzero B fields and electrons quantized in different X-valleys in $\text{Al}_x\text{Ga}_{1-x}\text{As}$ heterostructures²⁶ or Si inversion layers²⁷. As a demonstration we show in Fig. 6.4 calculated SdH traces for a -simplified- p-type heterojunction in which only the ground state heavy holes are occupied. The hole masses

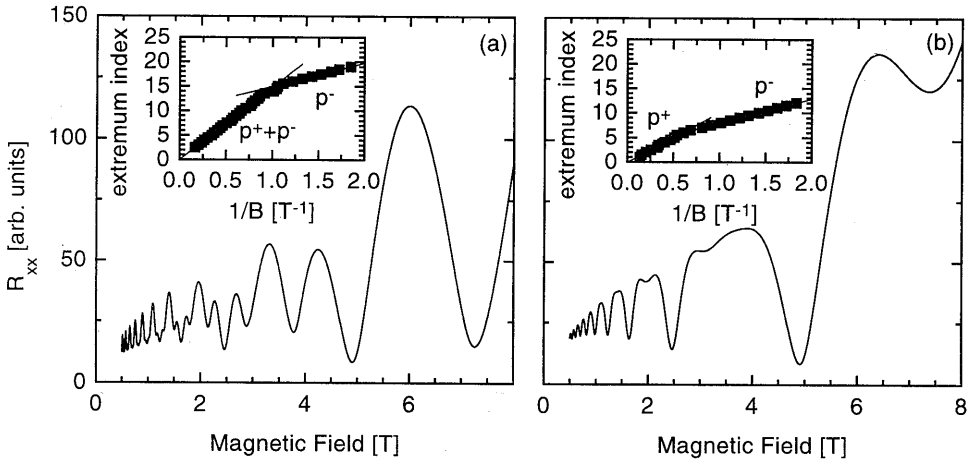


Fig. 6.4 Simulated Shubnikov-de Haas traces for a hypothetical heterojunction with $m^*_v = 0.4$ and $m^*_c = 0.2$ and a carrier density of $3.56 \cdot 10^{15} \text{ m}^{-2}$. $\Gamma_{ext,1}^{1T}$ and $\Gamma_{ext,1}^{1T}$ are 0.2 and 0.8 meV in (a) and 0.8 and 0.8 meV in (b).

were taken $0.4 \cdot m_0$ and $0.2 \cdot m_0$ for the $m_j = +3/2$, or 'spin' up, and $m_j = -3/2$, or 'spin' down, states, respectively. The total hole density p was taken $3.56 \cdot 10^{15} \text{ m}^{-2}$. In Fig. 6.4 (a), the widths of the extended states at 1 T, $\Gamma_{ext,1}^{1T}$ and $\Gamma_{ext,1}^{1T}$, were taken 0.8 and 0.2 meV, for up and down states respectively, and 0.8 and 0.8 meV in Fig. 6.4 (b). For simplicity, the fraction of localized states was assumed zero. As is apparent from the R_{xx} traces, the change from $\Gamma_{ext,1}^{1T} = 0.2$ meV in Fig. 6.4 (a) to $\Gamma_{ext,1}^{1T} = 0.8$ meV in Fig. 6.4 (b) causes a profound change in the SdH periodicity at higher fields. This is even clearer in the inserts, where the extremum index, not to be confused with the filling factor, is plotted versus $1/B$. In both situations, the low field oscillations are dominated by the 'spin' down holes, since the 'spin' down holes have the largest mobility. In Fig. 6.4 (a) the high field regime displays a periodicity that corresponds to the total density, $p^+ + p^-$, whereas the high field regime in Fig. 6.4 (b) is dominated by the periodicity of the 'spin' up holes, p^+ . The essential difference between situations (a) and (b) is the fact that in the high field regime of (a) the broadening of the 'spin' down LL is small compared to the spacing of the 'spin' up LL and that in (b) the reverse holds. In situation (b), as a result, the oscillations of the 'spin' up holes are superimposed on the slowly varying background of the 'spin' down holes, where the latter period consequently becomes dominated. It is worthwhile to point out that both situations have been observed in p-doped heterostructures. Situation (a), i.e. p^- in the low-field regime and $p^+ + p^-$ in the high-field regime, is

generally observed in single heterojunctions, see Refs. 7, 8 and 9. Situation (b), i.e. p^- and p^+ in the low- and high-field regimes respectively, has been reported for an asymmetric 50 Å quantum well⁷.

6.4 Numerical results and discussion

The model outlined in the previous paragraph has been used to simulate the Shubnikov-de Haas traces of Fig. 6.1. The results for the quantum well are plotted in Fig. 6.5. The Landau levels that are displayed in Fig. 6.3 are used as input for the simulations; other parameters used are given in Table 6.1. It turned out to be impossible to simulate both the high and low field regions of the experiment without including exchange

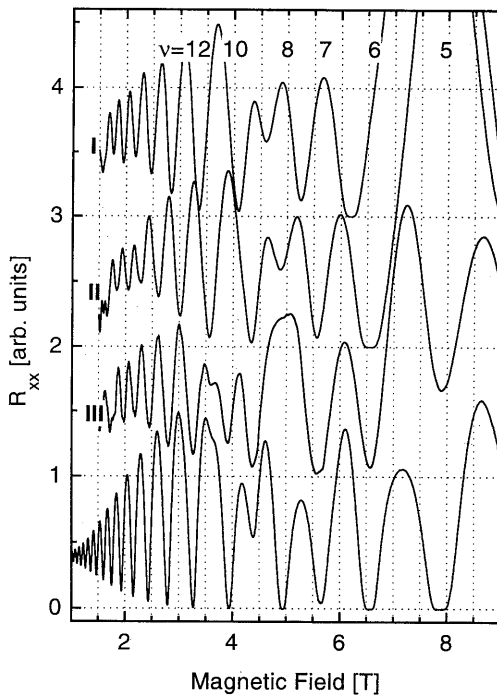


Fig. 6.5 Experimental and simulated Shubnikov-de Haas traces of the single quantum well. Curve I: $p=9.50 \cdot 10^{+15} \text{ m}^{-2}$, no exchange, curve II: $p=9.55 \cdot 10^{+15} \text{ m}^{-2}$, no exchange, curve III: $p=9.55 \cdot 10^{+15} \text{ m}^{-2}$, with exchange. Further parameters used in the simulations are given in Table 6.1.

interactions, see the upper two curves of Fig. 6.5. When we use the density from the high field SdH periodicity, $9.55 \cdot 10^{+15} \text{ m}^{-2}$, the low field oscillations are exactly out of phase with the experiment. Using the low field density, $9.0 \cdot 10^{+15} \text{ m}^{-2}$, solves this deviation but introduces large deviations in the high field regime. Only when we include exchange interactions in our model and use the high field density, satisfying agreement with the experiment can be obtained in the whole magnetic field range. It should be pointed out that when the low-field density is used in the simulations with exchange, the agreement with the experimental curve is very poor. From a comparison of the curves with $p=9.55 \cdot 10^{+15} \text{ m}^{-2}$ with and without exchange (middle two curves of Fig. 6.5) we can conclude that the

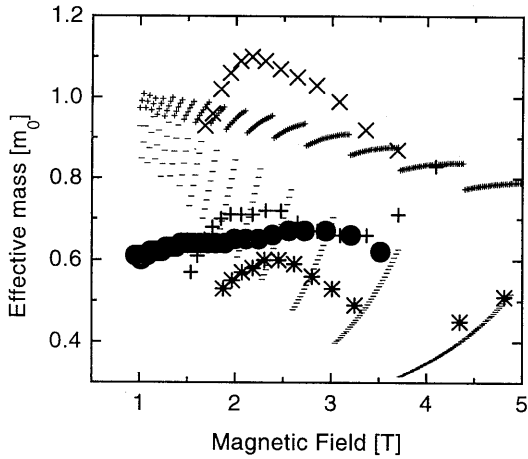


Fig. 6.6 Experimental and calculated effective masses versus magnetic field. The solid circles are experimental points, all other large symbols are calculated masses; +: no warping, no exchange; x: with warping, no exchange; *: with warping and exchange. The + and - lines are calculated cyclotron masses of the H0 'up' and 'down' bands, respectively, for Landau levels without warping and exchange. Only for LL with $E_{N, \uparrow/\downarrow} < E_F < E_{N+1, \uparrow/\downarrow}$ the cyclotron mass is plotted.

plotted experimental and calculated effective masses versus magnetic field. Because of the non-linear nature of the hole Landau levels and the presence of exchange interactions, the masses plotted in the figure should only be regarded as a measure of the

low field resistance minima occur at even instead of odd filling factors due to an exchange driven rearrangement of Landau levels. This implies that exchange interactions are important at magnetic fields as low as 2 T. Furthermore, we observe that the exchange indeed enhances the 'spin' splitting at $\nu=5$, in agreement with our interpretation of the activation measurements in Fig. 6.2 (a). At $\nu=8$ our simplified model fails in giving a proper description of the experiments. The reason for this is unclear at present.

If, as stated above, exchange is important in the low magnetic field regime, this should also be observable in the temperature dependence of the Shubnikov-de Haas oscillations. In Fig. 6.6 we

parameter	calculation			
	I	II, X	III, *	+
p [10^{+15} m^{-2}]	9.0	9.55	9.55	9.55
$\Gamma_{\text{ext}, \uparrow/\downarrow}^{1T}$ [meV]	0.28/0.28	0.25/0.25	0.55/0.55	0.28/0.28
E_{Ex}^{1T} [meV]	0	0	0.35	0
warping	yes	yes	yes	no

Table 6.1 Input parameters used in the calculations of Figs. 6.5 and 6.6. The roman numbers and the symbols refer to the curves in Fig. 6.5 and the symbols in Fig. 6.6, respectively. For all calculations we took $\epsilon=0.2$, $d=250 \text{ \AA}$ and $\Gamma_{\text{loc}, \uparrow/\downarrow}^{1T}=1.5 \text{ resp. } 1.5 \text{ meV}$.

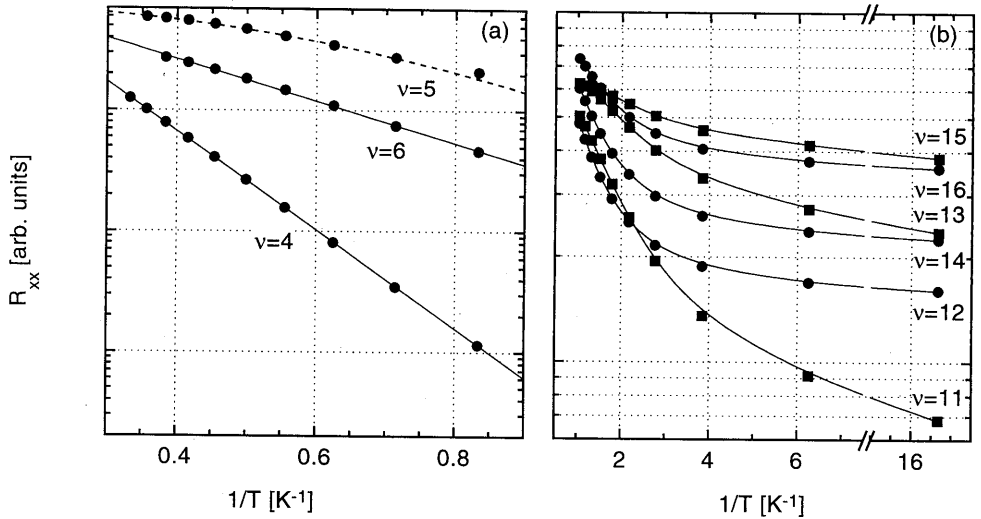


Fig. 6.7 (a) Calculated thermal activation of the conduction minima $\nu=4, 5$ and 6 of the quantum well, including exchange. As in Fig. 6.2(a), the $\nu=5$ minimum shows a quadratic activated behavior, indicative of exchange enhanced 'spin' splitting. (b) Calculated activation of resistance minima in the intermediate magnetic field regime. The density in the quantum well is taken to be $9.55 \cdot 10^{15} \text{ m}^{-2}$. The solid squares (circles) correspond to calculations without (with) exchange. The parameters used are the same as for the middle two curves in Fig. 6.5.

temperature dependence of SdH oscillation amplitudes, i.e. as an indication of the splitting between the highest occupied and lowest unoccupied Landau level. As from the simulation of the raw low-temperature SdH traces, we can conclude from the effective mass calculations that the single particle model, which neglects exchange effects, cannot explain the experimental observations. Once again it should be stated that the calculated effective masses do not depend significantly on any model parameter except E_{Ex}^{1T} . The good agreement between the experimental masses and those of the model calculations without warping and exchange is due to a cancellation of errors: When the band warping is included in the calculation of the hole Landau levels, an extra, repulsive, interaction between the H0 and L0 states is included^{14,16}. This results in a 'compression' of the H0 Landau fan, which can be expressed in terms of an increased effective mass. This demonstrates that the inclusion of band warping in hole Landau level calculations is not only essential for reproducing resistance minima in SdH experiments¹⁵, but also for the determination of single particle masses. When exchange interactions are included in the calculations, 'spin' up and down splittings at the Fermi level are increased. The thereby enhanced splitting between the highest occupied and lowest unoccupied Landau level is

observed as a decrease of the effective mass. For this reason we believe that the effective mass that is extracted from Shubnikov-de Haas measurements is rather meaningless. Another conclusion to be drawn from Fig. 6.6 is that the Shubnikov-de Haas masses are not equal to the cyclotron resonance masses, nor follow them in a simple manner, even when many-particle effects are absent.

A further confirmation of our interpretation of the present experiments can be obtained from the calculated thermal activation of resistance minima in the high and intermediate field regimes. In the discussion of Fig. 6.2 (a) the non-linear activation of the $\nu=5$ minimum was taken as an indication for an exchange-driven enhancement of a 'spin' splitting. Our simulations reproduce the observed behavior qualitatively: The $\nu=4$ and 6 minima exhibit linear activated behavior, whereas the $\nu=5$ minimum indeed shows a pronounced quadratic activation, see Fig. 6.7 (a). To produce a good local fit around $\nu=5$, including the broad plateau of zero resistance at 60 mK, we used $\Gamma_{ext,1}^{1T}, \Gamma_{ext,1}^{1T}=0.25$ meV instead of 0.55 meV, giving the best over-all simulation, which is used in the simulations of Figs. 6.5 and 6.6. It should be pointed out that also an increase of the exchange parameter E_{Ex}^{1T} can be used to reproduce the zero-resistance plateau, but also in this case a quadratic temperature dependence is found. Since neither E_{Ex}^{1T} nor $\Gamma_{ext,1}^{1T}$ and $\Gamma_{ext,1}^{1T}$ have a quantitative meaning in our model, and only the qualitative results of our model are important, this freedom in parameter choice is not troublesome.

In paragraph 6.2 the activation of resistance minima in the intermediate field regime of the quantum well SdH trace were discussed, and the claim was made that the extremely non-linear activation of the $\nu=14$ and 16 minima [see Fig. 6.2 (b)] is related to effects of exchange enhanced 'spin' splitting. In Fig. 6.7 (b) the activation behavior of various minima in the same magnetic field regime of calculated SdH traces are shown. The same parameters have been used as in the calculation of curves II and III in Fig. 6.5. Note that for the calculation without exchange resistance minima occur at odd filling factors, in contrast to the calculation with exchange and the experiment. Apart from this, additional support for our claim can be extracted from a comparison of Fig. 6.7 (b) with Fig. 6.2 (b). It is clear that the saturation at low temperatures of the experimental SdH resistance minima at $\nu=14$ and 16 is qualitatively far better reproduced by the model calculations that include exchange. As in the intermediate field regime no mobility gaps are present, the observed activation behavior is far more complicated than the simple $1/T$ or $1/T^2$ that is found in the high field regime. We found that at the lowest temperatures, the observed (lack of) temperature dependence predominantly reflects the shape of the tails of the LL density of states. The essential parameter determining this T dependence is therefore Γ_{ext}^{1T} . In the calculations with and without exchange Γ_{ext}^{1T} equals 0.55 and 0.25

meV, respectively, giving rise to the lesser temperature dependence at low temperatures in the former case. The importance of exchange interaction lays in the fact that it enhances the Landau level splitting at the Fermi level so that resistance oscillations are still observable, notwithstanding the fact that the Landau level broadening is larger than the splitting in the single-particle calculation, see Fig. 6.3.

There are two last questions that we want to address with respect to these simulations. The first concerns the magnetic field in which exchange effects become important. Our observations indicate that rearrangement of Landau levels due to exchange interactions is essential for a proper description of the transport experiments on p-type heterostructures at all magnetic fields. This is in marked contrast with the situation for n-type heterostructures, for which exchange effects become only significant at much higher magnetic fields⁵. The reason for this contrast is that the hole 'spin' splitting is not only due to the Zeeman effect, but also due to the different interactions with other bands for 'up' and 'down' hole levels. As a result, the total 'spin' splitting at the Fermi level is already much larger than the Landau level splitting for magnetic fields as low as 1 T, as can be seen in Fig. 6.3.

The second question concerns the generality of our results. In the above we have shown that for one particular GaAs/Al_xGa_{1-x}As QW exchange dominates the SdH resistance and the effective masses derived from its temperature dependence. It is however well known that, qualitatively, the dispersion relations and Landau levels of most GaAs/Al_xGa_{1-x}As heterostructures are the same. This also holds for the valence bands of most III/V-based heterostructures, in the sense that the hole g-factor and the interactions with other hole subbands lead to a much stronger 'spin' splitting than in the corresponding electron bands. Consequently, it is very likely that the exchange interaction is important in magneto-transport experiments on these structures. We feel that one should therefore be extremely carefull in using temperature dependent SdH measurements as a tool to obtain the single particle hole mass.

6.5 Conclusions

We have performed magneto-transport measurements on a p-type quantum well. From the thermal activation behavior of Shubnikov-de Haas conduction minima we concluded that exchange enhancement of 'spin' splittings can be important at both odd and even filling factors. Numerical simulations of Shubnikov-de Haas traces, based on realistic Landau levels and a simplified model for the exchange interaction confirmed

these observations. Furthermore, simulations showed that exchange interactions lead to a drastic rearrangement of hole Landau levels around the Fermi level at *all* magnetic fields, which is reflected in the observed Shubnikov-de Haas traces. This conclusion is strengthened by the observed temperature dependence of the Shubnikov-de Haas oscillation amplitude in the low magnetic field regime. We found that the observed behavior can not be described within the single particle model in which the Landau levels are calculated. Inclusion of exchange effects in the model did greatly improve the agreement of the calculations with the experimental data. These findings, in combination with the extremely non-linear nature of hole Landau levels, lead us to the conclusion that hole effective masses, deduced from temperature dependent SdH measurements, should be treated with extreme care and often can be regarded as totally meaningless.

Although the simplified model that we applied to take the effects of exchange on the hole Landau levels into account seems to give a qualitatively correct description of our experimental findings, a more extensive theoretical model could greatly improve on the understanding of many-body effects in p-type heterostructures.

References

1. J. F. Janak, *Phys. Rev.* **178**, 1416 (1969).
2. F. F. Fang and P. J. Stiles, *Phys. Rev.* **174**, 823 (1968).
3. T. Ando and Y. Uemura, *J. Phys. Soc. Jpn.* **37**, 1044 (1974).
4. Th. Englert, D. C. Tsui, A. C. Gossard, and Ch. Uihlein, *Surf. Sci.* **113**, 295 (1982).
5. R. J. Nicholas, R. J. Haug, K. v. Klitzing, and G. Weimann, *Phys. Rev. B* **37**, 1294 (1988).
6. J. X. Shen, W. Ossou, F. Fischer, A. Waag, and G. Landwehr, *Surf. Sci.* **361/362**, 460 (1996).
7. Y. Iye, E. E. Mendez, W. I. Wang, and L. Esaki, *Phys. Rev. B* **33**, 5854 (1986).
8. J. P. Eisenstein, H. L. Störmer, V. Narayanamurti, A. C. Gossard, and W. Wiegmann, *Phys. Rev. Lett.* **53**, 2579 (1984).
9. H. L. Störmer, Z. Schlesinger, A. Chang, D. C. Tsui, A. C. Gossard, and W. Wiegmann, *Phys. Rev. Lett.* **51**, 126 (1983).
10. A. Isahara and L. Smrcka, *J. Phys. C* **19**, 6777 (1986).
11. J. J. Koning, R. J. Haug, H. Sigg, K. v. Klitzing, and G. Weimann, *Phys. Rev. B* **42**, 2951 (1990).
12. M. Kemerink, P. M. Koenraad, P. C. M. Christianen, A. K. Geim, J. C. Maan, J. H. Wolter, and M. Henini, *Phys. Rev. B* **53**, 10000 (1996).
13. M. Kemerink, P. M. Koenraad, P. C. M. Christianen, R. v. Schaijk, J. C. Maan, and J. H. Wolter, *Phys. Rev. B* **56**, 4853 (1997).
14. S. R. Eric Yang, D. A. Broido, and L. J. Sham, *Phys. Rev. B* **32**, 6630 (1985).
15. W. Heuring, E. Bangert, K. Grötsch, G. Landwehr, G. Weimann, W. Schlapp, J. H. Reemtsma, and K. Heime, *Surf. Sci.* **229**, 76 (1990).
16. E. Bangert and G. Landwehr, *Surf. Sci.* **170**, 593 (1986).
17. P. A. Bobbert, H. Wieldraaijer, R. van der Weide, M. Kemerink, P. M. Koenraad, and J. H. Wolter, *Phys. Rev. B* **56**, 3664 (1997).

18. D. A. Broido and L. J. Sham, *Phys. Rev. B* **31**, 888 (1985).
19. T. Ando and Y. Uemura, *J. Phys. Soc. Jpn.* **36**, 959 (1974).
20. H. P. Assink, masters thesis, Eindhoven University of Technology (1990).
21. W. Xu and P. Vasilopoulos, *Phys. Rev. B* **51**, 1694 (1995).
22. G. Gobsch, D. Schultze, and G. Paasch, *Phys. Rev. B* **38**, 10943 (1988).
23. J. J. Harris, J. M. Roberts, S. N. Holmes, and K. Woodbridge, *Phys. Rev. B* **53**, 4886 (1996).
24. L. Spies, W. Apel, and B. Kramer, *Phys. Rev. B* **55**, 4057 (1997).
25. M. E. Raikh and T. V. Shahbazyan, *Phys. Rev. B* **47**, 1522 (1993).
26. S. Yamada, K. Maezawa, W. T. Yuen, and R. A. Stradling, *Phys. Rev. B* **49**, 2189 (1994).
27. B. Vinter and A. W. Overhauser, *Phys. Rev. Lett.* **44**, 47 (1980).

7 Many-particle effects in Be-delta-doped GaAs/Al_xGa_{1-x}As quantum wells

(submitted to Phys. Rev. B)

7.1 Introduction

The collective behavior of mobile carriers in a semiconductor lattice has attracted a lot of attention ever since the early days of semiconductor physics. With the advent of (quasi) two-dimensional (2D) systems, most of the many-body effects that had previously been studied in bulk semiconductors or metals, became subject of intense research in these new structures. Among these are such well-known effects as screening, the Fermi-edge singularity (FES) or Mahan exciton, exchange and correlation, etc. Since exchange and correlation effects lead to a reduction of the effective band gap in degenerate systems, their effect is often denoted as band gap renormalization or BGR. Although the basic concepts are not very new, all of these effects are still of great current interest^{1,2,3,4}. Both experimental and theoretical studies on many-particle effects have predominantly focussed on n-type systems, mainly to avoid the complications arising from the valence band coupling. However, due to the very different characteristics of the valence bands as compared to those of the conduction band, i.e. the co-existence of heavy and light hole groundstates, the high effective masses and the strong non-parabolicity, the study of p-type systems can greatly enhance the general understanding of many-body

physics^{5,6,7,8,9,10}.

In this paper we will report on photo-luminescence (PL) and photo-luminescence excitation (PLE) measurements on GaAs/Al_{0.20}Ga_{0.80}As quantum wells (QWs) with a Be delta (δ)-doping spike placed in the center of the well. These structures are ideal to study band gap renormalization because of the high carrier densities that can be achieved, and the occupation of multiple subbands. We will compare our results with the results of self-consistent field calculations, in which the effects of exchange and correlation have been incorporated by means of the local-density approximation (LDA). In particular, we will compare various models for the hole exchange-correlation potential with our experiments and with calculations without these many-body corrections. We find that the inclusion of exchange and correlation effects in self-consistent calculations is essential for a meaningful comparison with experiments, and that the model that has recently been developed by Bobbert *et al.*¹ consistently describes our experimental findings.

In a recent series of papers Wagner *et al.*^{11,12,13} report the observation of a FES in the luminescence spectra of structures that are very similar to the ones discussed here. From a theoretical point of view this observation is very remarkable^{4,14,15}. Both the small effective mass of the minority carriers and the large energetic separation between the highest occupied state and the lowest unoccupied state in the valence band, reported in Refs. 12 and 13, make the occurrence of a FES surprising. In our experiments we do not observe any indication for a Fermi-edge singularity. In paragraph 7.5 we will briefly discuss this negative result in the light of recent theoretical work on this subject, and we will compare our results to those of Wagner *et al.*

This chapter is organized as follows. In paragraph 7.2 we will describe the samples used in this work. Experimental results will be reported in paragraph 7.3 and discussed in paragraph 7.5. The numerical model used in the interpretation of our data is presented in paragraph 7.4, along with a comparison of measured and calculated transition energies. Paragraph 7.6 will summarize our conclusions.

7.2 Samples

The structures investigated were grown on semi-insulating GaAs substrates by conventional molecular-beam epitaxy techniques. On top of the substrate a 100-period GaAs/AlAs superlattice was grown, followed by a 200 Å Al_{0.20}Ga_{0.80}As barrier layer. Both the superlattice and the Al_{0.20}Ga_{0.80}As barrier were grown at 690 °C. Subsequently, the growth temperature was lowered to 480 °C to avoid Be diffusion during the growth

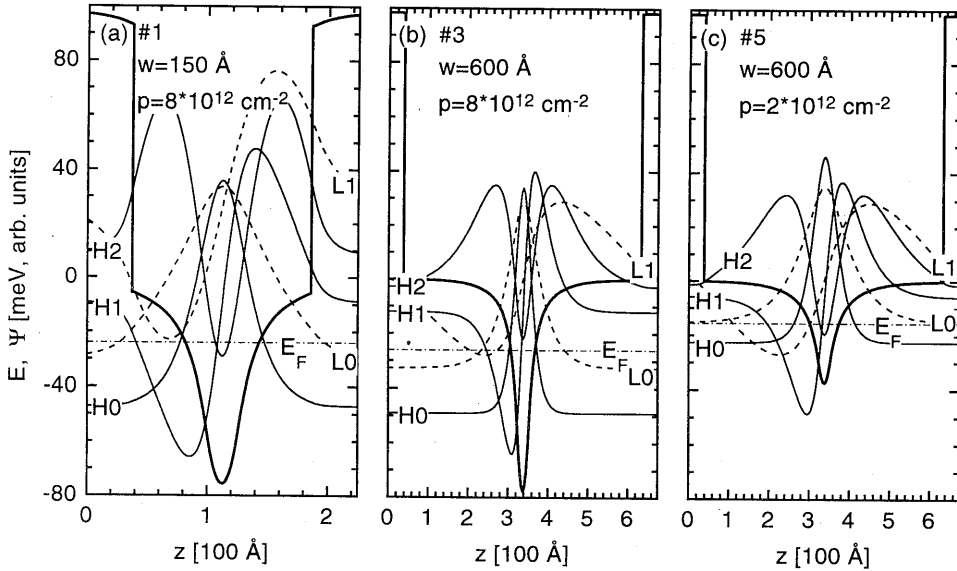


Fig. 7.1 Valence band self-consistent confining potential and wavefunctions of samples 1 (a), 3 (b) and 5 (c), calculated using the model outlined in the text. The thick solid line denotes the confining potential, the thin solid and dashed lines denote the heavy and light hole envelope wavefunctions, respectively. The dash-dotted line indicates the position of the Fermi level E_F .

of the active layers. The active layers consist of ten periods of the following structure: an undoped GaAs layer of width $w/2$, a Be δ -doping spike with a Be surface concentration p , deposited during a growth interrupt, another undoped GaAs layer of width $w/2$ and a 75 \AA $\text{Al}_{0.20}\text{Ga}_{0.80}\text{As}$ barrier. The total structure was terminated with another 125 \AA of $\text{Al}_{0.20}\text{Ga}_{0.80}\text{As}$ and a 100 \AA GaAs cap layer. In addition, a bulk Be-doped reference sample was grown. This structure consists of a single, $2 \mu\text{m}$ thick, bulk GaAs layer that had an aimed doping concentration of $2 \cdot 10^{18} \text{ cm}^{-3}$. It was grown at $630 \text{ }^\circ\text{C}$, directly on top of a semi-insulating GaAs substrate.

The motivation for growing a multiple quantum well structure, instead of a single QW, which is expected to show less broadened optical spectra, is threefold. Apart from the obvious increase in signal strength, two points are worth some further discussion. First, the two outer δ -doped wells will screen possible depletion fields, arising from mid-gap pinning of the Fermi level at the surface and in the substrate¹⁶. Therefore, the larger central part of the total structure will be unaffected by these uncontrollable fields, and thus will have a symmetric potential profile. This symmetry is essential in calculating the self-consistent solution of the coupled Poisson and Schroedinger equations. Furthermore,

Sample No.	well width [Å]	doping [10^{12} cm^{-2}]
1	150	8
2	300	8
3	600	8
4	1200	8
5	600	2
6	600	4
7	600	12
reference*	2 μm	$2 \cdot 10^{18} \text{ cm}^{-3}$

Table 7.1 Growth parameters of the investigated samples. The Be- δ -doping spike is placed in the center of the GaAs well region. The confining $\text{Al}_{0.2}\text{Ga}_{0.8}\text{As}$ barriers are 75 Å thick.

it has been shown by Rodriguez and Tejedor⁴ that the symmetry of the confining potential can strongly affect the appearance of Fermi-edge singularities. Also for this reason, uncontrollable and possibly illumination-dependent electric fields are undesirable. Second, since the surroundings of the active layers are screened by the two outer wells, the Fermi level in the central eight wells is solely determined by the doping in the δ -layers. The small (p-type) background doping concentration in the order of a few times 10^{14} cm^{-3} , resulting from contaminations in the MBE system, is fully negligible with respect to the amount of doping in the δ -layers. This also facilitates numerical simulations, as it allows for a restriction of the calculation interval to the active layers. Furthermore, as δ -doped samples are not expected to show very sharp optical lines, some broadening due to fluctuations over the ten periods of active layers is acceptable.

Two series of δ -doped samples were grown. One with a variable doping concentration p , ranging from 2 to $12 \cdot 10^{12} \text{ cm}^{-2}$, at a fixed well width $w=600 \text{ Å}$, and one with a variable well width, in between 150 and 1200 Å, at a doping level of $p=8 \cdot 10^{12} \text{ cm}^{-2}$. In Table 7.1 the relevant growth parameters are listed. In Fig. 7.1 (a-c) self-consistent potentials and wavefunctions of three representative structures are displayed. The model used for the calculations is described in paragraph 7.4.

7.3 Experimental results

The experiments described in this paper are performed with the sample mounted in a continuous-flow He cryostat, in which temperatures from 4 to 300 K can be reached. Unless stated otherwise, all reported data are taken at 5 K. The samples were excited using either a tunable Ti:Sapphire laser, or the yellow 594 nm (2.087 eV) line from a He-

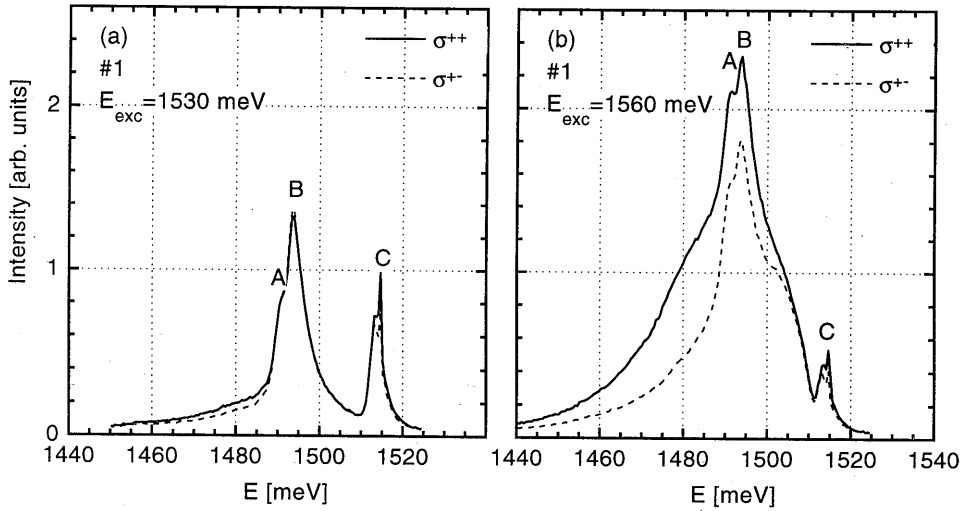


Fig. 7.2 Polarization-resolved photo-luminescence spectra of sample 1, excited at 1530 meV (in the Moss-Burstein gap, panel a) and at 1560 meV (above the Moss-Burstein gap, panel b). The solid and dashed lines are taken in parallel (σ^{++}) and cross (σ^+) polarization configuration, respectively. The identification of peaks A, B and C is discussed in the text.

Ne laser. The former source excites below the band-gap of the 20% $\text{Al}_x\text{Ga}_{1-x}\text{As}$ barriers (1800 meV), the latter above. Both the excitation and detection beams were aligned perpendicular to the sample surface (back-scattering configuration). Using polarization selective excitation and detection, i.e. using left (σ^-) or right (σ^+) circularly polarized light, heavy and light hole contributions to the optical spectra of the 2D structures could be separated. The excitation densities were approximately 1 and 0.15 Wcm^{-2} for PL and PLE, respectively. The luminescence signal was dispersed by a double 0.75 m Spex monochromator and detected using a cooled GaAs photo multiplier, connected to a DC-electrometer.

At the high-energy side of the PL spectra of all δ -doped samples, structure appears that seems to be independent of the well width and doping concentration. Also the PLE spectra of these samples show a 2D-structure independent background signal, that is sensitive to the detection wavelength. We will first identify these structure independent features in the PL(E) spectra of the δ -doped samples as being due to bulk GaAs. Then, the 2D-related PL(E) spectra will be discussed.

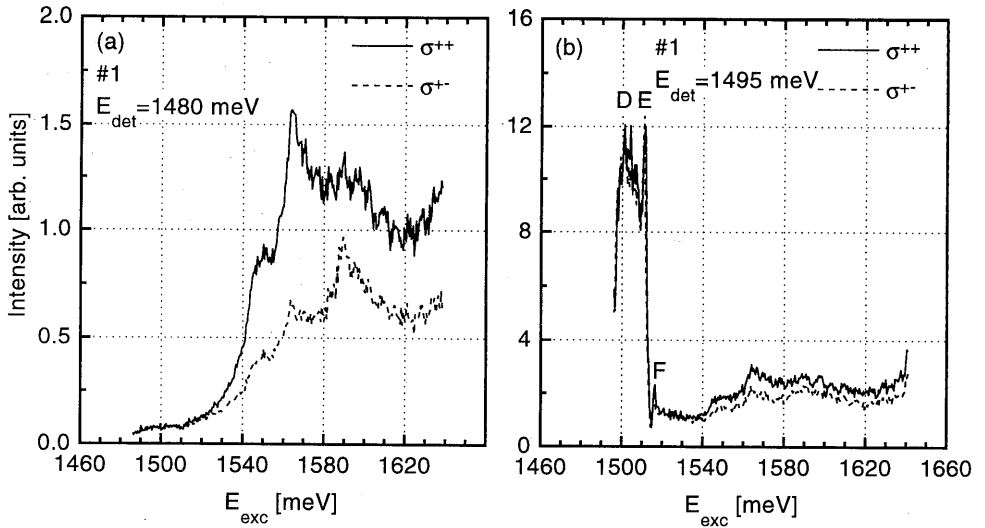


Fig. 7.3 Photo-luminescence excitation spectra of sample 1, detected at 1480 meV (a) and at 1495 meV (b). The solid and dashed lines are taken in parallel (σ^{++}) and cross (σ^+) polarization configuration, respectively. The identification of features D, E and F is discussed in the text. The units of the vertical axis of the (a) and (b) panels are identical.

7.3.1 Substrate-related PL(E)

Fig. 7.2 displays the polarized luminescence spectra of sample 1 ($w=150 \text{ \AA}$, $p=8 \cdot 10^{12} \text{ cm}^{-2}$), taken with the exciting laser at 1530 meV (a) and 1560 meV (b). Both spectra exhibit the features labeled A, B and C (at 1491, 1494 and 1513 meV, respectively), that, from their energetic position, can be identified as donor-acceptor (D,A), band-acceptor (e,A) and acceptor-bound exciton (A,X) recombinations in bulk GaAs, respectively. The identification of these features as being related to 3D (bulk) transitions in the substrate is confirmed by the following observations. First, as stated above, the lack of dependence on (2D) structural parameters. If one of the features were due to an enhancement of emission intensity at the Fermi level, or any other 2D-related transition, its position should definitely depend on the well width and doping concentration. Second, when exciting in the Moss-Burstein gap, i.e. at 1530 meV, see also Fig. 7.3, absorption in the 2D structure is forbidden due to the phase-space filling in the valence bands. No luminescence from the structure is therefore to be expected at this excitation energy. Third, the absence of polarization when the excitation is in the Moss-Burstein gap of the 2D structure is characteristic for 3D PL. When the PL signal of the wells is superimposed on the bulk lines, a polarized signal is to be expected, as is

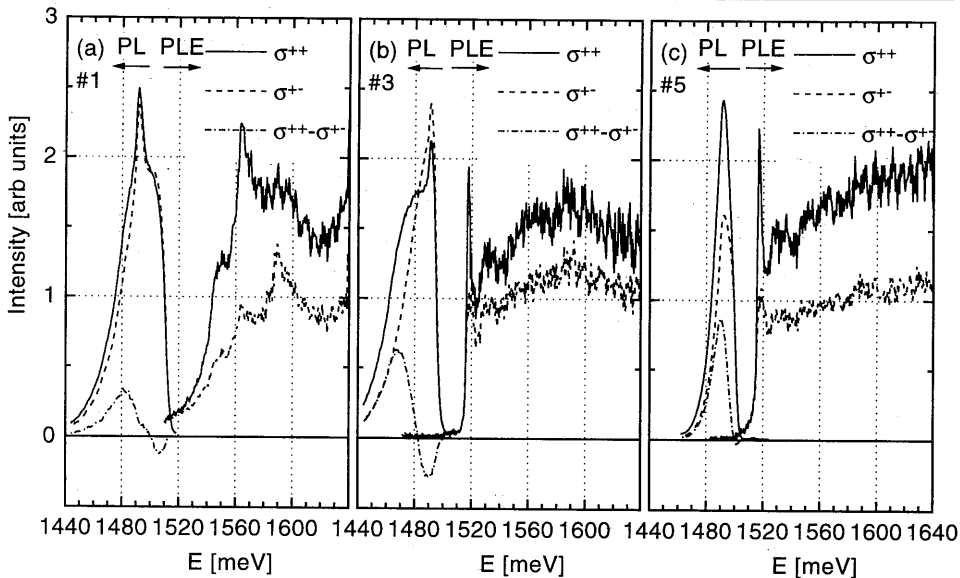


Fig. 7.4 PL and PLE spectra of samples 1 (a), 3 (b) and 5 (c). The PLE spectra are detected below the bulk PL signal. Solid and dashed lines denote σ^{++} and σ^{+-} polarizations, respectively. The dash-dotted line is the polarization curve, i.e. the difference between the polarized PL spectra.

shown in Fig. 7.2(b). Fourth, Ferreira *et al.* demonstrated that for 150 Å wells with doping concentrations above $p=6 \cdot 10^{11} \text{ cm}^{-2}$, the 3D and 2D PL signals start to overlap⁶.

The excitation spectra of sample 1, detected either near the maximum of the bulk luminescence (1495 meV) or below the bulk PL (1480 meV), are shown in Fig. 7.3 (a) and (b), respectively. Clearly, when the detection coincides with the bulk PL lines, three dominant lines are added to the excitation spectrum. The total disappearance of these lines when the detection is below the bulk PL indicates that, indeed, the emission-features A, B and C originate from a different region in the sample than the remainder of the luminescence. If this were not the case, carriers excited at any of the features D, E or F, should be able to recombine at energies below feature A, i.e. in the quantum well layers. Peaks E (1512 meV) and F (1516 meV) can now be identified as the absorption peaks of the acceptor bound and free excitons in bulk GaAs, respectively. The origin of structure D is not fully clear at present. From measurements with other detection energies we found that it is extended to, at least, 1485 meV, and that it is always of the same intensity as the E peak. It should be stressed that also the features D, E and F are equally present in all samples.

7.3.2 2D-related PL(E)

Polarization resolved PL and PLE spectra for samples 1, 3 and 5 are shown in Fig. 7.4 (a-c). The spectra of the other samples are fully consistent with the ones shown. The PL spectra are all taken using the Ti:Sapphire laser as excitation source. It is worthwhile to point out that none of the PL spectra showed significant changes when the wavelength of the exciting light was changed, nor when the He-Ne laser was used for excitation, apart from an obvious scaling of the PL spectrum. This is in marked contrast with the observations in Refs. 11,12 and 13 where the appearance of a FES in the PL spectrum of similar structures is reported, once the photon energy of the exciting laser is above the band gap of the confining barriers. In paragraph 7.5 we will come back to this point.

From a comparison of the PL spectra of Fig. 7.4 (a) and (b) it can be seen that the main effect of the increasing well width is a redshift of the 2D-related spectrum, being due to the decreased confinement energy of the groundstate electron level E0. As the lowest light and heavy hole levels (L0 and H0) are solely confined by the notch potential of the δ -doping layer, see Fig. 7.1, their confinement energy is not expected to change significantly with increasing well width. This is reflected by the almost constant separation between the H0-E0 and L0-E0 luminescence lines, assumed to equal the separation between the positive and negative extrema in the polarization curve (dotted line). For the same reason, also the width of the PL line, reflecting the separation between H0 and the Fermi energy E_F , remains constant with increasing well width. Obviously, this is not the case when, at constant well width, the carrier density is decreased, as shown in Figs. 7.4 (b) and (c). Here, the experiments indicate that the L0 subband is not significantly occupied, since the negative extremum in the polarization curve (σ^{++} - σ^+) has disappeared, in agreement with our calculations (we calculate E_F -L0=0.6 meV). The apparent blue shift with decreasing carrier density is due to the decreasing depth of the δ -potential and the reduction of the strength of the exchange-correlation potentials with decreasing doping concentration, again in accordance with the calculations depicted in Fig. 7.1.

The broad tail on the low-energy side of the PL spectra is assigned to transitions from background acceptor states to the lowest confined conduction band level¹⁷. Since the energy gap between the acceptor level and the E0 level is dependent on the position of the acceptor in the well, the length of the low-energy tail is expected to correlate with the depth of the δ -potential, i.e. with the doping concentration. Our measurements indeed show a monotonic increase of the tail length with increasing doping concentration, c.f. Fig. 7.4 (b) and (c). It is, however, extremely hard to quantify this effect, although the

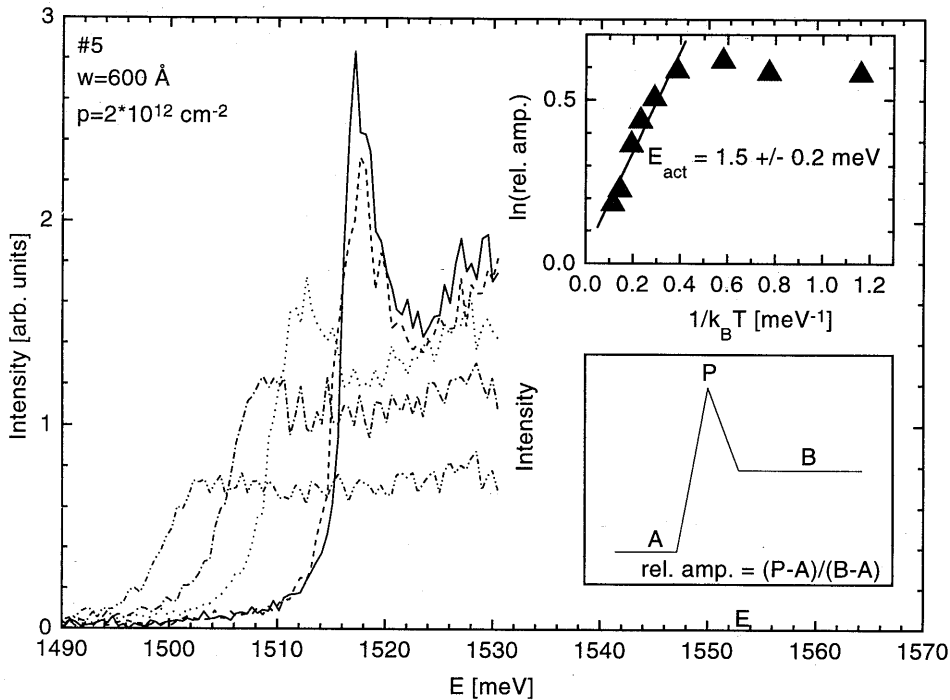


Fig. 7.5 (a) Main panel: The PLE onset of sample 5 in σ^{++} polarization at 20, 40, 60, 80 and 100 K. Upper insert: Activation plot of the normalized peak height. The activation energy of the exciton unbinding is 1.5 ± 0.2 meV. Lower insert: Schematic representation of the spectra plotted in the main panel and definition of the normalized peak height, used in the upper insert.

order of magnitude of the tail length compares favorably with the calculated potential profiles in Fig. 7.1.

The PLE spectra of our structures are hardly dependent on the doping concentration, as can be seen from a comparison of Figs. 7.4 (b) and (c). This can easily be understood by realizing that the PLE spectrum is determined by the higher, unoccupied, hole levels and the empty electron levels. Since these states 'feel' relatively little of the δ -potential, they are hardly affected by an increase in the doping concentration, which only changes the central region of the notch potential. Although the L0 level seems unoccupied at a doping level of 2×10^{12} cm $^{-2}$, L0-E0 is not observable in the PLE spectrum, due to either the small matrix element for L0-E0 transitions (from calculations, the step at 1517 meV is expected to be a factor of three higher than the L0-E0 absorption) or a small Moss-Burstein shift, resulting from a slight occupation of the L0 subband. Increasing, at constant doping concentration, the well width from 150 Å to

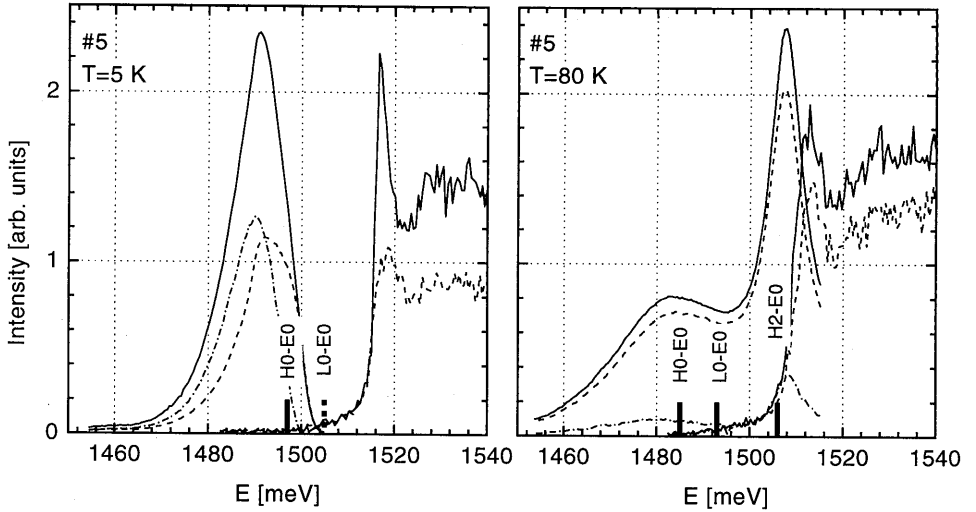


Fig. 7.6 PL spectra and PLE onsets at 5 K and 80 K for sample 5. Note the strong line in the 80 K PL spectrum associated with H2-E0 recombination, which is visible due to the thermal population of the H2 subband. The thick vertical lines are calculated PL energies, the meaning of all other lines is the same as in Fig. 7.4.

600 Å, the steps at 1545 and 1565 meV [Fig 7.4(a)] shift to lower energy, loose intensity and seem to merge at 1518 meV [Fig. 7.4(b)]. Since these steps are due to H2-E0 and H1-E1 absorption, respectively, this behavior can be understood from two points. Firstly, the obvious shifts of the hole and electrons with well-width, which causes a strong reduction of the separation between these transitions. Secondly, the increasing well width causes a dramatic reduction of the H1-E1 matrix element, effectively removing the H1-E1 absorption step from the PLE spectrum. The step at 1527 meV in Fig. 7.4(b) is assigned to H2-E2 absorption.

Apart from the 150 Å and 300 Å samples (no. 1 and 2), all samples show a sharp peak at the absorption onset. Based on its position and its small width (2.5 meV for sample 3), we assign this to a H2-E0 exciton. In order to validate this assignment, temperature dependent PLE measurements were performed, see Fig. 7.5. The upper insert shows the activation plot of the height¹⁸ of the excitonic PLE signal, normalized on the band-to-band PLE signal, as illustrated in the lower insert. The latter correction is needed to account for the temperature dependence of non-radiative losses, that affect the PLE signal strength. Clearly visible is the activated behavior, with an activation energy of 1.5 ± 0.2 meV. Taking the large density of mobile carriers that screen the Coulomb interaction into account, this value seems reasonable^{19,8}. In paragraph 7.5 this feature will

be discussed in more detail.

Further confirmation of the assignment of the peak at the absorption onset to an excitonic transition of an unoccupied subband comes from the temperature dependence of the PL signal, that is shown in Fig. 7.6. Clearly visible is, apart from the redshift due to the shrinkage of the band gap with temperature, the luminescence arising from one or more thermally occupied subbands. From our band structure calculations we find for the $H1-E_F$, $H2-E_F$ and $E0-E1$ separations respectively 9.7, 14.1 and 3.9 meV. Comparing this to $k_B T = 7$ meV at 80 K, the assignment of this line to either $H1-E1$ or $H2-E0$ recombination is possible, since they have calculated transition energies of 1517 and 1518 meV, respectively. Since the matrix element for the $H2-E0$ transition is a factor two larger than for the $H1-E1$ transition, the former transition is expected to dominate. The coincidence of the PL maximum with the half-height point of the peak at the PLE onset shows that both peaks share the same origin.

7.4 Numerical calculations

7.4.1 Model

The model used to obtain the self-consistent wave functions and confinement potentials of electrons and holes has been described in detail in an earlier publication²⁰, so only a brief outline will be given here. Additions that were made to the model described in Ref. 20, and that are essential for a proper calculation of the δ -potential solutions, will be discussed in more detail.

Hole wavefunctions and energies were obtained as numerically exact solutions of the 4*4 Luttinger Hamiltonian, including the valence band anisotropy. The used Luttinger parameters are $\gamma_1=6.85$, $\gamma_2=2.1$ and $\gamma_3=2.9$ for GaAs and $\gamma_1=3.45$, $\gamma_2=0.68$ and $\gamma_3=1.29$ for AlAs²¹, the used electron masses in GaAs and AlAs are $0.067 m_0$ and $0.15 m_0$. The parameters for $Al_xGa_{1-x}As$ were calculated using the virtual crystal approximation. The band gap of $Al_xGa_{1-x}As$ was calculated as $E_g(x)=1519.2+1360x+220x^2$ meV, where the common 40:60 rule was used for the distribution of the band gap discontinuity over the valence and conduction bands at the GaAs/ $Al_xGa_{1-x}As$ interfaces. The Hartree potential was calculated by solving the Poisson equation numerically. Only the ionized beryllium atoms and the occupied valence band states are contributing to this potential, for reasons explained in paragraph 7.2. The degree of ionization of the Be acceptors is assumed to be 100 percent²². The broadening

of the Be δ -layer is assumed to be rectangular, with a width of $25 \text{ \AA}^{12,23}$. For the present densities neither the exact broadening profile nor its width are of significant influence on the final solutions¹². In contrast to our experiences with barrier-doped p-type single and double QWs, it turned out that assuming parabolic valence bands in calculating the charge distribution gives erroneous results in these center- δ -doped wells. We therefore used the actual hole dispersions from the Luttinger Hamiltonian to calculate the Fermi level, and calculated the charge distribution by summing all (k-dependent) hole wavefunctions up to the Fermi level. The DOS was used as weight function in the latter procedure. In order to expedite the calculations, the axial approximation was applied in this part of the calculation. Absorption spectra are calculated as indicated in Ref. 19.

For the structural parameters needed in the self-consistent calculations, i.e. the well-width w and acceptor concentration p , the nominal values of the growth menu are taken. For the dopant concentration, the error made by this procedure can be estimated from the characterization data of the reference sample. This sample had a nominal Be concentration of $2 \cdot 10^{14} \text{ cm}^{-2}$ per μm GaAs, characterization with van de Pauw measurements showed an actual doping level between 2.0 and $1.95 \cdot 10^{14} \text{ cm}^{-2}$ per μm . The error in the subband calculations, caused by an error of this size in the dopant concentration, is fully negligible with respect to the experimental resolution. Deviations from the nominal value of the well width are usually a few percent. For 150 \AA wide wells this may cause measurable deviations in the calculations, for wider wells this will not be a problem. It is important to note that no adjustable fitting parameters have been used in our model.

7.4.2 Exchange and correlation

Inclusion of many-particle corrections in the subband calculations beyond the direct Coulomb interaction or Hartree term turned out to be essential. In recent literature, various attempts have been made to capture the complications arising from the coexistence of light and heavy holes in calculations of the BGR in p-type systems^{24,25,1}. Because of the high hole density and the occupation of multiple subbands, the present samples are extremely suited as a test system for various hole-BGR models. In this work, calculations based on the models proposed by Reboledo and Proetto (Ref. 24) and Bobbert *et al.* (Ref. 1) will be compared with calculations without exchange and correlation corrections, and with calculations based on the one-component plasma model of Hedin and Lundquist²⁶. The model proposed by Sipahi *et al.*²⁵ is only applicable to

homogeneous systems, and can therefore not be applied to the present samples. However, as far as $k=0$ energies are concerned, this model is similar to the one proposed by Reboredo and Proetto, in the sense that holes with $|m_j|=3/2$ and $|m_j|=1/2$ experience different exchange-correlation corrections. For details concerning the various BGR models, the reader is referred to the original publications. However, for the sake of self-containedness, the basic assumptions of the models by Hedin and Lundquist, Reboredo and Proetto and Bobbert *et al.* will be briefly outlined below.

All three models apply the Local Density Approximation (LDA) for extending results obtained for a homogeneous bulk system to a quasi-2D system, by calculating an effective exchange-correlation potential V_{xc} that only depends on the local carrier density, i.e. $V_{xc}(p(z))$. The Hedin and Lundquist model was originally derived for n-type systems. It therefore assumes that the carrier plasma consists of one type of (parabolic) carriers only. By applying this model directly to a hole gas, characterized by the effective heavy hole mass m_h^* , one indirectly assumes that all holes are heavy holes. The validity of this assumption is further discussed in paragraph 7.5. Although this assumption totally ignores the actual valence band structure, favorable comparisons with experiments have been reported for BGR calculations that treat the valence bands as a single, parabolic band^{27,28,29}. Since the Hedin/Lundquist model is only used for comparison with more sophisticated models, there is no particular reason for choosing this model instead of any other parametrized model available in the literature for calculating the BGR in n-type systems^{30,31}, apart from the fact that the Hedin/Lundquist model appears to be the most popular. The model proposed by Reboredo and Proetto²⁴ is based on an analogy with the spin-density functional formalism. The exchange-correlation potential is made dependent on $|m_j|$, $V_{xc}^{|m_j|}(p^{3/2}(z), p^{1/2}(z))$. By ignoring exchange and correlation between light holes and heavy holes, the final exchange-correlation potential becomes only dependent on the local density of particles with $|m_j|=3/2$ or $1/2$, $V_{xc}^{|m_j|}(p^{|m_j|}(z))$. The quantity $p^{|m_j|}(z)$ is defined as the density in the heavy ($|m_j|=3/2$) or light ($|m_j|=1/2$) hole subbands. For the functions $V_{xc}^{|m_j|}$ a parametrized expression, derived for a one-component plasma, is used, where the carrier mass is chosen equal to an effective heavy or light hole mass, depending on $|m_j|$. To summarize, the most important feature of this model is that heavy and light holes experience different exchange-correlation potentials. In paragraph 7.5.1 we will discuss the inconsistency and omissions of this model. The model derived by Bobbert *et al.* does not assign a particular character (heavy or light) or mass to individual subbands, as Ref. 24, or to particular spinor components, as Ref. 25, of the 2D structure. Rather, it is based on the notice that, within the LDA formalism, the quasi-2D structure *locally* is treated as *bulk* and that therefore the *bulk* dispersion relations must be used to

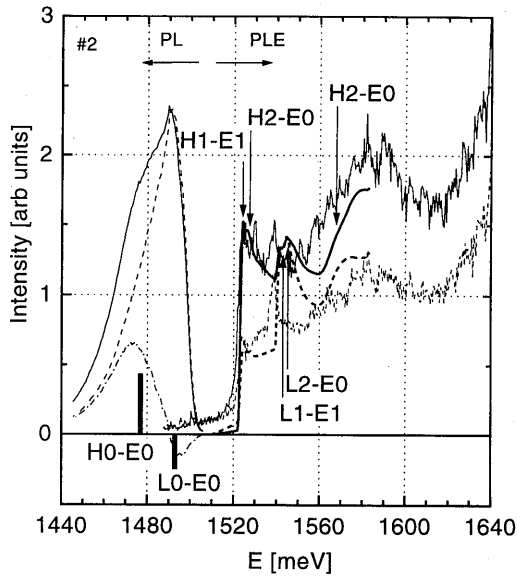


Fig. 7.7 Comparison between experimental and simulated PLE spectra of sample 2. The experimental PL spectrum can be compared with calculated transition energies for recombination at $k=0$ (thick vertical lines). Solid and dashed lines denote σ^{++} and σ^{+-} polarizations, respectively. The dash-dotted line is the difference between the polarized PL spectra. The thick, smooth lines are simulations, the thinner lines are experimental curves. The arrows identify the origin of features in the simulated PLE spectra.

shown are obtained using the model of Bobbert *et al.* for $V_{xc}(z)$.

To arrive at the total band gap renormalization, also the correlation of the photo-generated electron with the sea of holes must be taken into account. Independent of the model used for the hole exchange-correlation potential, we use the parametrized expression of Ref. 1 for the electron correlation potential $V_c(z)$, again using the LDA.

7.4.3 Numerical results

Because of the strong overlap of the electron and hole wave functions with the ionized acceptors, a relaxation of the k -selection rules could easily occur as a result of localization or strong scattering. Before a meaningful comparison of experiments and

determine the *local* amount of heavy and light holes. Based on this idea, Bobbert *et al.* calculate the exchange and correlation energy $\epsilon_{xc}(\rho)$ of a hole in a homogeneous hole gas of density ρ , where all heavy-light hole interactions, i.e. heavy-heavy, light-light and heavy-light hole exchange and correlation, are taken into account. Since the Coulomb interaction is non-diagonal with respect to hole character, it is fundamentally impossible to identify a single hole as 'light' or 'heavy'. The exchange-correlation energy is therefore identical for all holes in the system. Subsequently, $\epsilon_{xc}(\rho)$ is converted to the exchange-correlation potential, using $V_{xc}(z) = -\frac{d}{d\rho}[\rho\epsilon_{xc}(\rho)](z)$. Note that also $V_{xc}(z)$ is equal for 'heavy' and 'light' hole subbands. Unless stated otherwise, all calculations

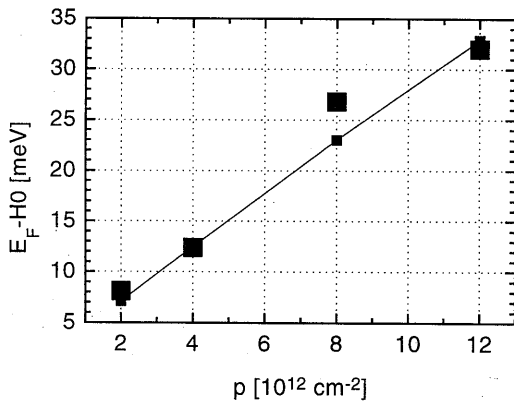


Fig. 7.8 Experimentally and numerically determined separation between the ground state heavy hole energy at $k=0$ and the Fermi energy versus doping concentration for $w=600 \text{ \AA}$. The large (small) squares denote experimental (numerical) points, the thin line connects the numerical points.

calculations can be performed, it is therefore essential to determine whether or not the measured optical transitions are direct in k -space. To do so, an experimental PL and PLE spectrum will be compared with numerical simulations, see Fig. 7.7. The numerical spectra (PLE) and energies (PL) are calculated with full k -conservation. The excellent agreement between measured and calculated PLE spectra, both in position and steepness of onsets, shows that the relaxation of k -conservation selection rules indeed is negligible, as far as absorption is concerned. In emission this is

definitely not the case, which is illustrated in Fig. 7.8, where the experimental and calculated $H0-E_F$ separations are plotted versus carrier density. Experimentally, the $H0-E_F$ separation is determined by taking the energy at the maximum in the polarization curve as the transition energy associated with $H0(k=0)$ to $E0(k=0)$ recombination, and the half-maximum point at the high-energy side of the emission spectrum as due to $H0(k=k_F)$ or $L0(k=k_F)$ to $E0(k=0)$ recombination. The very favorable comparison with calculated values shows that this assignment is correct, and that transitions in emission can either be direct or indirect in k . However, the maximum emission intensity still seems to arise from direct transitions, and positive and negative extrema in the polarization curve will in the following be assumed to indicate $H0(k=0)$ to $E0(k=0)$ and $L0(k=0)$ to $E0(k=0)$ transitions, respectively. It is worthwhile to point out that the onset of absorption does not correspond to $H0(k=k_F)$ or $L0(k=k_F)$ to $E0(k=k_F)$ transitions, as in most modulation-doped heterostructures, but to $H1-E1$ or $H2-E0$ transitions at the zone center. This is due to the large hole densities in the present samples, which cause extremely large Moss-Burstein shifts.

As a typical example, Fig. 7.9 shows the dispersion relation for the same sample as shown in Fig. 7.7 (no. 2), together with the calculated Fermi energy E_F . The well-known non-parabolicity of the valence band states is apparently visible.

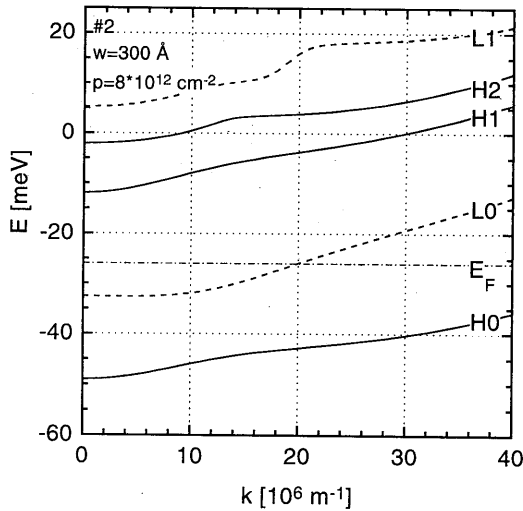


Fig. 7.9 Dispersion relations of the lowest subbands of sample 2. The solid and dashed lines denote heavy and light hole dispersions, respectively. The dash-dotted line indicates the Fermi level E_F .

However, extreme non-parabolicities as negative masses, that are generally found for the L0 band in heterostructures based on the $\text{Al}_x\text{Ga}_{1-x}\text{As}$ system¹⁹, are absent. Nevertheless, the remaining non-parabolicities still strongly affect the optical spectra, which is manifested mainly in the non-step like behavior of the absorption spectra, see Fig. 7.7.

The summary of our experimental and numerical data is shown in Figs. 7.10 and 7.11, where measured and calculated transition energies are plotted versus the well width (Fig. 7.10) and the dopant concentration (Fig. 7.11). Comparing the measured energies with the ones calculated without exchange and correlation corrections directly shows the need for these corrections, in contrast with the claim in Ref. 12. Furthermore, it shows that in these δ -doping layers the BGR can not be accounted for by a rigid shift of all valence bands, like in, for instance, single quantum wells. Clear differences can also be found between the results obtained with the BGR models by Bobbert *et al.* and by Reboredo and Proetto, that both aim to account for the coexistence of light and heavy holes. These differences are most pronounced in the light hole subbands, particularly at low doping concentrations and narrow well widths, c.f. the upper-right and lower-left panels of Figs. 7.10 and 7.11. Both the energies of the L0-E0 and L1-E1 transitions calculated with the Reboredo-Proetto model are far more than the experimental error of about 2 meV above the experimentally found values. Moreover, the Reboredo-Proetto model incorrectly predicts one occupied subband for a hole density of $p=4*10^{12} \text{ cm}^{-2}$. A surprisingly good correspondence with experimental data is found when the one-particle model of Hedin and Lundquist is used in the calculations. Comparing with the model by Bobbert *et al.* with 'fitting to the experimental data' as criterium for success, the Bobbert-model seems to prevail for all samples, except those with the lowest density and most narrow well width, for which the Hedin-Lundquist model seems to prevail. The differences are however quite small. On physical grounds,

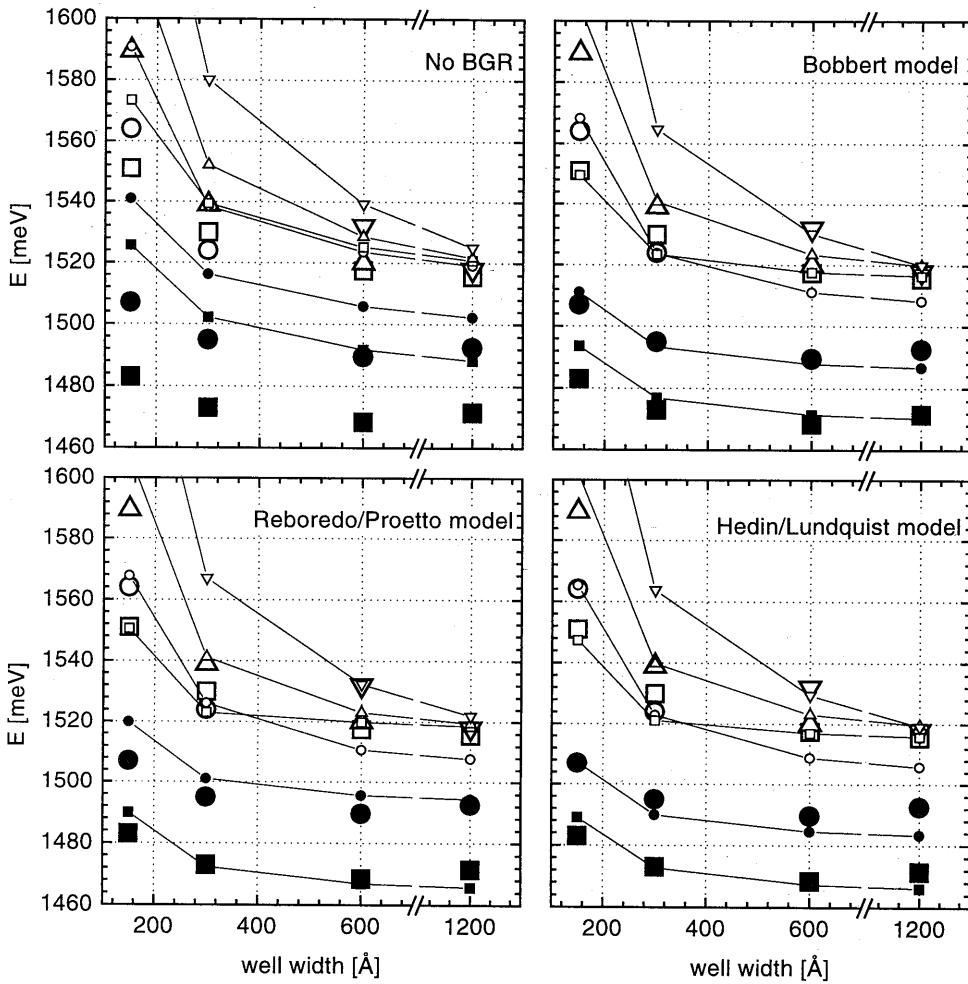


Fig. 7.10 Measured and calculated transition energies, using various models for the hole exchange and correlation interactions, versus the well width. The large symbols denote experimental points, the small symbols denote calculations. The lines connect the calculated energies. The experimental error is usually less than 2 meV. The meaning of the symbols is as follows: solid squares: H0-E0; solid circles: L0-E0; open squares: H2-E0; open circles: H1-E1; open up triangle: L1-E1; open down triangle: H2-E2.

the success of the model by Hedin and Lundquist for p-type systems is accidental and based on a cancellation of errors¹, to which we will come back in the next section.

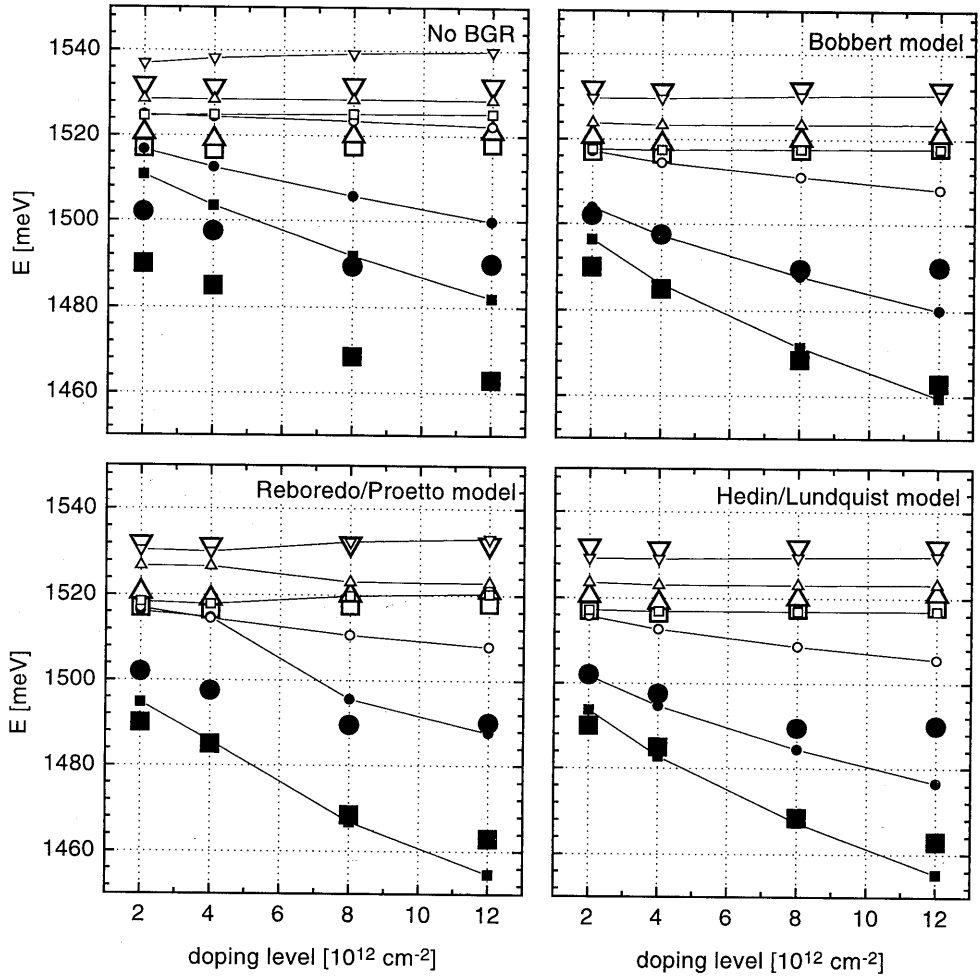


Fig. 7.11 As Fig. 7.10, but as a function of the total dopant concentration.

7.5 Discussion

7.5.1 Exchange and correlation

In the previous section we have shown that the BGR model by Reboredo and Proetto systematically underestimates the renormalization of the light hole-related transitions. These deviations are directly due to the fact that this model uses different exchange-correlation potentials for heavy and light holes, and that these potentials are

only a function of the local density in the heavy *or* light hole subbands. The analogy with the spin-density functional formalism, on which this model is based, is tempting but invalid. The local 'heavy' and 'light' hole densities, obtained by Reboredo and Proetto from the envelope functions of the $|m_j|=3/2$ and $|m_j|=1/2$ spinor components, are easily shown to be dependent on the direction of the quantization axis, which, of course, should not be the case. Furthermore, the exchange and correlation interactions between 'light' and 'heavy' holes are, by definition, ignored in this model. Even in the hypothetical case of an infinitesimally small light hole mass, when no states with $|m_j|=1/2$ are occupied, these interactions can not be ignored due to the non-diagonal character of the Coulomb interaction with respect to the hole character¹.

The surprisingly good correspondence between experimentally determined energies, and those calculated with the Hedin-Lundquist model for exchange and correlation is, as stated above, due to a cancellation of errors. To be more precise, the implicit assumption that all holes are 'heavy', made by applying an 'electron gas' model to a hole gas, leads to an overestimation of the exchange energy and an underestimation of the correlation energy. The qualitative reason why the exchange energy for the hole gas is smaller in magnitude than that for the electron gas is the fact that, besides the spatial degrees of freedom, there are four instead of two internal degrees of freedom ($m_j=\pm 3/2, \pm 1/2$ for a hole gas, and only $m_j=\pm 1/2$ for an electron gas). Consequently, it is easier to fulfil the Pauli exclusion principle, which reduces the exchange interaction. The underestimation of the hole correlation energy, when applying the Hedin/Lundquist model to a hole gas is also related to the number of internal degrees of freedom. Due to the coexistence of light and heavy holes, the number of possible excitations at the Fermi level is increased, leading to a higher dielectric constant for a hole gas than for an electron gas of the same density. A high dielectric constant means that the system reacts efficiently on a perturbation (strong screening), which implies a strong correlation with the perturbation. In this specific case the perturbation is just the Coulomb potential of any hole in the system. Therefore, the correlation energy of a system with four internal degrees of freedom is higher than that of system with two internal degrees of freedom.

The only method of defining local heavy and light hole fractions that is consistent with the LDA formalism is employed in the model by Bobbert *et al.* It states that, since LDA treats the quasi-2D charge distribution locally as a bulk density, also the bulk dispersion relations have to be used in determining the local heavy and light hole fractions. The success of the Bobbert model for the present samples therefore mainly shows the validity of the local density approximation in the calculation of the effects of hole exchange and correlation in quasi-2D systems of high degeneracy.

7.5.2 Exciton screening

The observation of strong excitonic features in the present, highly degenerate samples may appear surprising at first sight. Although it is well known that the efficiency of Coulomb screening in 2D systems is strongly reduced as compared to that in 3D systems, straightforward extrapolation of available theoretical suggests that only an infinitesimally small binding energy should remain^{32,33}. However, as was pointed out in a few earlier publications^{34,8,9}, standard 2D screening theory ignores the differences in probability distributions of various subbands along the growth direction. To be more specific, the relatively strong confinement of the occupied groundstates (H0 and L0), leads to a poor screening of excitons formed by more extended states like H2 and E0^{34,8,9}. Furthermore, it has been suggested⁶ that the presence of ionized impurities inside the quantum well makes the screening of excitons less efficient, which will facilitate the survival of excitons up to the current doping concentrations. The overlap argument is in full agreement with the observation that no significant excitonic absorption enhancement is visible for the 150 and 300 Å wells. Due to the confinement by the Al_{0.20}Ga_{0.80}As barriers, the extension of the H2 and E0 wave functions along the growth direction is not much larger than that of the H0 and L0 wave functions, causing a relatively efficient screening of the H2-E0 exciton.

There are two points that we would like to stress, concerning the screening of excitons in these samples. The first is that it has been shown that peaked structures in absorption spectra are generally spoken an unreliable indicator for the presence or absence of excitons^{19,8}. See e.g. the peaks at 1540 and 1565 meV in the PLE spectra of the 300 and 150 Å wells, respectively [Figs. 7.7 and 7.4(a)], that can fully be accounted for by the valence bandstructure only. The absence of a peak in the absorption spectrum, on the other hand, does not imply the total bleaching of the exciton⁸. The second point, that is strongly related to this, is that we do not claim that all excitons, excepte the H2-E0 exciton, are unbound. The apparent dominance of the H2-E0 exciton in the spectra of wide wells is due to the subtle interplay between the exciton binding strength and the optical matrix element. The latter is extremely large for the H2-E0 transition in wide wells, as can directly be concluded from a comparison of the strengths of the H0-E0 and H2-E0 PL lines at 80 K, see Fig 7.6. As an example, the H1-E1 subbands are also expected to form an exciton of significant binding energy for wide wells ($w \geq 600$ Å), but at these well widths, the optical matrix element of H1-E1 transitions is much smaller than that of the H2-E0 exciton, which prevents the exciton from being identifiable in PLE.

7.5.3 The absence of a Fermi-edge singularity

In contrast to what is reported by Wagner and Richards^{11,12,13} for samples that are very similar to the ones discussed here, we do not find any indication for a Fermi-edge singularity in the PL spectra of our samples. It has been shown that such a FES can arise from either strong localization of the minority carriers^{7,15,35,36,37,38} or a near-resonance condition between states at the Fermi level and those of a nearby excitonic level^{3,4,39,40,41}. Due to the small electron mass in GaAs, the former condition is not very likely to be fulfilled, as was also noticed in Ref. 12. Furthermore, the small effective mass of the unlocalized electron will inhibit the observation of any FES-like features in emission spectra, due to the large recoil of the scattered electron^{4,14,15}. The latter condition requires an excitonic level which is almost at resonance with the Fermi level. For all samples but the one with $p=2 \cdot 10^{12} \text{ cm}^{-2}$ the separation between E_F and the lowest occupied hole level is at least 13 meV, which seems to far for causing any significant coupling^{39,40,42}. Moreover, it was shown by Rodriguez and Tejedor⁴ that no such coupling at all can occur in symmetric potentials. Summarizing the above, the absence of a FES in the PL spectra of our samples appears to be in good agreement with most earlier work on the FES in emission spectra.

There are two significant differences between the present samples and the ones used by Wagner and Richards. The first is the density range, which runs from $3 \cdot 10^{12}$ to $4 \cdot 10^{13} \text{ cm}^{-2}$ in Refs 12 and 13. However, the separations between E_F and the lowest unoccupied subband reported for these samples are of the same size as in our samples. The second, and probably most significant, difference concerns the fact that Wagner and Richards employ samples with a single δ -doped well. As was pointed out by Wagner¹³, this might easily lead to a breaking of the symmetry of the confining potential, which can strongly enhance the formation of a FES⁴.

It is interesting to mention the observation of a FES in a highly disordered system of Be δ -doped bulk GaAs by Fritze *et al.*⁷. In these samples, the extremely high Be coverage in the δ -layer (up to 0.35 monolayer (ML) or $p=2.1 \cdot 10^{14} \text{ cm}^{-2}$) caused the formation of Be clusters. The resulting high disorder leads to the localization of the minority carriers (electrons), despite their low effective mass. The Be coverages used in our samples, maximally 0.02 ML, are far below the density at which the so-called surface phase transition occurs, and Be clusters start to form.

7.6 Conclusions

Summarizing, we have studied many-body interactions in Be- δ -doped quantum wells, by means of a careful comparison between PL(E) experiments and self-consistent field calculations. Different LDA-models for the exchange and correlation potentials of an interacting hole gas have been compared with experiments. It is found that the model that was recently derived by Bobbert *et al.*¹ consistently describes the experimental band gap renormalization, both for empty and filled subbands. Furthermore, our results indicate that 'heavy' and 'light' hole subbands experience the same exchange-correlation potential, which is consistent with the assumptions of the LDA formalism. For well widths above 600 Å a sharp peak dominates the absorption spectra of our samples, which is attributed to a H2-E0 exciton. The dominance of this exciton is explained in terms of a strong optical matrix element and a reduced screening efficiency of higher subbands, due to a small overlap with the screening particles. In contrast to earlier work on similar samples, no indication for a Fermi-edge singularity in PL was found, which is discussed and understood in the framework of other theoretical and experimental work on this singularity.

References

1. P. A. Bobbert, H. Wieldraaijer, R. van der Weide, M. Kemerink, P. M. Koenraad, and J. H. Wolter, *Phys. Rev. B* **56**, 3664 (1997).
2. S. A. Brown, J. F. Young, Z. Wasilewski, and P. T. Coleridge, *Phys. Rev. B* **56**, 3937 (1997).
3. S. J. Xu, S. J. Chua, X. H. Tang, and X. H. Zhang, *Phys. Rev. B* **54**, 17701 (1996).
4. F. J. Rodriguez and C. Tejedor, *J. Phys.: Condens. Matter* **8**, 1713 (1996).
5. I. A. Buyanova, W. M. Chen, A. Henry, W.-X Ni, G. V. Hansson, and B. Monemar, *Phys. Rev. B* **53**, 1701 (1996).
6. A. C. Ferreira, P. O. Holz, B. E. Sernelius, I. Buyanova, B. Monemar, O. Mauritz, U. Ekenberg, M. Sundaram, K. Campman, J. L. Merz, and A. C. Gossard, *Phys. Rev. B* **54**, 16989 (1996).
7. M. Fritze, A. Kastalsky, J. E. Cunningham, W. H. Know, R. N. Pathak, and I. E. Perakis, *Solid State Commun.* **100**, 497 (1996).
8. M. Kemerink, P. M. Koenraad, P. C. M. Christianen, R. van Schaijk, J. C. Maan, and J. H. Wolter, *Phys. Rev. B* **56**, 4853 (1997).
9. M. Kemerink, P. M. Koenraad, A. Parlangeli, P. C. M. Christianen, R. van Schaijk, J. C. Maan, and J. H. Wolter, accepted for publication in *Phys. Stat. Sol. (a)* **164** (1997).
10. M. Kemerink, P. M. Koenraad, and J. H. Wolter, unpublished.
11. J. Wagner, A. Ruiz, and K. Ploog, *Phys. Rev. B* **43**, 12134 (1991).
12. D. Richards, J. Wagner, H. Schneider, G. Hendorfer, M. Maier, A. Fischer, and K. Ploog, *Phys. Rev. B* **47**, 9629 (1993).
13. J. Wagner, D. Richards, H. Schneider, A. Fischer, and K. Ploog, *Sol. State El.* **37**, 871 (1994).
14. P. Hawrylak, *Phys. Rev. B* **44**, 3821 (1991).
15. A. E. Ruckenstein and S. Schmitt-Rink, *Phys. Rev. B* **35**, 7551 (1987).

16. Using the formula for the electrostatic potential of a charged plate $V = ped/2\epsilon_0\epsilon_r$, with d the separation between the topmost delta layer and the surface (600 Å), we find that $1.8 \cdot 10^{12} \text{ cm}^{-2}$ holes have to be transferred to surface states to overcome the mid-gap pinning of the Fermi level at the surface. So, even at the lowest doping concentration, the doping in the first delta layer is enough to accomplish this.
17. M.-L. Ke, L. S. Rimmer, B. Hamilton, J. H. Evans, M. Missous, K. E. Singer, and P. Zalm, *Phys. Rev. B* **45**, 14114 (1992).
18. In fact, one should measure the integrated excitonic intensity. However, a large degree of arbitrariness exists in separating the excitonic and free-particle contributions to the total PLE spectrum, which makes a quantitative analysis along this line impossible. The followed method does not suffer from this problem.
19. M. Kemerink, P. M. Koenraad, and J. H. Wolter, *Phys. Rev. B* **54**, 10644 (1996).
20. M. Kemerink, P. M. Koenraad, P. C. M. Christianen, A. K. Geim, J. C. Maan, J. H. Wolter, and M. Henini, *Phys. Rev. B* **53**, 10000 (1996).
21. *Physics of Group IV Elements and III-V Compounds*, edited by O. Madelung, M. Schultz, and H. Weiss, Landolt-Börnstein, New Series, Group III, Vol. 17, Pt. a (Springer-Verlag, Berlin, 1982); *ibid.*, Vol. 22, Pt. a (Springer-Verlag, Berlin, 1987).
22. E. F. Schubert, J. M. Kuo, R. F. Kopf, H. S. Luftman, L. C. Hopkins, and N. J. Sauer, *J. Appl. Phys.* **67**, 1969 (1990).
23. P. M. Koenraad, M. B. Johnson, H. W. M. Salemink, W. C. van der Vleuten, and J. H. Wolter, *Mat. Science and Engineering B* **35** 485 (1995).
24. F. A. Reborado and C. R. Proetto, *Phys. Rev. B* **47**, 4655 (1993).
25. G. M. Sipahi, R. Enderlein, L. M. R. Scolfaro, and J. R. Leite, *Phys. Rev. B* **53**, 9930 (1996).
26. L. Hedin and B. I. Lundqvist, *J. Phys. C: Solid St. Phys.* **4**, 2064 (1971).
27. G. Tränkle, H. Leier, A. Forchel, H. Haug, C. Ell, and G. Weimann, *Phys. Rev. Lett.* **58**, 419 (1987).
28. S. Haacke, R. Zimmermann, D. Bimberg, H. Kal, D. E. Mars, and J. N. Miller, *Phys. Rev. B* **45**, 1736 (1992).
29. S. Das Sarma, R. Jalabert, and S.-R. E. Yang, *Phys. Rev. B* **41**, 8288 (1990).

30. O. Gunnarsson and B. I. Lundqvist, Phys. Rev. B **13**, 4274 (1976).
31. J. P. Pedrew and A. Zunger, Phys. Rev. B **23**, 5048 (1982).
32. G. D. Sanders and Y.-C Chang, Phys. Rev. B **35**, 1300 (1987).
33. D. A. Kleinman, Phys. Rev. B **32**, 3766 (1985).
34. A. B. Henriques, Phys. Rev. B **44**, 3340 (1991).
35. Y. H. Zhang, N. N. Ledentsov, and K. Ploog, Phys. Rev. B **44**, 1399 (1991).
36. M. S. Skolnick, J. M. Rorison, K. J. Nash, D. J. Mowbray, P. R. Tapster, S. J. Bass, and A. D. Pitt, Phys. Rev. Lett. **58**, 2130 (1987).
37. G. Livescu, D. A. B. Miller, D. S. Chemla, M. Ramaswamy, T. Y. Chang, N. Sauer, A. C. Gossard, and J. H. English, IEEE J. Quantum Electron. **QE-24**, 1677 (1988).
38. S. Schmitt-Rink, C. Ell, and H. Haug, Phys. Rev. B **33**, 1183 (1986).
39. W. Chen, M. Fritze, W. Walecki, A. V. Nurmikko, D. Ackley, J. M. Hong, and L. L. Chang, Phys. Rev. B **45**, 8464 (1992).
40. M. Fritze, W. Chen, A. V. Nurmikko, J. Jo, M. Santos, and Shayegan, Phys. Rev. B **45**, 8408 (1992).
41. J. F. Mueller, Phys. Rev. B **42**, 11189 (1990).
42. P. Hawrylak, Phys. Rev. B **44**, 6262 (1991).

Summary

In contrast to the conduction bands, the theoretical description of the valence bands of III/V semiconductors is rather complicated. This is due to the coexistence of three 'types' of holes, which interact with each other: the heavy and light hole bands, and the spin-orbit split-off band. In (quasi) two-dimensional structures this interaction generally leads to highly non-parabolic and anisotropic valence band dispersion relations. It has been the predominant aim of this Ph.D. work to relate numerically calculated valence band structures to experimental observations.

The inclusion of valence band coupling in the calculation of many-body effects like screening, exchange, correlation and Fermi edge singularities is usually very cumbersome, and can easily obscure the underlying physical phenomena. Mainly for these reasons, most calculations of many-body effects have discussed systems in which the carriers are characterized by a parabolic dispersion, i.e. the carriers are assumed to be electron-like. In regarding holes as 'complicated electrons', it is often tacitly assumed that the description of effects that have been observed and understood for electrons, can straightforwardly be transferred to holes. In this thesis we examine in detail many-particle effects in hole-systems. Without exception, it turns out that a proper interpretation of our experiments requires more than a simple replacement of electrons by holes in the usual interpretation for electron-systems.

During the project, we employed both optical and electrical experimental techniques. The vast majority of our experiments is performed in the temperature range from 100 mK to 4.2 K. We used (magneto) Photo-Luminescence (PL) and -Excitation (PLE) spectroscopy, Shubnikov-de Haas (SdH) and Hall measurements. All investigated samples were grown in-house by MBE and consisted of $\text{Al}_x\text{Ga}_{1-x}\text{As}/\text{In}_y\text{Ga}_{1-y}\text{As}$ heterostructures, grown on GaAs (100) substrates.

Using the asymmetry of two coupled quantum wells of different width, in combination with the coupling between heavy and light holes, it is possible to generate a macroscopic separation between holes of opposite 'spin' (m_j). This effect was coined spin-dependent hole delocalization. Further theoretical study revealed that band bending, resulting from the presence of free holes and ionized acceptors, can greatly enhance this effect. This is the subject of chapter 3.

The aforementioned heavy-light hole coupling leads to a negative effective mass of the lowest light hole subband in many of $\text{GaAs}/\text{Al}_x\text{Ga}_{1-x}\text{As}$ heterostructures. Since the absolute value of this mass almost equals the mass of the electron, a singularity arises in

the joint density of states. In chapter 4 we show experimentally, numerically and analytically that this second-order van Hove singularity can be observed in the PLE spectrum of a 90 Å, p-doped GaAs/Al_xGa_{1-x}As quantum well. In earlier experimental work, this peak has also been observed, but was incorrectly interpreted as an excitonic feature.

The coexistence of a heavy and a light hole groundstate allows one to separate experimentally the contributions to the unbinding of excitons of Coulomb screening on the one hand, and Pauli principle-related screening on the other. This subject is discussed in chapter 5. A prerequisite is that the doping used is p-type, and that either the light or the heavy hole groundstate is unoccupied. A detailed analysis of magneto-PLE spectra then shows that the RPA approach, in which the Coulomb screening of excitons is usually calculated, fails for excited subbands. The reason for this failure is that the RPA approach neglects differences in spatial extent of particles in various subbands.

In chapter 6 a detailed comparison between magneto-transport (SdH) experiments and model calculations is presented. It is shown that, for all magnetic fields, Shubnikov-de Haas spectra of p-type heterostructures are very strongly affected by exchange interactions between holes in various Landau levels. This is in contrast with n-type systems where these interactions are only important in the high-magnetic field regime. As a consequence, the effective hole masses that are extracted from the temperature dependence of SdH oscillations are to be treated with extreme care and can often be regarded as meaningless.

Quantum wells with a beryllium delta-doping in the middle of the well are extremely suited to study exchange and correlation effects or, equivalently, band gap renormalization (BGR). This is due to the high hole densities that can be achieved in this way. In chapter 7 we compare experimentally determined PLE transition energies with the results of self-consistent field calculations, in which the BGR was calculated along the lines of various models available in the literature. We conclude that the model which was recently developed by Bobbert *et al.* is the only model that consistently describes the experiments.

Samenvatting

Met moderne technieken is het mogelijk om halfgeleidermaterialen atoomlaag voor atoomlaag te 'groeien', waarbij de samenstelling per atoomlaag gevarieerd kan worden. Door gebruik te maken van het feit dat vrije ladingdragers, elektronen of gaten, zich liever in het ene materiaal dan in het andere bevinden, is het mogelijk deze ladingdragers op te sluiten in een extreem dunne laag halfgeleidermateriaal. Door bijvoorbeeld een dunne (± 10 nm) laag galliumarsenide (GaAs) tussen twee dikke aluminium-galliumarsenide ($\text{Al}_x\text{Ga}_{1-x}\text{As}$) lagen te groeien, ontstaat een structuur waarin vrije lading opgesloten wordt in de GaAs laag. Omdat deze lading nog maar in twee richtingen vrij kan bewegen worden dergelijke structuren (quasi) twee-dimensionaal (2D) genoemd.

Het is algemeen bekend dat elektronen de stroom voerende deeltjes zijn in geleidende materialen. Hoe dit te rijmen is met de 'gaten' in bepaalde halfgeleiders zal aan de hand van onderstaande vergelijking geïllustreerd worden. Stel een halfgeleider voor als twee boven elkaar liggende, bijna oneindig grote, damborden, waarbij op elk vakje maximaal één steen (elektron) mag liggen. Het bovenste bord noemen we de conductie- of elektronenband, de onderste de valentie- of gatenband. In een volkomen zuivere, ofwel intrinsieke halfgeleider is elk vakje op het onderste bord bezet met een steen, en is het hele bovenste bord leeg. Wanneer we nu stroom willen sturen door deze halfgeleider (stenen willen verplaatsen), hebben we een probleem: in de conductieband zijn geen elektronen (stenen) om te verplaatsen, en in de valentieband kunnen we geen elektron verplaatsen omdat elk vakje al bezet is. Het systeem is dus isolerend. Wanneer we echter één, of een aantal elektronen in de conductieband brengen, is er wel geleiding mogelijk. Een dergelijke halfgeleider is van het n-type. Ook wanneer elektronen verwijderd worden uit de valentieband is geleiding mogelijk in de zo ontstane p-type halfgeleider. De wiskundige beschrijving van geleiding in een n-type halfgeleider is relatief simpel omdat alleen het gedrag van de paar extra elektronen in de conductieband beschreven hoeft te worden. Het bijhouden van het gedrag van alle elektronen bij geleiding in de valentieband is echter een exercitie van gigantische omvang. Het dambord is immers vrijwel oneindig groot en bijna alle vakjes zijn bezet. Veel efficiënter is het om niet alle aanwezige maar de paar *afwezige* elektronen te beschrijven. Door zo'n afwezig elektron een gat te noemen en *te doen alsof* het een gewoon deeltje is, ontstaat een situatie die wiskundig precies gelijk is aan de situatie in een n-type halfgeleider: een paar deeltjes op een voor de rest leeg dambord. Wanneer, onder invloed van een

elektrisch veld, een elektron in de valentieband naar links beweegt, beweegt het gat naar rechts. Het quasi-deeltje 'gat' heeft dus een lading die tegengesteld is aan die van het elektron, namelijk positief.

De oorsprong van de extra elektronen of gaten in n- of p-type halfgeleiders verdient nog enige uitleg. Bepaalde atomen hebben, wanneer ze in het kristalrooster van de halfgeleider zijn ingebouwd, een elektron 'te veel', in het geval van een donor, of een elektron 'te weinig', in het geval van een acceptor. De in een halfgeleider aanwezige donoren en acceptoren worden samen de dotering genoemd. Het extra elektron van een donor, meestal Si in GaAs komt terecht in de geleidingsband, aangezien de valentieband al helemaal vol zit. Op deze wijze ontstaat een n-type materiaal. Door opname van een elektron uit de valentieband door een acceptoratom, meestal beryllium (Be) in GaAs, wordt een gat gevormd in de valentieband en ontstaat een p-type materiaal. Een andere manier om elektronen en gaten te vormen in een intrinsieke halfgeleider is het zogenaamde fotoexcitatie of -absorptie proces, waarbij een halfgeleider met licht van een bepaalde golflengte bestraald wordt. Als de energie van het inkomende licht groter is dan de afstand tussen valentie- en conductieband, kan een lichtdeeltje geabsorbeerd worden door een elektron van de valentieband naar de geleidingsband te verplaatsen (exciteren). Hierbij worden dus gelijktijdig een vrij elektron en een vrij gat gecreëerd. Als dit elektron terugvalt naar de valentieband, het recombinatie- of emissieproces, komt weer licht vrij, met een energie die precies overeenkomt met de afstand tussen de valentie- en conductieband.

Als de zojuist geïntroduceerde gaten zich in een twee-dimensionale structuur net zo simpel zouden gedragen als biljartballen op een biljarttafel, in feite ook een 2D systeem, was dit proefschrift niet geschreven. Biljartballen, en elektronen, hebben de eigenschap dat als hun snelheid v , of eigenlijk hun impuls $p=mv$, verdubbeld wordt, hun kinetische energie E vier keer zo groot wordt, overeenkomstig de bekende formule $E=\frac{1}{2}mv^2$ of $E=\frac{1}{2}p^2/m$. Voor gaten is het verband tussen energie en impuls, de zogenaamde dispersierelatie, niet zuiver kwadratisch. Deze afwijking van een parabolische dispersierelatie wordt in de regel geïnterpreteerd in termen van een gaten-massa die afhankelijk is van de impuls! De berekening van deze gaten-dispersierelaties is tamelijk gecompliceerd, en het relateren van deze dispersierelaties aan experimentele resultaten is verre van triviaal. Dit laatste was een van de hoofddoelen van dit promotieonderzoek.

In het bovenstaande is alleen gesproken over afzonderlijke deeltjes, die geen wisselwerking met elkaar hebben. Deze een-deeltjes benadering is in veel gevallen niet correct omdat geladen deeltjes elkaar in de regel wel degelijk voelen. De eenvoudigste

uitbreiding van dit model is de interactie tussen een elektron en een gat, een twee-deeltjes interactie. Een vrij elektron en een vrij gat trekken elkaar aan, en kunnen zodoende een exciton vormen. Dit is een waterstof-achtige verbinding, waarbij de plaats van de positieve waterstofkern is ingenomen door het eveneens positieve gat, waar, klassiek gezien, het negatieve elektron omheen cirkelt.

Wanneer een exciton in een omgeving geplaatst wordt waarin zich zeer veel vrije gaten (of elektronen) bevinden, zal het met toenemende gaten- of elektronendichtheid ontbinden. Voor een exciton in een omgeving met veel vrije gaten, dus in een p-type halfgeleider, is dit als volgt te begrijpen. Een exciton kan bestaan, zoals gezegd, doordat een elektron aangetrokken wordt door het elektrisch veld van een gat. Andere gaten voelen dit veld echter ook, maar dan als afstotend, want gelijke ladingen stoten elkaar af. Hierdoor zullen de vrije gaten zich herrangschikken, en wel zodanig dat het veld van het gat dat het exciton vormt zo goed mogelijk afgeschermd wordt. Het elektron voelt nu slechts het afgeschermd veld, en wordt dus minder sterk gebonden. Dit ontbindings- of afschermingsproces wordt aangeduid als exciton-screening of -bleaching, en is een typisch voorbeeld van een veel-deeltjeseffect. In dit proefschrift wordt exciton-screening onder invloed van vrije gaten uitvoerig bestudeerd.

Afgezien van de boven besproken exciton-screening blijken ook andere veel-deeltjes effecten van belang te zijn in gedoteerde halfgeleiders. Twee effecten zijn in het bijzonder bestudeerd in dit promotieonderzoek, namelijk exchange en correlatie. Correlatie is zeer sterk gerelateerd aan screening, en wordt veroorzaakt doordat deeltjes van gelijke lading elkaar afstoten. Door deze afstoting zullen de onderlinge afstanden tussen de deeltjes zo groot mogelijk worden en ontstaat in het ideale geval een perfect geordend systeem. Dit geordende, of gecorreleerde, systeem heeft een lagere energie dan een willekeurig verdeeld systeem. Deze energieverlaging kan, zij het indirect, gemeten worden. Het effect van exchange is vergelijkbaar met dat van correlatie, maar de drijvende kracht achter exchange, het zogenaamde Pauli-verbod, is van puur quantummechanische oorsprong en zal hier niet verder besproken worden.

List of publications

1. M. Kemerink and L. W. Molenkamp, “*Stochastic Coulomb blockade in a double quantum dot*”, Appl. Phys. Lett. **65** (8) 1012 (1994).
2. L. W. Molenkamp, Karsten Flensberg, and M. Kemerink, “*Scaling of the Coulomb Energy Due to Quantum Fluctuations in the Charge on a Quantum Dot*”, Phys. Rev. Lett. **75**, 4282 (1995).
3. L. W. Molenkamp and M. Kemerink, “*Stochastic Coulomb blockade and scaling of charging energy in a double quantum dot*”, Superlatt. and Microstr. **16**, 275, (1994).
4. M. Kemerink, P. M. Koenraad, P. C. M. Christianen, A. K. Geim, J. C. Maan, J. H. Wolter, and M. Henini, “*Enhancement of spin-dependent hole delocalization in degenerate asymmetric double quantum wells*”, Phys. Rev. B **53**, 10000 (1996).
5. M. Kemerink, P. M. Koenraad, and J. H. Wolter, “*Effect of strain on a second-order van Hove singularity in $Al_xGa_{1-x}As/In_yGa_{1-y}As$ quantum wells*”, Phys. Rev. B **54**, 10644 (1996).
6. P. A. Bobbert, H. Wieldraaijer, R. van der Weide, M. Kemerink, P. M. Koenraad, and J. H. Wolter, “*Exchange-correlation energy of a hole gas including valence band coupling*”, Phys. Rev. B **56**, 3664 (1997).
7. M. Kemerink, P. M. Koenraad, P. C. M. Christianen, R. van Schaijk, J. C. Maan, and J. H. Wolter, “*Magneto-optical study on exciton screening in p-type $Al_xGa_{1-x}As/In_yGa_{1-y}As$ quantum wells*”, Phys. Rev. B **56**, 4853 (1997).
8. M. Kemerink, P.M. Koenraad, J. H. Wolter, P. C. M. Christianen, A. K. Geim, A. Parlange, J. C. Maan, and M. Henini, “*Spin-dependent hole delocalization enhancement by bandfilling effects in degenerate asymmetric double quantum wells*”, Superlatt. Microstruct. **21**, 217 (1997) (oral presentation at ICSSM-9, Liege, Belgium 1996)

-
- 9 M. Kemerink, P. M. Koenraad, and J. H. Wolter, “*Exchange interaction in p-type GaAs/Al_xGa_{1-x}As quantum wells studied by magneto transport*”, accepted for publication in Phys. Rev. B.
 10. M. Kemerink, P. M. Koenraad, P. C. M. Christianen, R. van Schaijk, J. C. Maan, J. H. Wolter, “*Exciton Screening in p-type Quantum Wells: The Effects of Subband Occupation and Wave Function Overlap*”, accepted for publication in Phys. Stat. Sol. (oral presentation at OECS-5, Göttingen, Germany 1997)
 11. M. Kemerink, P. M. M. Thomassen, P. M. Koenraad, P. A. Bobbert, J. C. M. Henning, and J. H. Wolter, “*Many-particle effects in Be-delta-doped GaAs/Al_xGa_{1-x}As quantum wells*”, submitted to Phys. Rev. B.

Dankwoord

Om de kaft enigszins overzichtelijk te houden sta ik daar als enige auteur vermeld. Dit betekent echter niet dat de inhoud van dit boekje uitsluitend het gevolg is van mijn persoonlijke inspanningen. Gedurende de vier jaar van mijn promotieonderzoek in de groep van Prof. Dr. J. H. Wolter ben ik door talloze personen geholpen die ik daarvoor heel hartelijk wil bedanken. Het plezier dat ik gehad heb in mijn werk is voor een groot deel op hun conto te schrijven. Zonder volledig te kunnen zijn wil ik een aantal mensen met name bedanken.

In de eerste plaats wil ik mijn directe begeleider, Paul Koenraad, bedanken voor zijn aanstekelijk enthousiasme, meedenken, en alle andere zaken die onder een goede begeleiding vallen.

De vele goede tips, bruikbare ideeën en opbouwende kritiek die ik gekregen heb in de discussies met Peter Bobbert, Peter Christianen, John Henning, Jan Kees Maan, Andrea Parlange en Arnout van de Stadt mogen niet onvermeld blijven.

Een belangrijk deel van de metingen in dit proefschrift is uitgevoerd door stagiaires en afstudeerders, die eveneens een grote bijdrage hebben geleverd aan de gebruikte software. In chronologische volgorde: Steven Teeuwen, Eddy Thans, Raymond Cuypers, Rob van Schaijk, Evert Jan de Theije, Jack Luursema, Patrick Thomassen en Joost van den Heuvel.

Geen experimenteel onderzoek kan zonder samples en technische ondersteuning. Zonder de inspanningen van Tom Eijkemans, Cees van Es, Peter Nouwens, Jos van Ruyven en Willem van der Vleuten was dit boekje derhalve een flink stuk dunner geweest. Ook Jos van Amelsvoort en Wil Delissen van het heliumbedrijf wil ik bij deze bedanken voor de continue heliumvoorziening.

De lezerscommissie wil ik bedanken voor de vele nuttige aanwijzingen en correcties gedurende de laatste fase van het schrijven van dit boekje.

Last but not least wil ik alle collega's uit de groep HF bedanken voor de fijne tijd die mijn promotie geweest is.

Curriculum vitae

Martijn Kemerink werd op 23 september 1970 geboren in Hengelo (O). Op zesjarige leeftijd kon hij zowel stikstof als helium vullen in de opstelling van zijn vader aan de universiteit Groningen. Na zijn middelbare schooltijd, van 1982 tot en met 1988 aan het Praedinius Gymnasium te Groningen, vervolgde hij zijn opleiding tot fysicus middels een studie Technische Natuurkunde aan de Technische Universiteit Eindhoven, die hij afronde in 1993. Gedurende zijn studie liep hij stage in de groepen Atomaire en Optische Wisselwerkingen en Lage Temperaturen. Zijn afstudeerwerk verrichtte hij op het Philips Natuurkundig Laboratorium te Eindhoven, onder begeleiding van Laurens Molenkamp. Dit resulteerde in een afstudeerverslag getiteld 'Coulomb-blockade oscillations in a double quantum dot system'. Van november 1993 tot november 1997 werkte hij aan het onderliggende proefschrift in de groep Halfgeleiderfysica onder leiding van Prof. Dr. J. H. Wolter, met als directe begeleider Paul Koenraad. Per 1 januari 1998 is hij voor een periode van drie jaar als 'Akademie-onderzoeker' van de KNAW aan de vakgroep Halfgeleiderfysica van de TUE verbonden.

Gedurende zijn studietijd werkte hij een twintigtal weken als recreatiemedewerker, en later coördinator, bij Storm R&S op verschillende vakantieparken in Duitsland en Nederland. Daarbuiten is hij gedurende de negen jaar van zijn studie en promotie actief lid geweest van studenten zaalhandbal vereniging Oktopus. In dezelfde periode trachtte hij zich te bekwamen in het klassieke gitaarspel.

Stellingen

behorende bij het proefschrift

Many-body effects in the valence bands of two-dimensional heterostructures based on III/V semiconductors

- 1) Het lichte gaten absorptiespectrum van p-gedoteerde GaAs/AlGaAs quantum putten vertoont geen logaritmische van Hove singulariteit, zoals geclaimd door Winkler, maar een tweede-orde van Hove singulariteit.
- *R. Winkler, Phys. Rev. B* **51**, 14395 (1995)
- *dit proefschrift, hoofdstuk 4*
- 2) Verschillen in de ruimtelijke uitgebreidheid van de envelopefuncties van verschillende subbanden in twee-dimensionale heterostructuren zijn essentieel voor een goed begrip van exciton screening.
- *dit proefschrift, hoofdstuk 5*
- 3) Temperatuur-afhankelijke Shubnikov-de Haas metingen zijn ongeschikt voor het bepalen van de effectieve massa van gaten.
- *dit proefschrift, hoofdstuk 6*
- 4) De door Enderlein *et al.* geformuleerde dichtheidsfunctionaaltheorie voor een wisselwerkend gatengas is inconsistent daar de som van de hierin gedefinieerde locale zware en lichte gaten dichtheden niet gelijk is aan de totale locale dichtheid.
- *R. Enderlein, G. M. Sipahi, L. M. R. Scolfaro, and J. R. Leite, Phys. Rev. Lett.* **79**, 3712 (1997)
- 5) Electron transport door zeer smalle halfgeleiderkanalen vertoont sterke overeenkomsten met gasdynamica.
- *L. W. Molenkamp and M. J. M. de Jong, Phys. Rev. B* **49**, 5038 (1994)

- 6) Halfgeleiderfysici tellen beroepsmatig net als kleine kinderen: één, twee, veel.
- eigen observatie gedurende vier jaar promotie
- 7) Het bezuinigen op door de overheid gefinancierd fundamenteel wetenschappelijk onderzoek is in strijd met de toenemende mate waarin industriële patenten leunen op dit onderzoek.
- NRC Handelsblad 31 mei 1997, bijlage W&O, pag. 2
- 8) Uit fair-trade oogpunt (een eerlijke prijs voor producten uit de derde wereld) is het gebruik van cocaïne beter te rechtvaardigen dan de consumptie van koffie zonder Max Havelaar keurmerk.
- 9) De praktijk dat bedrijven en burgers financieel gecompenseerd worden voor stijgende milieu-belastingen, reduceert het nut van deze belastingen.
- 10) Veel 'Bekende Nederlanders' hebben met gaten gemeen dat ze omhoog vallen.